# Passivated-Electrode Insulator-Based Dielectrophoretic Chips for Rare Cell Analysis

Kruthika Kikkeri

Thesis submitted to the faculty of the Virginia Polytechnic Institute and State University
in partial fulfillment of the requirements for the degree of

Master of Science
In
Electrical Engineering

Masoud Agah, Chair
Xiaoting Jia, Co-Chair
William T. Baumann

May 1st, 2018
Blacksburg, VA USA

Keywords: Breast Cancer, Dielectrophoresis, Microelectromechanical Systems (MEMS), Neurons, Staphylococcus epidermidis

Passivated-Electrode Insulator-Based Dielectrophoretic Chips for Rare Cell Analysis

Kruthika Kikkeri

## ABSTRACT

The analysis of potentially harmful biological particles is imperative for the mitigation of disease. As a result, there is a growing need for tools which can characterize, detect, and separate biological particles for the alleviation of a multitude of disease. One powerful technique for the analysis of cells is the use of dielectrophoresis (DEP) forces for the manipulation of particle movement. DEP is a particle transport phenomenon, induced by the presence of non-uniform electric fields. The dependence on intrinsic electrical properties of cells, have enabled DEP force to be utilized for numerous biological analyses. This thesis presents the investigation of breast cancer, pathogen, neuronal and glial cells and their DEP profiles. The drug response of various breast cancer cell lines when exposed to a variety of chemical stimuli were analyzed using shifts in their DEP profiles in relation to control groups. These results were supplemented with cell proliferation assays, morphology imaging, and gene expression analysis to identify biophysical changes which could contribute to the DEP shifts. Additional experiments were conducted for the monitoring of pathogens. Live/dead bacteria mixtures were evaluated using an integrated system with DEP enrichment and impedance spectroscopy. An algorithm was utilized to estimate concentrations of live/dead bacteria, and then compared with flow cytometry results. Another application of DEP which was investigated was the separation of heterogeneous mixtures. Through the use of a novel microfluidic channel design, the separation of simulated circulating tumor cells (CTCs) from diluted whole blood and

neuron cells from glial cells was demonstrated. The wide range of applications examined in this thesis highlights the versatility of DEP and the flexibility of the reported devices.

Passivated-Electrode Insulator-Based Dielectrophoretic Chips for Rare Cell Analysis

Kruthika Kikkeri

## GENERAL AUDIENCE ABSTRACT

Microscale technology can be utilized for the identification, characterization and sorting of biological material in a plethora of biomedical applications. One promising technique which is capable of cell manipulation is dielectrophoresis (DEP). DEP is a microscale force which causes particles to be attracted or repelled by specific geometries in microchannels. The DEP force is produced by the application of electric fields and can be utilized to analysis biological cell populations. This is because biological particles have unique electrical properties based on their cell morphology. Distinctions in their external protrusions and internal structures contribute to their electrical properties and can be identified in their DEP profiles. Based on this concept a variety of biomedical applications of DEP was explored. Chapter 2 and 3 describe the investigation of cells when exposed to various drugs. Drug induced responses were characterized based on their shifts in their DEP profiles. Chapter 4 presents the a rapid and low-cost live/dead assay for bacteria in aqueous samples through DEP and impedance spectroscopy. In chapter 5, the development of a DEP platform for cell sorting is reported. The wide range of biomedical applications which were explored demonstrate the useful nature of the DEP phenomenon.

**To Narayana (Venka) Kikkeri**

# Acknowledgements

Throughout my time at Virginia Tech, my academic career has been enriched by countless people. First, I would like to express my utmost gratitude towards my advisor Dr. Masoud Agah who has guided through this entire process. I have had numerous amazing opportunities because of his support and wisdom. I am very grateful to have had the chance to join VT MEMS Lab. I would also like to thank my co-advisor Dr. Xiaoting Jia whose incredible support and knowledge has greatly enriched my graduate experience. I would also like to thank Dr. Jeannine Strobl for the countless hours she spent providing us with valuable feedback for experiments and papers, as well as helping us better understand biological material.

Beyond my advisors, I would also like to the current and past members of the VT MEMS Lab and Jia Lab. All of you have been an been my inspiration and motivation throughout the years. I owe a special thanks for Sepeedah Soltanian-Zadeh for her assistance during my first year in the VT MEMS Lab and Shan Jiang for her expertise and remarkable fabrication skills. Additionally, I would like to thank Parham Ghassemi, Xiang Ren, Ana Lopez Marcano, Shan Jiang and Ryan Chan for all your help and for making the lab more enjoyable.

For the majority of my projects, I have been fortunate enough to work with remarkably talent individuals through various collaborations. I want to thank Dr. Ayesha Shajahan-Haq from the Georgetown Lombardi Comprehensive Cancer Center for her continued support of the VT MEMS Lab and all our microsystems projects. I would also like to thank Dr. Amy Pruden and Dr. Maria Virginia Riquelme for their help with

pathogen samples and analyses. Additionally, I would like to thank Dr. Andrea Bertke for her help with the extraction of neuron and glial cells.

Last, but not least, I would like to thank my family and friends. Particularly, I would like to thank my dad (Nagendra Kikkeri), aunt (Prema Kikkeri), and brother (Navneeth Kikkeri) for their unwavering support, and for shaping me to be the person I am today. I appreciate each person's efforts and without all of you I would not have survived graduate school.

# Table of Contents

# List of Figures

# List of Tables

# 1 Introduction

## 1.1 Background

Biomedical devices and biotechnologies are by far one of the fast growing fields to date [1-3]. This is as a result of the large number of unmet needs in the areas of disease prevention, detection, and treatment [1, 3-11]. Cancer, for example, is one of the leading causes of death worldwide, with nearly nine million deaths annually [12]. However, the underlying mechanisms that initiate metastasis, which is directly related to 90% of cancer related deaths, still remain largely unknown [13]. Currently, specific cells such as circulating tumor cells (CTCs) or tumor initiating cells (TICs) are thought to be responsible for the spread of these aggressive cancers [14, 15]. However, these cells are difficult to detect due to their low abundance and heterogeneity of samples. Other challenges include the limited understanding of causes of drug resistance or multidrug resistance. These challenges can also apply to other ailments such as neurological disorders or illness caused by pathogens [10, 16, 17]. Thus, tools which can help us better understand biological samples can have direct applications to a variety of biomedical needs.

Microsystems which stem from microelectromechanical systems (MEMS) and micro total analysis systems (μTAS) technology have revolutionized analytical instrumentation for numerous biomedical applications [9, 11, 18]. The microscale manipulation of biological material presents several inherent advantages. One clear advantage is the relatively low cost of devices. These miniaturized structures often capitalize on the highly developed microfabrication techniques that arose from the integrated circuit (IC)/semiconductor industry which enables bulk manufacturing. This combined with the ability to reduce material volumes have resulted in lower manufacturing

costs than similar macroscale technologies. Additional benefits of microsystems include the increase in throughputs with high density arrays, reduction of samples and reagent requirements, and overall reduction of bulky platforms [8]. However, possibly the most distinctive benefits of these systems is the intrinsically small size of the platform, which enables them to use micro-scale phenomena to analyze biological material. Based on scaling laws, forces which dominate at the macroscale, are negligible at the microscale. Instead, other forces such as electrostatics, dipole forces, and stokes drag dominate [19, 20]. This enables microsystems to have higher sensitivities and smaller time scales, making them highly useful platforms.

An electrokinetic phenomena which has shown great promise in the characterization, detection, and separation of various biological material is dielectrophoresis (DEP) [19, 21-23]. DEP is the term used to describe the movement of polarizable particles in non-uniform electric fields [24, 25]. Traditional DEP devices employ an array of thin-film interdigitated electrodes placed within a flow channel to generate a non-uniform electric field that interacts with particles near the surface of the electrode array. However, these electrodes embedded DEP (eDEP) platforms often lack robustness, have relatively high costs, can have bubble formation at the electrode-liquid boundary, and have low throughputs [8]. In contrast, insulator-based DEP (iDEP) is a technique which utilizes insulating obstacles instead of electrodes within the device to produce spatial non-uniformities in the electric field. iDEP is a practical method to obtain the selective cell manipulation while overcoming most of the challenges associated with traditional DEP. Yet, in even with iDEP devices, the electrodes must contact the solution

in the reservoirs of the channel which can cause cross-contamination [26]. Additionally, the wide spacing of these electrodes leads to large voltages for actuating them.

To alleviate these issues, the VT MEMS Laboratory developed the passivated-electrode insulator-based dielectrophoresis (πDEP) platform [26-28]. The πDEP assuages the shortcomings of the current eDEP and iDEP mechanisms by utilizing insulator structures to generate strong, localized electric field gradients, while incorporating electrode with a passivation layer. This passivation layer prevents fouling of electrodes, electrolysis, and enables the fabrication of disposable microfluidic chips and reusable electrodes. In principle, electric fields are capacitively coupled through the passivation layer to induce DEP forces in the microfluidic channels. This thesis presents several designs of the πDEP for applications involving breast cancer, bacteria, whole blood, neuron and glial cells. These investigations have demonstrated the versatility of the DEP platform for cell characterization and drug response assessment, environmental pathogen monitoring, and heterogeneous mixture separation.

## 1.2 Theory

DEP is the electrokinetic phenomena which induces the motion of a particle in the presence of an electric field gradient. This occurs through the formation of an electric dipole moment (**p**) due to the polarization of particles in the non-uniform electric field. Positive and negative charges (+Q and –Q, respectively) are directed to opposite sides of particles, making the dipole moment a function of the charge (Q) and the displacement vector between two point charges (negative and positive points) (**d**) as shown in Equation 1.1 [19].

$$\mathbf{p} = Q\mathbf{d} \tag{1.1}$$

This causes orientation of particle moment to be dependent on polarizability of the particle versus that of the surrounding medium. If the particle polarizability is greater than the surrounding medium, the direction of the particle's dipole moment will align with the electric field orientation. Otherwise the dipole moment of the particle will be oriented against the electric field direction. These polarized particles experience a torque and align themselves in the electric field to minimize their electric field potentials. In a non-uniform electric field, the two poles of the moment **p** experience different electric forces which induces movement. This force which induces particle transport is referred to as the DEP force. Larger electric field gradients will induce larger particles due to the differential forces on the dipoles. The net difference between the two components (+Q and –Q sides) is used to determine the magnitude of the DEP force. The Taylor expansion and further details on this derivation is presented in [19]. Thus, the first order DEP force can be expressed in terms of the dipole moment as:

$$\boldsymbol{F_{DEP}} = (\mathbf{p} \cdot \nabla)\boldsymbol{E} \tag{1.2}$$

It should be noted that this expression is the DEP force is its simplest, first order form and neglects higher order moments. For spherical particles, higher order moments can be solved for effective moments up to any arbitrary order. However, higher order moments are often considered negligible. When multiple closely spaced particles are exposed to a non-uniform electric field, there is a dipole-dipole interaction which causes "pearl chaining." Here particles essentially align themselves together in lines which tend to follow electric field equipotential lines. They then traverse through the electric field together based on the DEP force.

The magnitude of the dipole moment is linearly proportional to the particle's effective polarizability, volume of the particle and magnitude of the applied electric field. For spherical particles with radius *R*, dipole moments can be described as:

$$\mathbf{p} = 4\pi R^3 \varepsilon_o \varepsilon_{r_{medium}} Re[CM]\boldsymbol{E} \tag{1.3}$$

where $\varepsilon_o$ is the permittivity of free space, $\varepsilon_{r_{medium}}$ relative permittivity of the surrounding medium, and Re[29] is the Clausius-Mossotti factor [19]. Substitution of Equation 1.3 into 1.2 forms the following equation:

$$\boldsymbol{F_{DEP}} = 4\pi R^3 \varepsilon_o \varepsilon_{r_{medium}} Re[CM]\nabla \boldsymbol{E}^2 \tag{1.4}$$

This form of the DEP force is more commonly used as it can be applied to both direct current (DC) and alternating current (AC) induced electric fields without additional mathematical manipulation.

As particle radius, permittivity of the surrounding medium, and electric field gradients are generally fixed in experimentations, the CM factor value is often manipulated for DEP assays. The CM factor for spherical particles is:

$$CM = \frac{\varepsilon_p^* - \varepsilon_m^*}{\varepsilon_p^* + 2\varepsilon_m^*} \tag{1.5}$$

where $\varepsilon_p^*$ is the complex permittivity of the target particle, and $\varepsilon_m^*$ is the complex permittivity of the surrounding medium [19]. Complex permittivities are defined as:

$$\varepsilon^* = \varepsilon + \frac{\sigma}{j\omega} \tag{1.6}$$

where $\sigma$ is the conductivity, $j$ is $\sqrt{-1}$, and $\omega$ is the radial frequency of the applied electric field [19]. Based on this relation, it can be deduced that at low frequencies the conductivities dominate the CM factor, while at high frequencies the permittivities dominate. Furthermore, it can also be observed that the complex permittivity of the

particles versus the surrounding medium can result in positive, negative, or null CM factors. For cases where $\varepsilon_p^* > \varepsilon_m^*$, the CM is positive, meaning that the induced dipole moment is directed towards the direction of the electric field. The particles in this field will experience a force which attracts them to the electric field gradient maxima, otherwise referred to as positive DEP (pDEP). In contrast, for cases where $\varepsilon_p^* < \varepsilon_m^*$, the CM is negative, meaning that the induced dipole moment is oriented opposite to the direction of the electric field. The particles in this field will experience a force which attracts them to the electric field gradient minima, otherwise referred to as negative DEP (nDEP). When the $\varepsilon_p^* = \varepsilon_m^*$, the CM factor is zero and is often referred to as the crossover frequency [19]. Figure 1.1 displays behavior observed under different CM values. Thus, the intrinsic electrical properties of particles greatly influence the CM factor and consequentially the DEP force.

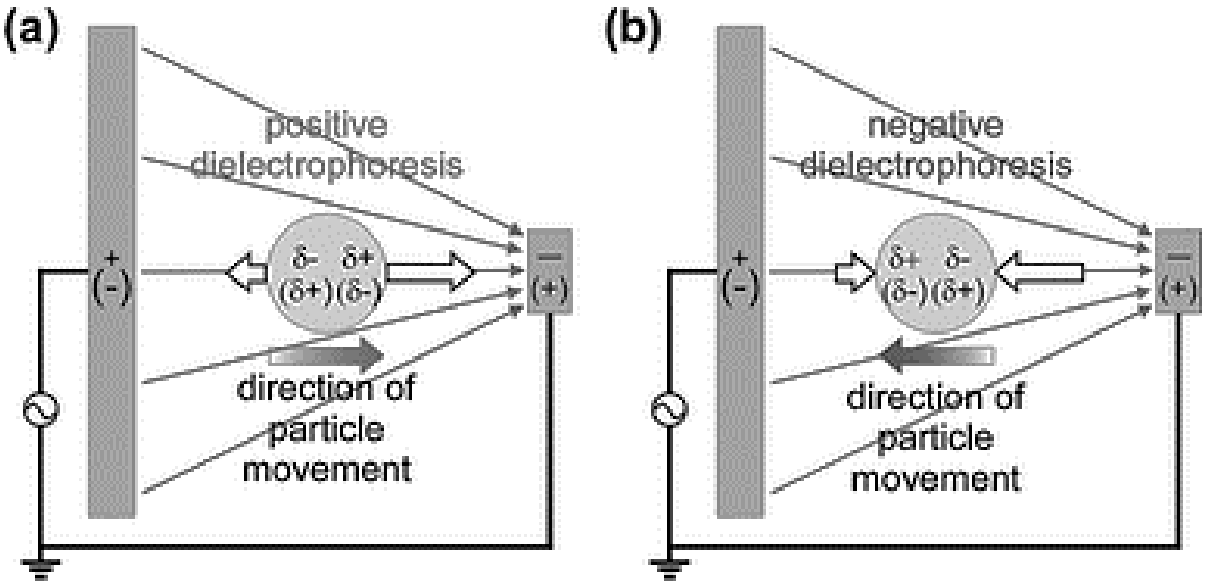


**Figure 1.1:** Image of particle movement under positive and negative DEP conditions [15].

For biological particles, several models have been described to determine the effective complex permittivities. One method to model biological cells is through the use of shells. These models represent different components (organelles) of the cell as shells or groups. The single shell model as shown in Figure 1.2 uses the cell membrane as one shell and combines the internal organelles as another shell designated to be the cytoplasm components. Higher order models incorporate additional shells to represent individual organelles. Although multi-shell models can provide detailed information on the internal structure of cells, the single shell model can be sufficient for many applications [19].

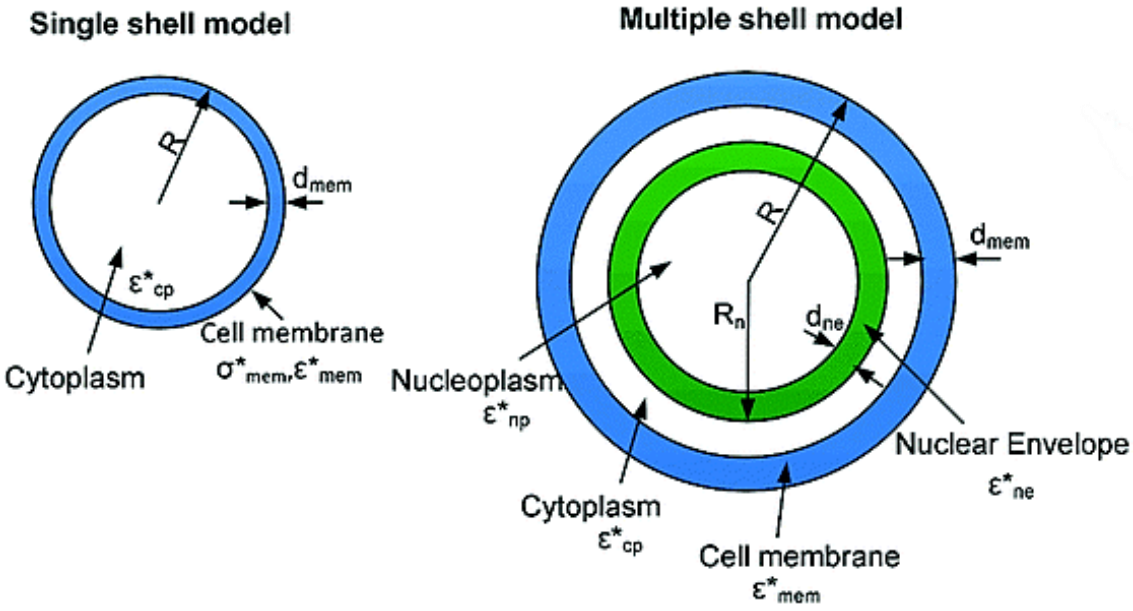


**Figure 1.2:** Examples of single and multiple shell models [19].

Based on these models, it has been shown that morphology of cells impacts the CM factor. As shown in Figure 1.3, membrane roughness (membrane specific capacitance), particle size, cytoplasm conductivity, nucleus-cytoplasm ratio and cytoplasm permittivity can modulate the CM factor. Additionally, it shows the influence of the media conductivity

on the maximum positive CM factor values. These factors can be used to analyze various biological samples based on their DEP properties through microfluidic assays.

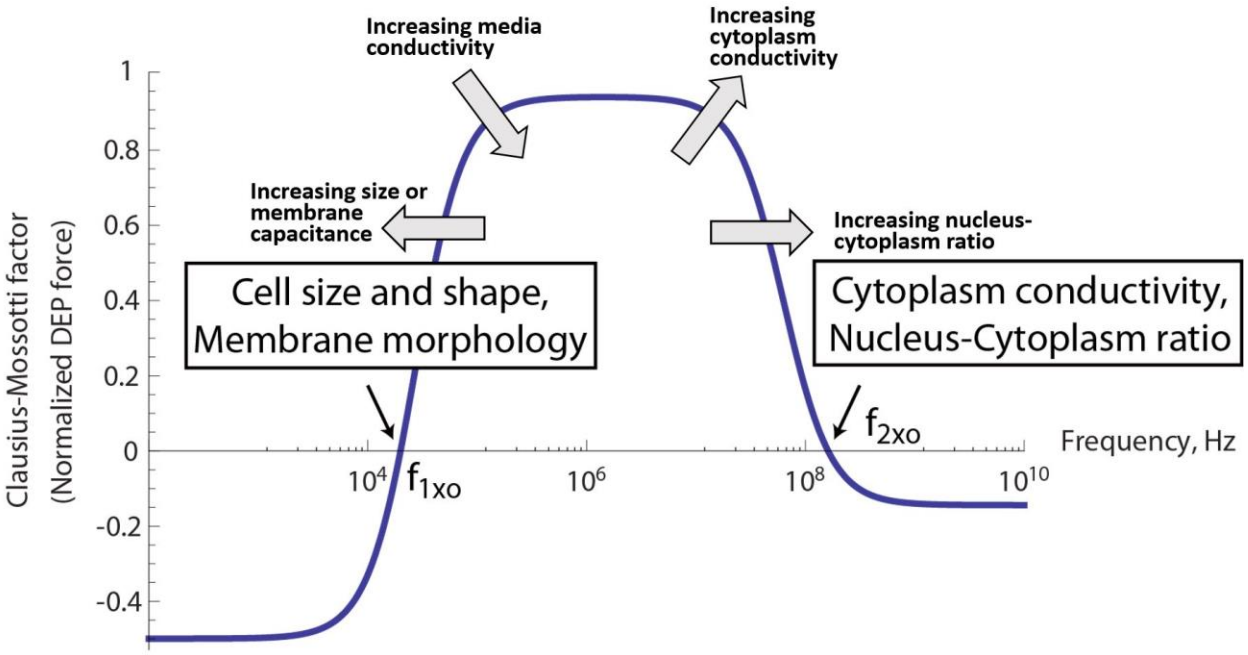


**Figure 1.3:** CM factor as a function of frequency. Image was modified from [17].

For microfluidic-based DEP experiments, a number of additional force influence the movement of particles. For microfluidic investigations which involve fluid flows, the movement of particles based on the force balance between the DEP force and Stoke's drag. Thus, the "DEP trapping" is used to describe when the DEP force dominates. Generally, this is used to push particles to either the electric field maxima or minima and remain stationary in that region. However, when Stoke's drag dominates, particles flow with the bulk fluid through the microfluidic channels. In either case, both forces can be modulated to cause unique cell movements. Modification of DEP parameters and fluid flow rates can be used to characterize, detect a separate various biological samples.

## 1.3 References


[1] Oliver, N., Toumazou, C., Cass, A., Johnston, D., *Diabetic Medicine* 2009, *26*, 197-210.

[2] Wolpaw, J. R., Birbaumer, N., Heetderks, W. J., McFarland, D. J., Peckham, P. H., Schalk, G., Donchin, E., Quatrano, L. A., Robinson, C. J., Vaughan, T. M., *IEEE transactions on rehabilitation engineering* 2000, *8*, 164-173.

[3] Stock, U. A., Vacanti, J. P., *Annual review of medicine* 2001, *52*, 443-451.

[4] Yu, Z., Guo, X., Jiang, Y., Teng, L., Luo, J., Wang, P., Liang, Y., Zhang, H., *Breast Cancer* 2017.

[5] Nathan, M. R., Schmid, P., *Oncology and Therapy* 2017, *5*, 17-29.

[6] Tang, Y., Wang, Y., Kiani, M. F., Wang, B., *Clin Breast Cancer* 2016.

[7] Jeselsohn, R., Buchwalter, G., De Angelis, C., Brown, M., Schiff, R., *Nat Rev Clin Oncol* 2015, *12*, 573-583.

[8] Li, M., Li, W. H., Zhang, J., Alici, G., Wen, W., *Journal of Physics D: Applied Physics* 2014, *47*, 063001.

[9] Sajeesh, P., Sen, A. K., *Microfluidics and Nanofluidics* 2014, *17*, 1-52.

[10] Hanani, M., Spray, D. C., in: Parpura, V., Verkhratsky, A. (Eds.), *Pathological Potential of Neuroglia: Possible New Targets for Medical Intervention*, Springer New York, New York, NY 2014, pp. 473-492.

[11] Dittrich, P. S., Manz, A., *Nat Rev Drug Discov* 2006, *5*, 210-218.

[12] Siegel, R. L., Miller, K. D., Jemal, A., *CA Cancer J Clin* 2016, *66*, 7-30.

[13] Lee, D., Nam, S. M., Kim, J.-a., Di Carlo, D., Lee, W., *Analytical chemistry* 2018, *90*, 2902-2911.

[14] Sollier, E., Go, D. E., Che, J., Gossett, D. R., O'Byrne, S., Weaver, W. M., Kummer, N., Rettig, M., Goldman, J., Nickols, N., *Lab on a Chip* 2014, *14*, 63-77.

[15] Plaks, V., Koopman, C. D., Werb, Z., *Science* 2013, *341*, 1186-1188.

[16] Bartram, J., *Pathogenic mycobacteria in water: a guide to public health consequences, monitoring and management*, World Health Organization 2004.

[17] Sghirlanzoni, A., Pareyson, D., Lauria, G., *The Lancet Neurology* 2005, *4*, 349-361.

[18] Gossett, D. R., Weaver, W. M., Mach, A. J., Hur, S. C., Tse, H. T. K., Lee, W., Amini, H., Di Carlo, D., *Analytical and bioanalytical chemistry* 2010, *397*, 3249-3267.

[19] Pethig, R. R., *Dielectrophoresis: Theory, Methodology and Biological Applications*, John Wiley & Sons 2017.

[20] Castellanos, A., Ramos, A., Gonzalez, A., Green, N. G., Morgan, H., *Journal of Physics D: Applied Physics* 2003, *36*, 2584.

[21] Soltanian-Zadeh, S., Kikkeri, K., Shajahan-Haq, A. N., Strobl, J., Clarke, R., Agah, M., *ELECTROPHORESIS* 2017, *38*, 1988-1995.

[22] Kikkeri, K., Agah, M., *2017 IEEE 30th International Conference on Micro Electro Mechanical Systems (MEMS)* 2017, pp. 358-361.

[23] Pethig, R., *Biomicrofluidics* 2010, *4*, 022811.

[24] Pohl, H. A., Crane, J. S., *Biophysical journal* 1971, *11*, 711-727.

[25] Pohl, H. A., *Journal of Applied Physics* 1951, *22*, 869-871.

[26] Zellner, P., Shake, T., Sahari, A., Behkam, B., Agah, M., *Anal Bioanal Chem* 2013, *405*, 6657-6666.

[27] Nakidde, D., Zellner, P., Alemi, M. M., Shake, T., Hosseini, Y., Riquelme, M. V., Pruden, A., Agah, M., *Biomicrofluidics* 2015, *9*, 014125.

[28] Shake, T., Zellner, P., Sahari, A., Breazeal, M. V. R., Behkam, B., Pruden, A., Agah, M., *Analytical and Bioanalytical Chemistry* 2013, *405*, 9825-9833.

[29] Abd El-Rehim, D. M., Ball, G., Pinder, S. E., Rakha, E., Paish, C., Robertson, J. F., Macmillan, D., Blamey, R. W., Ellis, I. O., *Int J Cancer* 2005, *116*.

# 2 Breast Cancer Cell Obatoclax Response Characterization using Passivated-Electrode Insulator-Based Dielectrophoresis

This chapter was reproduced from [27] with permission from Wiley.

*Soltanian-Zadeh, S.*, Kikkeri, K.*, Shajahan-Haq, A. N., Strobl, J., Clarke, R., Agah, M., ELECTROPHORESIS 2017, 38, 1988-1995.*

*Equal contribution

For this project, my contributions included device fabrication, DEP experimentation and analysis of the DEP profiles. For initial DEP investigations, frequency sweeps and parameter optimization experiments were split equally between myself and another graduate student. Further experiments to show the impact of varying concentrations of chemical stimuli were conducted solely by myself. I also assisted in the writing of this manuscript.

## 2.1 Introduction

At diagnosis, 70% of breast tumors express estrogen receptors (ER+) and the standard of care for these patients is endocrine therapy with antiestrogens or aromatase inhibitors [1]. These therapies are designed to deprive the tumor of growth promoting actions of estrogens and while they do have initial widespread clinical efficacy, 50% of women receiving endocrine therapy will show either de novo resistance or acquired resistance [2]. Therefore, endocrine resistance remains a major challenge in the clinic. In the laboratory, endocrine resistance has been studied at the molecular level using established breast cancer cell lines such as the ER+ MCF-7 derivatives, LCC1 and LCC9 [3]. MCF-7 cells have been used to model patients whose tumors are growth stimulated

by estrogens and growth inhibited by anti-estrogen drugs [4]. LCC1 cells were selected from MCF-7 cells during *in vivo* propagation in mouse xenografts; although growth of LCC1 cells is estrogen independent, LCC1 grow is inhibited by anti-estrogens. LCC9 cells are a derivative of LCC1; LCC9 cells were selected *in vitro* from LCC1 cells and are estrogen-growth independent and anti-estrogen resistant [3]. Thus, LCC1 and LCC9 cells represent forms of ER+ breast cancer that require new drug treatments are excellent models to screen new anti-cancer agents.

To provide patients with more targeted cancer treatments, cell lines must be further analyzed to characterize ER+ cells and their response to experimental anti-cancer agents. Conventional cell manipulation methods such fluorescent tagging with Annexin V [5], MTT assays, and the trypan blue assays can be used to study drug induced growth inhibition and cell death. Such assays showed that LCC1 and LCC9 cell density decreased in response to GX, an anti-tumor BH3-mimetic drug (GX15-070) [6]. However, proliferation assays can be laborious, time consuming and fail to provide insight into drug-induced biophysical changes. Methods such as electrorotation have been utilized to characterize cells based on their dielectric properties [7]. Huang et al. demonstrated the ability of electrorotation to detect cell membrane responses to drug-induced apoptosis in HL-60 cells [8]. This technique was able to provide real-time membrane property measurements for single cells, however, due to its low throughput, it is very difficult to analyze the changes in cell populations.

One promising alternative for analyzing the drug response of cancer cells is dielectrophoresis (DEP). DEP can provide insight into changes occurring in cell biophysical attributes including size, membrane capacitance, and cytoplasmic

conductivity. DEP is an electrokinetic-based technique in which uncharged particles suspended in a fluid can be moved via polarization forces induced by an inhomogeneous electric field [9]. It is a highly versatile and customizable method which does not require biological markers [10] and can be used to manipulate bioparticles based on their dielectric properties and discriminate based on the cell's physiological state [11]. Moreover, DEP based characterization can be further integrated into microfluidic platforms to provide separation of live and dead cells [5], to separate circulating tumors cells from blood samples [12], or provide real time analysis of drug induced cytotoxicity in cells [13]. Typical AC electric fields used in DEP have not shown adverse effects on cells when applied within certain frequency and voltage ranges [14]. Therefore, integrating microfluidics into DEP based characterization can provide Lab-On-Chip systems which provide high throughput with real time analysis of live cells.

Various DEP based methods have been used to study the effect of drugs on cells. In a study by Wang et al., the effectiveness of DEP characterization as a rapid method superior to DNA fragmentation for the detection of drug-induced apoptosis in human myelogenous HL-60 cells was demonstrated [15]. In addition, DEP has been utilized to complement flow cytometry to understand the underlying mechanism in multi-drug resistance reversal in human leukemic cells [16] and human breast cancer cells [17]. Henslee et al. used the 3DEP$^{TM}$ system to show DEP results were comparable to standard assays such as flow cytometry, trypan blue, and MTT assay whilst being faster and label-free [18]. The 3DEP$^{TM}$ system was also used to complement flow cytometry assessments of drug-induced apoptosis progression in Jurkat T-cells [19]. Similar studies have been carried out using DEP based techniques to study the drug-induced apoptosis in lung cancer

cells [20]. These studies illustrate the value of DEP in drug response analysis using electrodes in direct contact with cell samples. Such methods pose limitations such as sample contamination, electrolysis, and delamination of electrodes [21].

In contrast, the off-chip passivated-electrode insulator-based dielectrophoresis (OπDEP) uses a unique DEP design in which AC electric fields are capacitively coupled into the microchannel to alleviate some of the commonly known limitations in electrode-based DEP. This technique generates necessary electric field gradients through micro-pillars embedded within the microfluidic channel while utilizing reusable electrodes positioned on a separate detachable substrate for AC electric field generation. This platform has been previously used to isolate live and dead bacteria [22]. However, this is the first demonstration of the applicability of this technique for breast cancer cell drug analysis and the first use of insulator-based DEP for analyzing closely related drug sensitive and drug resistance breast cancer cells.

In this study, we employ the OπDEP platform to characterize two ER+ breast cancer cell lines, LCC1 and LCC9, and their DEP response to 100nM, 500nM, and 1μM treatments of the anti-tumor drug GX. Scanning Electron Microscope (SEM) imaging was performed to compare the DEP results with cell morphological changes. Cell proliferation assays were performed to compare the DEP findings with a conventional drug assessment method.

## 2.2 Materials and Methods

### 2.2.1 Device Fabrication

Fabrication of OπDEP devices used in this study followed processes previously presented [22]. Electrodes were fabricated on a glass substrate through photolithography

and deposition of chrome/gold by physical vapor deposition. A lift-off process was then employed to create a pair of electrodes with dimensions of 1000µm and 600µm in width and horizontal spacing, respectively, on a 500µm thick glass substrate. After, a silicon wafer is patterned with photoresist and dry etched to create a negative silicon master.

Polydimethlsiloxanne (PDMS) (Dow Corning, MI, USA) microfluidic channels with an array of insulator pillars were fabricated using the negative silicon wafer as the mold. Inlets and outlets were punched on each chip and then bonded to a 100µm thick #0 cover glass slide (Electron Microscopy Sciences, PA, USA) which separates the microfluidic chip from the electrodes. The microfluidic component was placed directly above and between the electrodes with minimal alignment and attached using tape. Figure 2.1 shows an optical image of the OπDEP chip with a close-up of the insulating pillars which are 100µm in diameter with edge-to-edge 30µm spacing with a depth size 40µm for the entire microfluidic channel. Overall size of the entire chip is 3cm×2.5cm.

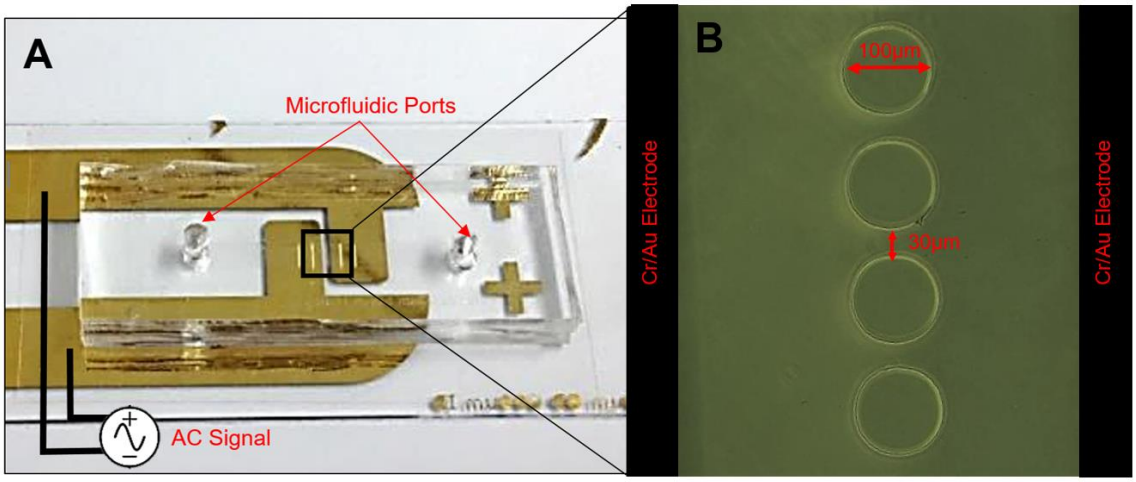


**Figure 2.1:** (A) Top view of the fabricated microfluidic chip and electrodes. The image shows the alignments of the microfluidic device with the DEP pillars positions directly above and in-between the reusable (detachable) electrodes spaced 400 µm. (B) Close-up

of the DEP pillars within the microfluidic chip and electrodes that lie below the microfluidic chip and surround the DEP pillars.

### 2.2.2 Cell Culture and Treatments

LCC1 and LCC9 cells lines were obtained from Tissue Culture Shared Resources of the Lombardi Comprehensive Cancer Center, Georgetown University, Washington, DC. As recommended by the supplier, cells were maintained in T-25 flasks in Minimum Essential Medium (MEM Richter's modification) (Life Technologies, NY, USA) containing 5% Donor Calf Serum Charcoal Stripped (Valley Biomedicals, VA, USA) and antibiotics, 100 U/mL penicillin and 100µg/mL streptomycin (Mediatech, VA, USA), at 37°C in a humidified 5% CO2 incubator.

LCC1 and LCC9 cells were treated with GX (Selleckchem, TX, USA) for 12 hours. Stock solutions of GX were prepared in dimethyl sulfoxide (DMSO) (Life Technologies, NY, USA), stored at -80°C, and diluted in culture media to the desired concentrations. A vehicle control treatment using 0.1% DMSO was also performed on both cell lines.

Immediately prior to DEP analysis, cells were harvested and fluorescently tagged with 5µM 5-chloromethylfluorescein diacetate (Cell Tracker Green CMFDA Dye) (Life Technologies, NY, USA) in a low conductivity DEP buffer prepared by adding 8.5g sucrose (Sigma Aldrich, MO, USA) and 0.725mL MEM (Life Technologies, NY, USA) in 100mL deionized water [23]. The conductivity of the DEP buffer was found to be 113±0.54µS/cm as measured using Conductivity Meter SG7 (Mettler Toledo, Scherzenbach, Switzerland). Cells were washed two times with DEP buffer to remove residual drug and CMFDA and avoid alterations in the solution conductivity. The final cell concentration in the samples was adjusted to $2\times10^6$cells/mL for all experiments.

### 2.2.3 Experimental Setup

For experimentation, a 1mL syringe containing the fluorescently tagged cell solution was connected to the chip and the solution was driven through the channel at a constant flow rate of 10, 20, or 50µL/hr based on the experiment of interest, using a Pump11 Elite syringe pump (Harvard Apparatus, MA, USA). Experiments were conducted at frequencies 50kHz and100kHz-1MHz at 100kHz intervals. Voltages were applied over this frequency range to the electrodes using a 50MHz function generator (4079 50MHz Dual-Channel Arbitrary Waveform/Function Generator, B&K Precision, CA, USA) and a voltage amplifier (A800DI Voltage Amplifier, FLC Electronics AB, Sweden) to initiate DEP forces induced by the application of the AC electric field causing trapping around the pillars. Trapping of the cells was observed using a Zeiss Axio Observer.Z1 inverted epifluorescence microscope (Germany) with a 10X objective lens and imaged using a Zeiss AxioCam MRc camera (Germany).

Trials were observed for 25 seconds to account for 20 second DEP excitation, cell release and to allow cells to return to a continuous flow (see supporting information 1 and 2 for videos of trapping). Trapping efficiencies were calculated as the ratio of trapped cells to the total number of cells in each run. Crossover frequencies were determined by experimentally sweeping the voltage over the 50kHz-1MHz range to determine the frequency at which the cell switch from being repelled by the highest gradient areas in the electric field (negative DEP) to being attracted to the highest gradient areas in the electric field (positive DEP). Only values for positive DEP are reported. Trials were operated using 20µL/hr flow rate and $80V_{peak\text{-}to\text{-}peak}$ applied voltage. These two values were the optimal values for this study, see supporting information 3 for further information.

### 2.2.4 Scanning Electron Microscope Sample Preparation

Cells were grown with and without drug treatment on individual glass slides and fixed using a 4% formaldehyde solution in phosphate-buffered saline (PBS, Baker, PA, USA). Samples were post-fixed in 1% osmium tetraoxide, serially dehydrated in a graded ethanol series (15%, 30%, 50%, 70%, 95%, 100%), and critical point dried. After sputter coating the samples with gold, SEM images were acquired using a Carl Zeiss EVO 40 SEM (Germany).

### 2.2.5 Cell Size Measurement

Cell size in suspension was measured using images captured by the epifluorescence microscope and analyzed using the image processing software, Zen Pro Blue (Germany). Fifty cell sizes were measured for LCC1 and LCC9 vehicle and GX-treated trials. Final cell size was reported as the mean ± standard deviation.

### 2.2.6 Cell Proliferation Assay

Cell proliferation assays were performed to assess the time course of response to GX. Cell proliferation was determined using the crystal violet assay. Cells were seeded at a proliferation of $5\times10^3$ per well in 96-well plates. 24 hours later, the indicated concentration of GX or vehicle control was added for 12, 24 or 48 hour treatments. Following treatment, cells were stained with a crystal violet staining solution as previously described [6]. Sodium citrate buffer was used to extract the dye, and an index of cell proliferation was obtained using the absorbance at 550nm using a microplate reader (Bio-Rad, CA, USA). Results at 12, 24 and 48 hours are shown in Figure 2.2. LCC9 cells are significantly more sensitive to 500nM GX than LCC1 cells, confirming an earlier report by Schwartz et al [6].

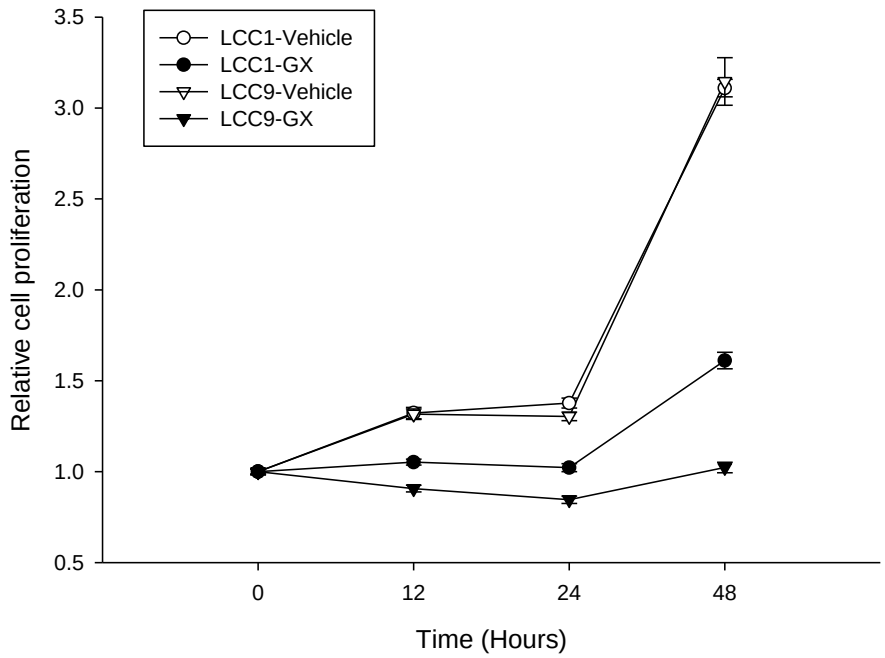


**Figure 2.2:** Proliferation assay results for untreated and GX-treated LCC1 and LCC9 cells under control conditions (DMSO vehicle alone). LCC1 and LCC9 cells showed similar rate of proliferation at 12, 24 and 48 hours. With 500nM GX treatment, LCC9 cells showed significant increase in sensitivity to Obatoclax compared with LCC1 cells at 12, 24 and 48 h ($p<0.05$, ANOVA).

### 2.2.7 Statistical Significance Analysis

For multiple group comparisons, Student-Newman-Keuls method comparison test was applied following ANOVA. Results were considered to be significantly different at $p < 0.05$. Statistical analysis was carried out using the Sigma Plot software (Jandel Scientific, SPSS, Chicago, IL, USA).

## 2.3 Results

### 2.3.1 DEP Characterization of Breast Cancer Drug Response

While discerning among different cell types is an established application of DEP-based technologies, drug response characterization is another area which can benefit from DEP characterization methods and has not been explored to a great extent. Therefore, a drug sensitivity study of LCC1 and LCC9 cells to the drug GX was performed using the OπDEP platform. Figure 2.3 shows the response of LCC1 and LCC9 cells to GX treatment at 100nM, 500nM and 1µM compared to their vehicle counterparts.

Vehicle control and GX-treated cells in both cases have notably different DEP profiles. In both cell lines, the crossover frequency shifted to a higher value in response to 1µM GX exposure with LCC9 cells showing a larger shift in the crossover compared to LCC1 cells. As seen in the Figure 2.3, the LCC1 vehicle-treated cells had an initial crossover frequency of 700kHz. After 100nM GX treatment, the LCC1 cells shifted their crossover frequency to 800kHz. When exposed to the 500nM and 1µM GX treatments, the cells reached a maximum in crossover frequency of 900kHz.

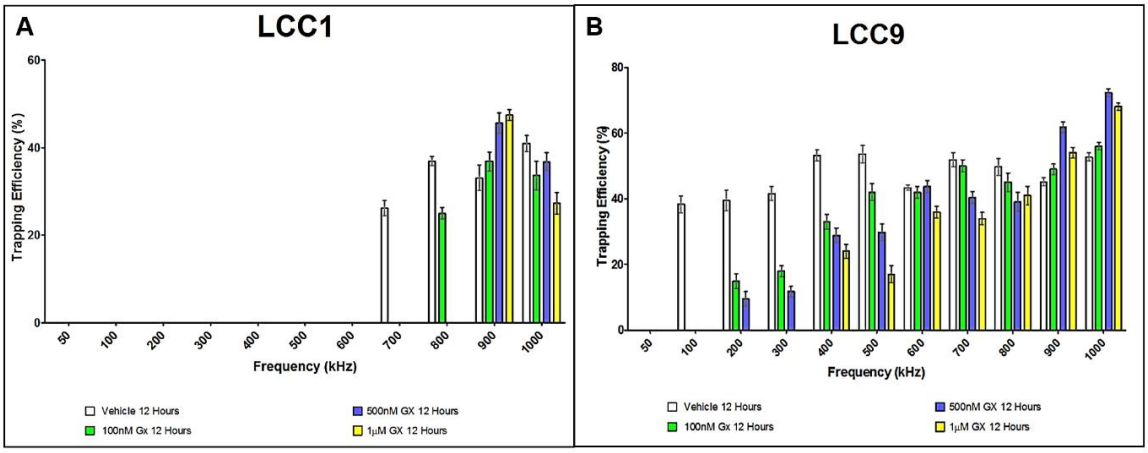


**Figure 2.3:** Trapping profile of vehicle and GX-treated at 100nM, 500nM, and 1µM (A) LCC1 and (B) LCC9 cells, each bar represents mean ± standard error of mean for at least 3 experiments (n>=3).

Similarly, the LCC9 (vehicle) had a crossover of 100kHz which shifted to a maximum of 400kHz when exposed to GX. When exposed to 100nM or 500nM GX, the crossover frequency shifted to 200kHz. However, when exposed to the 1μM solution, the crossover frequency shifted to 400kHz.

In addition to changes in the crossover frequency, GX-treatment resulted in alterations in the trapping efficiencies. For vehicle-treated LCC1 cells trapping efficiency at 900kHz was 33%±2.8%. GX treatments of 100nM, 500nM and 1μM GX caused graded increases in the trapping efficiency at 900kHz to 38%±2.8%, 46%±2.3%, and 56%±1.2%, respectively. At the 1MHz frequency, the LCC1 vehicle-treated cells had a somewhat higher trapping efficiency (41%±1.8%) than the LCC1 GX-treated cells (36%-27%).

In contrast, vehicle-treated LCC9 vehicle cells generally exhibited greater trapping efficiencies than GX-treated cells. The trend for 100kHz-800kHz was that with each concentration of GX, the trapping efficiency of the LCC9 cells decreased relative to the vehicle. However, at 900kHz and 1MHz the trapping efficiencies increased when exposed to GX. At 1MHz the 100nM, 500nM, and 1μM GX-treated cells had higher trapping efficiencies of 56%±1.1%, 72%±1.1%, and 68%±2.3%, respectively, versus 51%±1.2% for the vehicle.

These changes can be indicative of a change in the cell size and/or changes in the properties of the cell which relate to the electrical properties of the cell. Further experiments were carried out to understand the immediate effects of this drug on each cell line.

### 2.3.2 Morphology of Vehicle and GX-treated LCC Cells

The cell morphology and surface properties are visible aspects of the cell which play a role in the DEP response. Hence, SEM images of vehicle and GX-treated LCC1 and LCC9 cells were acquired (Figure 2.4). These images reveal changes in the cell membrane. The cell surface of LCC1 vehicle-treated cells appears generally smooth with many pores. However, the cells became ruffled with many protrusions after treatment with GX. In contrast, vehicle-treated LCC9 cells have a rough surface appearance with many surface protrusions. However, after treatment with GX, the LCC9 surfaces appear smoother with fewer surface protrusions.

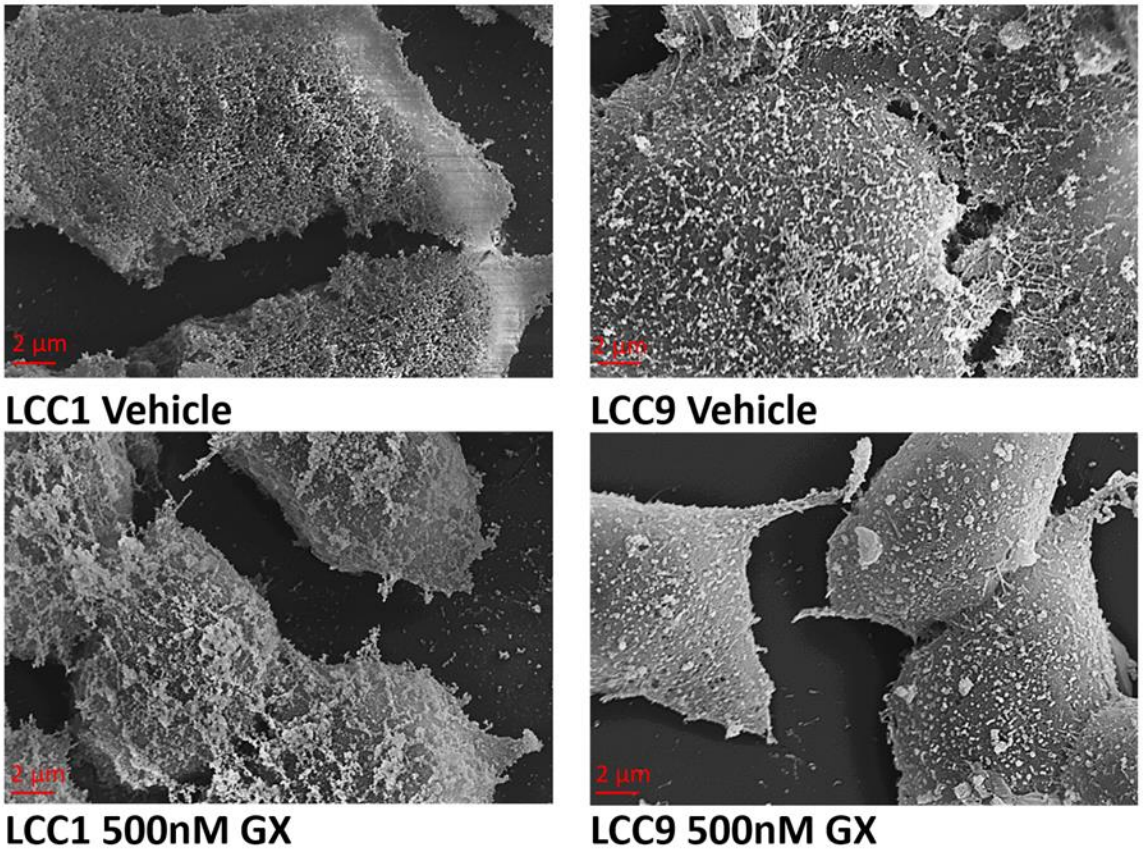


**Figure 2.4:** SEM images of vehicle control and 500nM GX-treated LCC1 and LCC9 cells with labeling below each image.

Cell size is another factor affecting the DEP force. The size of vehicle and GX-treated LCC1 and LCC9 cells were measured (Table 1). LCC9 GX-treated cells showed a significant decrease in cell size while LCC1 GX-treated cells were slightly larger than the control cells. Cell shrinkage also termed apoptotic volume decrease (AVD) is a hallmark of apoptosis and might well account for the reduced cell size observed here in response to GX [24].

| **Treatment** | **LCC1 (µm)** | **LCC9 (µm)** |
|---|---|---|
| Vehicle | 13.0 ± 2.0 | 15.0 ± 1.0 |
| GX 100nM 12 Hours | 13.5 ± 1.0 | 14.5± 1.5 |
| GX 500nM 12 Hours | 14.5 ± 1.5 | 11.0 ± 1.5 |
| GX 1µM 12 Hours | 15.5 ± 1.5 | 10.0 ± 1.0 |

**Table 1** Measured axial length cell size for vehicle and GX-treated LCC1 and LCC9 cells.

## 2.4 Discussion

The DEP force acting upon a particle is a factor of various parameters as shown by Pohl [9]. The DEP profile (trapping efficiency in this work) can provide valuable information regarding the electrical properties of the cell. One such information can be extracted from the low crossover frequency which has been observed in the results

presented in this work. Based on previously developed models [25], the low crossover frequency can be expressed as:

$$f_{x1} \approx \frac{\sqrt{2}}{2\pi r C_m}\sigma_s \tag{2.1}$$

Where r is the particle radius, $C_m$ is the membrane capacitance, and $\sigma_s$ is the conductivity of the solution the cells are suspended in. Based on this equation, at constant solution conductivity, the crossover frequency has an inverse relationship with both the cell radius and membrane capacitance.

Based on the DEP profile, studies have demonstrated that DEP can be a useful tool for drug assessment for cancer cells, while also providing insight into the cell physiology [17]. Wang et al cited membrane changes determined by DEP profiles could be used as an indication of apoptosis in HL-60 cells. The study suggests that these membrane variations are caused by changes in the membrane area, which is associated with cell size or surface ruffles, folds or microvilli alterations [15]. Variations in these parameters modifies $f_{x1}$, as described by Equation 1, such that larger membrane capacitances and particle radii result in decreased values. Other studies investigated multidrug resistance in breast cancer cells using DEP and a single-shell model to extract membrane and cytoplasm properties. Their findings suggested cytoplasmic features are more critical than membrane properties in determining drug sensitivity. These investigators found no significant change in the electrical nature of the membrane between the drug sensitive and multi-drug resistant cell lines tested [16, 17].

Based on the frequencies used for these DEP studies, these variations in cellular DEP profiles can be attributed to differing physical characteristics, such as cell size, membrane capacitance, morphology, and membrane passive conductivity [26]. As shown

by Gascoyn et al., the membrane capacitance is directly related to the degree of membrane folding which is dictated by the membrane morphology [11]. In their work, a membrane morphological score (M) is defined as

$$M = \frac{(R+P+F)}{3} \tag{2.2}$$

where R, P, and F are roughness, projections, and flattening compared to a smooth sphere, respectively. Based on this definition, we can predict that membrane capacitance would be greater in the vehicle-treated LCC9 than LCC1 cells; additionally, the vehicle-treated LCC9 cells may be slightly larger than the LCC1 cells which again would predict a higher membrane capacitance. High number of protrusions and larger membrane capacitances translate to lower crossover frequencies, as seen by the DEP profiles.

The LCC9 are strongly growth inhibited by GX while LCC1 are relatively GX insensitive to GX. The DEP profiles displayed by LCC9 and LCC1 should reflect these distinct drug sensitivities. As mentioned previously the $f_{x1}$ is inversely proportional to cell size and membrane capacitance, meaning an increase in either parameter results in a decrease in crossover frequency. The trapping efficiency has the opposite relationship where in increase in cell size or capacitance results in higher trapping values. In response to GX, LCC9 cells showed a noticeable decrease in roughness, slight increase in projection, no change in cell flattening after GX treatment, and a concentration-dependent decrease in cell size. These physical observations would be expected to increase crossover frequency and decrease trapping efficiency. In LCC1 cells, however, we see noticeable increase in cell surface roughness and slight increase in projections. However, the cells become significantly rounded compared to vehicle condition where they show a flat surface mostly. These characteristic changes for both cell lines translates to their shifts in the DEP profiles.

Assuming constant membrane permittivity and thickness, findings regarding LCC9 are consistent with the concepts that the smoother membrane and smaller cell size contributes to a higher crossover frequency. Results show that when exposed to GX, LCC9 cells decreased proportionally in size as the GX concentration was increased. In addition, the cells decreased in the number of surface protrusions when exposed to the 500nM GX treatment. The LCC9 cell's crossover frequency shifted from 100kHz to a higher frequency of 400kHz.

In contrast, GX-treated LCC1 cells, showed a higher proliferation of surface protrusions, while also shifting their crossover frequency from 700kHz to a higher value of 900kHz. The cell size increase was negligible in response to GX which is consistent with lack of apoptosis in this line (Table 1). This indicates that factors other than cell size or surface roughness contribute to the DEP profile. Because the crossover frequency for LCC1 is relatively high, changes in the cytoplasm as demonstrated by other studies [18] or membrane passive conductance [26] might be responsible.

Beyond crossover frequency, we observed that for GX-treated LCC9 cells, the overall trapping efficiency at lower frequencies (200kHz-500kHz) decreased compared to the vehicle-treated cells. In the more GX-sensitive LCC9 line, that the trapping efficiency over this range decreased with increasing concentrations of GX. This change is consistent with membrane morphology and cell size as LCC9 GX-treated cells have fewer protrusions and are smaller in size than the vehicle cells (Table 1). However, at frequencies beyond 500kHz, the trapping efficiencies became more similar to the vehicle cells, suggesting minimal or no changes in internal dielectric properties.

The LCC1 vehicle and GX-treated cells also have relatively similar trapping efficiencies for high frequencies. This may imply that the cell size and surface morphology is no longer playing as large of a role in the DEP profile as the frequencies are becoming larger. Again, this suggests that the internal cell components such as the cytoplasm are predominant influences on the DEP profile in this cell line. Supporting this are the findings that GX elicits cytoplasmic autophagosomes in LCC1 cells and that compared with LCC9 cells, autophagy plays a more prominent role than apoptosis in the toxicity of GX in this cell line [6].

We have shown the OπDEP platform was able to detect changes in the DEP profile after 12 hour GX treatment, while a traditional drug assessment method such as proliferation assays require seeding and at least 24 hour incubation prior to treatment. Similarly, DEP has shown to detect drug response in cells (after 2 hours of treatment) faster than other assessment methods such as flow cytometry which typical requires 24 hours [20]. Along with this advantage, the OπDEP platform eliminates certain common drawbacks associated with other DEP platforms. The benefits of OπDEP include reusable electrodes, passivation from cell solution (preventing interactions between the cells and electrodes) and localization of electric fields, making this a cost-effective for tool for rapid drug assessment.

Nevertheless, we acknowledge the OπDEP platform is limited by the thick passivation layer (100μm) which causes the system to require large electric field magnitudes. This translates to limited frequency ranges due to equipment restrictions and large electronics. Further limitations of the platform are discussed in Zellner et al [22]. In addition, as this study evaluated frequencies at 100kHz intervals, the DEP profiles

generated are only discrete values. In order to produce a more continuous profile, additional data points should be added for future studies.

Further studies need to be performed to better define the relationships which link DEP characteristics and the cellular alterations which lead to each kind of profile. Additionally, to evaluate the predictive nature of the trapping efficiency and crossover frequency DEP analyses with unknown cell samples should be conducted. Future directions for this platform encompass the fabrication of multiple channels on a single chip in order to enable simultaneous differential measurements for various trials, leading to more robust results and reduced experimental time.

## 2.5 Conclusion

By utilizing the previously established OπDEP platform, we have shown that different cell lines exhibit different and distinctive trapping profiles. When the cells were exposed to a chemical stimulus, the initial trapping frequency and the trapping efficiencies vary. The treated cells are clearly distinguished from their vehicle counterparts based on shifts in their DEP profiles, exhibiting the applicability of this method for drug sensitivity studies. These shifts in the DEP profiles can be further examined to determine the underlying biophysical changes due to drug exposure. Thus, this method of analysis provides greater insight into the biophysical changes of cells in a rapid, label-free assay. Additionally, the inherent benefits of the OπDEP platform such as reusable electrodes and separation between the electrodes and sample shows the platform's tremendous potential for drug sensitivity studies.

## 2.6 References

[1] Clarke, R., Liu, M. C., Bouker, K. B., Gu, Z., Lee, R. Y., Zhu, Y., Skaar, T. C., Gomez, B., O'Brien, K., Wang, Y., Hilakivi-Clarke, L. A., *Oncogene* 2003, *22*, 7316-7339.

[2] Thompson, A., Brennan, K., Cox, A., Gee, J., Harcourt, D., Harris, A., Harvie, M., Holen, I., Howell, A., Nicholson, R., Steel, M., Streuli, C., *Breast Cancer Research* 2008, *10*, 1-25.

[3] Brünner, N., Boysen, B., Jirus, S., Skaar, T. C., Holst-Hansen, C., Lippman, J., Frandsen, T., Spang-Thomsen, M., Fuqua, S. A. W., Clarke, R., *Cancer Research* 1997, *57*, 3486-3493.

[4] Lee, A. V., Oesterreich, S., Davidson, N. E., *JNCI: Journal of the National Cancer Institute* 2015, *107*, djv073-djv073.

[5] Lv, Y., Zeng, L., Zhang, G., Xu, Y., Lu, Y., Mitchelson, K., Cheng, J., Xing, W., *Int J Nanomedicine* 2013, *8*, 2333-2350.

[6] Schwartz-Roberts, J. L., Shajahan, A. N., Cook, K. L., Warri, A., Abu-Asab, M., Clarke, R., *Mol Cancer Ther* 2013, *12*, 448-459.

[7] Stylianou, S., Clarke, R. B., Brennan, K., *Cancer Res* 2006, *66*.

[8] Huang, H. E., Chin, S. F., Ginestier, C., Bardou, V. J., Adélaïde, J., Iyer, N. G., Garcia, M. J., Pole, J. C., Callagy, G. M., Hewitt, S. M., Gullick, W. J., Jacquemier, J., Caldas, C., Chaffanet, M., Birnbaum, D., Edwards, P. A., *Cancer Res* 2004, *64*.

[9] Pohl, H. A., *Journal of Applied Physics* 1951, *22*, 869-871.

[10] Pethig, R., *Advanced Drug Delivery Reviews* 2013, *65*, 1589-1599.

[11] Gascoyne, P. R. C., Shim, S., Noshari, J., Becker, F. F., Stemke-Hale, K., *ELECTROPHORESIS* 2013, *34*, 1042-1050.

[12] Gascoyne, P. R., Shim, S., *Cancers (Basel)* 2014, *6*, 545-579.

[13] Khoshmanesh, K., Akagi, J., Nahavandi, S., Skommer, J., Baratchi, S., Cooper, J. M., Kalantar-Zadeh, K., Williams, D. E., Wlodkowic, D., *Analytical Chemistry* 2011, *83*, 2133-2144.

[14] Yusvana, R., Headon, D. J., Markx, G. H., *Biotechnology and Bioengineering* 2010, *105*, 945-954.

[15] Wang, X., Becker, F. F., Gascoyne, P. R., *Biochimica et Biophysica Acta* 2002, *1564*, 412-420.

[16] Labeed, F. H., Coley, H. M., Thomas, H., Hughes, M. P., *Biophysical Journal* 2003, *85*, 2028-2034.

[17] Coley, H. M., Labeed, F. H., Thomas, H., Hughes, M. P., *Biochim Biophys Acta* 2007, *1770*, 601-608.

[18] Henslee, E. A., Torcal Serrano, R. M., Labeed, F. H., Jabr, R. I., Fry, C. H., Hughes, M. P., Hoettges, K. F., *Analyst* 2016, *141*, 6408-6415.

[19] Mulhall, H. J., Cardnell, A., Hoettges, K. F., Labeed, F. H., Hughes, M. P., *Integr Biol (Camb)* 2015, *7*, 1396-1401.

[20] Kumar, R. T. K., Liu, S., Minna, J. D., Prasad, S., *Biochim Biophys Acta* 2016, *1860*, 1877-1883.

[21] Chou, C., Tegenfeldt, J. O., Bakajin, O., Chan, S. S., Cox, E. C., Darnton, N., Duke, T., Austin, R. H., *Biophysical Journal* 2003, *83*, 2170-2179.

[22] Zellner, P., Shake, T., Sahari, A., Behkam, B., Agah, M., *Anal Bioanal Chem* 2013, *405*, 6657-6666.

[23] Flanagan, L. A., Lu, J., Wang, L., Marchenko, S. A., Jeon, N. L., Lee, A. P., Monuki, E. S., *STEM CELLS* 2008, *26*, 656-665.

[24] Bortner, C. D., Cidlowski, J. A., *Phil. Trans. R. Soc. B* 2014, *369*, 20130104.

[25] Pethig, R., Talary, M. S., *IET Nanobiotechnol* 2007, *1*, 2-9.

[26] Pethig, R. R., *Dielectrophoresis: Theory, Methodology and Biological Applications*, John Wiley & Sons 2017.

[27] Soltanian-Zadeh, S., Kikkeri, K., Shajahan-Haq, A. N., Strobl, J., Clarke, R., Agah, M., *ELECTROPHORESIS* 2017, *38*, 1988-1995.

# 3 Dielectrophoretic properties distinguish responses to estrogen and fulvestrant in breast cancer cells

This chapter was reproduced from a manuscript under review in Sensors and Actuator B.

## 3.1 Introduction

Dielectrophoresis (DEP) has shown to be a versatile method to characterize cells based on their inherent biophysical properties [1]. DEP operates based on differences in dipoles induced in cells upon the application of AC electric fields. These differences are caused by variances in cell physiology such as size, membrane capacitance, and cytoplasm conductivity [2-4]. Thus, cells can be characterized by their behavior under DEP forces. Cellular DEP profiles have been used as a label-free alternative to flow cytometry and magnetic bead technologies for cell sorting [5-9]. DEP has been applied experimentally in biomedicine for the evaluation of drug efficacy, toxicants, stem cell research, and cancer cell detection [8, 10, 11]. Previous work in this laboratory demonstrated the use of the πDEP platform in the characterization of breast cancer cell lines to better understand their response to the anti-cancer Bcl2 inhibitor, Obatoclax [3].

Understanding the causes of therapy resistance and identification of drug-resistant tumor cells are crucial to improving cancer management. Tumors which initially respond to anti-cancer drugs, often develop resistance. The unchecked spread of these metastatic lesions most often results in cancer-related death. ER are present in 70-80% of breast tumors, and cellular pathways activated by the binding of E2 to the ER are mitogenic in many of these tumors [12]. Interruption of the E2-ER signaling pathway is a primary goal of ET. Thus, current first-line therapeutic options include ET with aromatase inhibitors (AI) that inhibit the biosynthesis of E2 such as anastrazole, exemestane and letrozole alone or in combination with tamoxifen (Tam), a selective ER modifier (SERM), remains

the first line ET for premenopausal women [12, 13]. Patients whose ER+ tumors fail to respond to these treatments (intrinsic resistance) or whose ER+ tumors recur (acquired resistance) can opt to receive additional ET with Ful, a selective ER degrader (SERD) and/or receive a cytotoxic chemotherapy regimen. Panels of genetic markers, Ki67 immunohistochemistry, tumor size, grade, and lymph node involvement are used to assess tumor recurrence risk [14-16]. However, there is still a need for a biomarker to predict the Ful-responsiveness of cells. This would greatly assist in directing the most effective treatment to individual patients, since Ful is non-inferior to Ais and is often given as a second line treatment in combination with cdk4,6 inhibitor such as palbocicclib.

The mechanisms that confer resistance to ET and the role of ER in this process have been intensively investigated [17]. The growth promoting activities of E2 are mediated primarily through the ER-alpha molecular subtype encoded by the ESR1 gene. Clinically, tumors with higher levels of ER-positivity, as determined by immunohistochemistry are associated with a greater probability of ET sensitivity. Intrinsic resistance may be linked more closely to lower levels of ER [18]. In addition, ER activation of alternative, mitogenic growth factor signaling pathways and stimulation of PI3K pathways can lead to E2-independent breast tumor growth [19]. Detection of ESR1 mutations leading to ER proteins with altered function are one cause of acquired resistance to an AI but likely not an antiestrogen. For example, mutated ER can result in constitutively active ER that no longer require E2 for function. Metastases that express these constitutively activated forms of ER no longer respond to an AI, but do retain sensitivity to Tam and Ful, as the latter will promote degradation of the mutant ER [20, 21]. Several studies, where ET

resistance in patients has been investigated in long-term follow-up, show that tumor recurrence may also be a result of the aggressiveness of the cancer rather than acquired resistance [22].

To date no studies have addressed whether there are differences in biophysical properties of ET-s and ET–r cells. Here, we have used DEP to study drug responsiveness in human breast cell lines. We used the LCC1/LCC9 cell line pair because they are well-characterized and show sensitivity and resistance to Ful. The LCC1 cell line is an MCF-7 derivative selected from MCF-7 cells during propagation *in vivo* as mouse xenografts in the absence of E2 [23]. While LCC1 cells can grow independently of E2, their proliferation is weakly stimulated by E2, but inhibited by Tam and Ful [17]. LCC1 cells represent an intermediate stage in ET resistance in which growth is not responsive to AI therapy, but responses to Tam and Ful are seen. LCC9 cells were selected *in vitro* from an LCC1 cell population by their resistance to Ful. LCC9 cells are also cross-resistant to Tam [17]. Proliferation of LCC9 cells is E2-independent even though they are ER+ and their ER protein shows activity in the presence of E2 [24].

Here, we examined the DEP response of LCC1 and LCC9 cells to Ful- exposures for 12, 24, 48, and 72 hours. The πDEP platform was used to characterize the electrical changes of the cells in response to the Ful chemical stimulus. Specifically, DEP excitations utilized to trap cells around electric field gradient maxima (positive DEP or pDEP) in the πDEP microfluidic channel. A frequency sweep was conducted to analysis the pDEP response of the cells based on their f0 and trapping efficiencies. For this study, f0 was quantified as the frequency where the DEP force experienced by the cells switched from negative DEP (attraction to electric field gradient minima) to pDEP. Gene

expression analysis and cell morphology imaging were performed to allow the DEP results to be compared with conventional drug assessment methods, while providing additional insight into biophysical changes.

## 3.2 Methods

### 3.2.1 Device Fabrication

The πDEP devices were fabricated using a simplified process which was previously presented in [2]. Figure 1B depicts the fabrication process for the electrodes and microfluidic chip. The reusable electrodes were fabricated on a 500 µm thick glass substrate through photolithography and physical vapor deposition of chrome/gold. Following deposition, a lift-off process was employed to create a pair of electrodes with a width and horizontal spacing of 1000 µm and 600 µm, respectively. Connection wires were then soldered onto the electrode ends as shown in Figure 1B.

The microfluidic chip was fabricated by first patterning a <100> silicon wafer with photoresist and developing it to create a negative silicon master. Liquid polydimethlsiloxanne (PDMS) (Dow Corning, MI, USA) and curing agent were combined in a 10:1 ratio and poured into the silicon master. This mixture was degassed in a vacuum chamber for 1 hour and then cured at 100°C for 45 minutes to allow the PDMS to solidify. The solidified PDMS was then removed from the silicon master and cut. Inlets and outlets were punched on each chip and then bonded to a 100 µm thick #0 cover glass slide (Electron Microscopy Sciences, PA, USA) which acts as the passivation layer between the fluidic channel and the electrodes. The microfluidic chip was placed directly above and between the electrodes with minimal alignment and attached using tape. The πDEP chip

has insulating pillars 100 μm in diameter with edge-to-edge 30 μm spacing with a depth size 40 μm for the entire microfluidic channel.

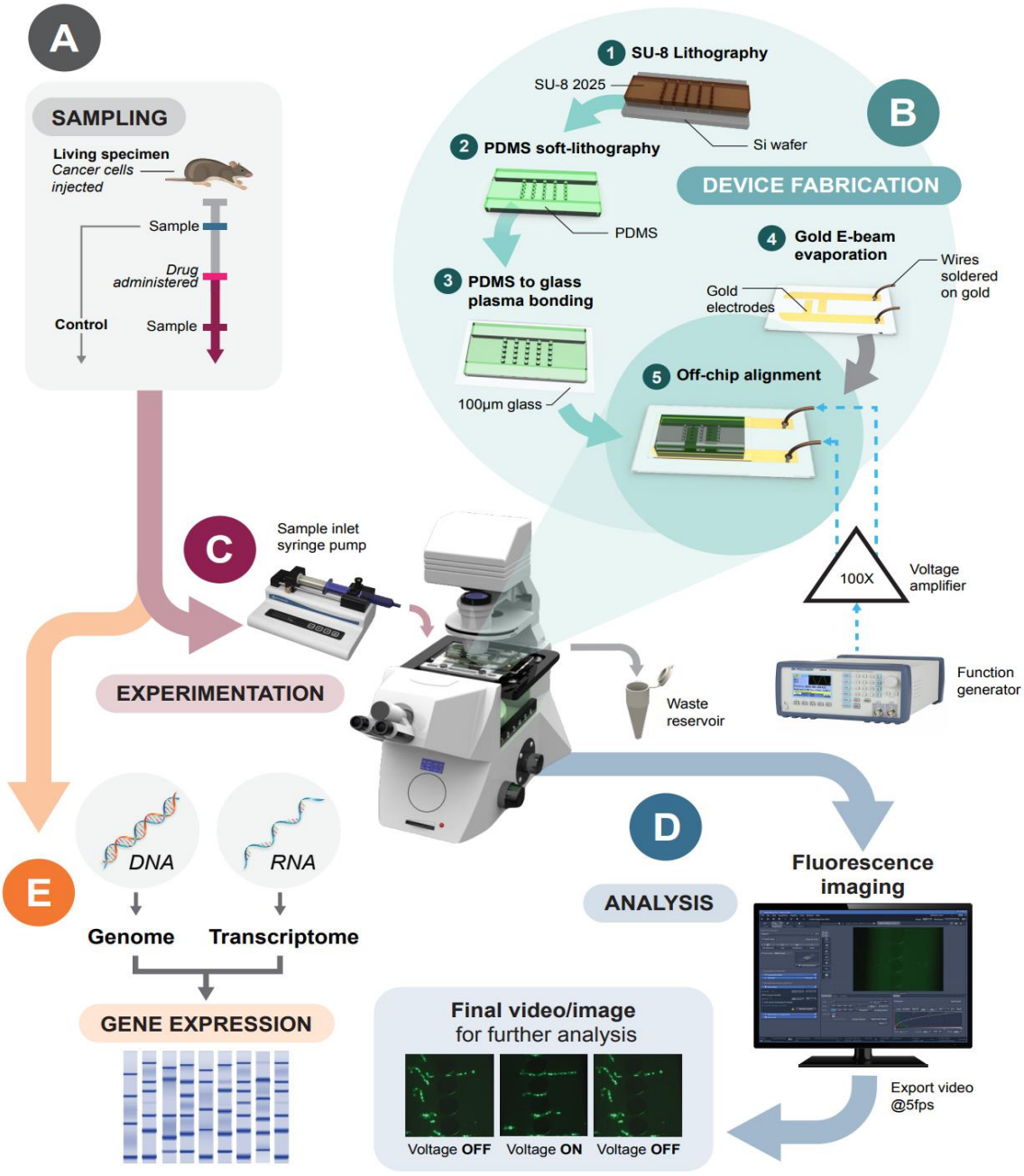


**Figure 3.1:** Overview of methodology employed for experimentation. A represents the methods used to extract cancer cell lines from mouse xenografts that led to the LCC1 cell line. The LCC9 cells were derived from LCC1 in vitro via growth in Ful. Both cell lines were maintained *in vitro* and processed for DEP or gene analysis. B1-5 depicts the

fabrication procedure for the OπDEP device. C is the experimental setup for the DEP analysis. E2 is a rendition of the gene expression investigation.

### 3.2.2 Cell Culture and Treatments

LCC1 and LCC9 ER+ breast cancer cells were obtained from the Tissue Culture Shared Resources at Georgetown University Medical Center, Washington, DC. Cells were maintained in T-25 flasks in Minimum Essential Medium (MEM Richter's modification) (Life Technologies, NY, USA) and grown in 5% charcoal-stripped Calf Serum Charcoal Stripped (Valley Biomedicals, VA, USA) and antibiotics, 100 U/mL penicillin and 100µg/mL streptomycin (Mediatech, VA, USA), at 37°C in a humidified 5% CO2 incubator.

Stock solutions of Ful and E2 were prepared in vehicle (ethanol), stored at -20°C, and diluted in culture media to the desired concentrations. The frozen stock solutions were thawed prior to treatment. LCC1 and LCC9 cells were treated with 500 nM Ful, 10 nM E2, or a vehicle control of 0.1% vehicle for 12, 24, 48, or 72 hours.

Following treatment, cells were harvested with trypsin and fluorescently tagged with 5 µM 5-chloromethylfluorescein diacetate (Cell Tracker Green CMFDA Dye) (Life Technologies, NY, USA) in a 113±0.54 µS/cm DEP buffer containing 8.5 g sucrose (Sigma Aldrich, MO, USA) and 0.725 mL MEM (Life Technologies, NY, USA) in 100mL of deionized water [8]. Cells were washed twice by centrifugation (1500 rpm for 10 minutes) and then re-suspended in the DEP buffer to remove residual drug (CMFD) and to avoid alterations in the solution conductivity. The conductivity was verified using a Conductivity Meter SG7 (Mettler Toledo, Scherzenbach, Switzerland). The final cell concentration in the samples was adjusted to $2\times10^6$ cells/mL for all experiments based on quantifications

made using a hemocytometer. Cell viability in these suspensions was greater than 90% as determined by Trypan blue dye exclusion.

### 3.2.3 Experimental Setup

PDMS-based microfluidic devices were placed under vacuum for at least 30 minutes prior to experimentation to reduce priming issues. After vacuum treatment, a bovine serum albumin (BSA) solution was injected into the microfluidic channel for 2 minutes to coat the channel and prevent cell adhesion. BSA was flushed out with the DEP buffer. An overview of the device operation is depicted in Figure 1. A 1 mL syringe containing the fluorescently tagged cell solution was then connected to the chip. The solution was driven through the channel at a constant flow rate of 20 µL/hr, using a Pump11 Elite syringe pump (Harvard Apparatus, MA, USA). Electrodes were excited over a range of 50 kHz and 100 kHz-1 MHz at 80 $V_{peak\text{-}to\text{-}peak}$ through the use of a 50 MHz function generator (4079 50 MHz Dual-Channel Arbitrary Waveform/Function Generator, B&K Precision, CA, USA) and a voltage amplifier (A800DI Voltage Amplifier, FLC Electronics AB, Sweden). Excitation induced DEP forces caused by AC electric field, resulting in cell trapping around the pillars. A Zeiss Axio Observer.Z1 inverted epifluorescence microscope (Germany) with a 10X objective lens was used to image the microfluidic channel.

Duration of each trial was 25 seconds to ensure time for 20 second DEP excitation and cell release, and to allow cells to return to a continuous flow. Trapping efficiencies were calculated as the ratio of trapped cells to the total number of cells in each run. The f0 was determined to be the frequency at which the cells began to experience positive DEP and were pulled to the higher gradients in the electric field around the posts. Details of the experimental setup and methodology are described in [3].

### 3.2.4 Scanning Electron Microscope Sample Preparation

Scanning Electron Microscope (SEM) images were taken to assess the cell morphology with (72 hours) and without drug treatments. Cells were fixed onto glass slides using a 4% formaldehyde solution in phosphate-buffered saline (PBS, Baker, PA, USA). Samples were post-fixed in 1% osmium tetraoxide, serially dehydrated in a graded ethanol series (15%, 30%, 50%, 70%, 95%, 100%), and critical point dried. The sample was then sputter-coated with a thin layer of gold and imaged using a Carl Zeiss EVO 40 SEM (Germany) [3].

### 3.2.5 Cell Size Measurement

Cells under suspension were measured using images captured by the epifluorescence microscope and analyzed using the image processing software, Zen Pro Blue (Germany). Fifty cell sizes were measured for each treatment type for both cell lines. Final cell sizes are reported in Table 2 [3].

### 3.2.6 Gene Expression and Data Analysis

Gene expression analysis was performed using three biological replicates each from LCC1 and LCC9 cells using an Agilent human gene expression microarray (4x44K) at the Genomics and Epigenomics Shared Resources at Georgetown University Medical Center. Briefly, total RNA was extracted using the RNeasy kit (Qiagen, Valencia, CA, USA). RNA labeling and hybridization were performed according to the Agilent protocol. For each experiment, fragmented cRNA was hybridized in triplicates to arrays (Agilent, Santa Clara, CA). Data analysis included pre-processing of the probe-level Agilent data. Gene expression raw data were normalized using the normexp and quantile method as implemented in the R limma package [25]. The same package was used for the following statistical analysis.

### 3.2.7 Statistical Significance Analysis

For multiple group comparisons, Student-Newman-Keuls method comparison test was applied following ANOVA. F0 results were considered to be significantly different at $p < 0.05$. Statistical analysis was carried out using the Sigma Plot software (Jandel Scientific, SPSS, Chicago, IL, USA) [3].

## 3.3 Results

### 3.3.1 DEP Characterization

A time course study of the response of LCC1 and LCC9 ER+ breast cancer cells to E2 and Ful was performed using the OπDEP platform (Figure 3.2) Each cell line in response to treatment with vehicle control, E2 or Ful showed unique DEP profiles. Although both cell lines saw gradual, time-dependent shifts in their f0 that were evident at the earliest time point, 12 hours, the cell lines were biophysically distinct as determined by DEP. LCC1 vehicle-treated cells had an initial f0 of 700 kHz which decreased to lower frequencies after treatments. Ful treatment significantly shifted the LCC1 f0 to 300 kHz, and a smaller decrease to 600 kHz when exposed to E2. In contrast, the f0 of LCC9 cells shifted from 100 kHz to significantly higher values of 700 kHz and 800 kHz after Ful and E2 treatment, respectively.

Additionally, Ful and E2 treatment resulted in alterations in the trapping efficiencies relative to the vehicle. At 800 kHz, the trapping efficiency of LCC1 cells fluctuated between 40% ± 2.0% and 20% ± 3.0% over the 0-72 hour time course for all of the treatments. At 800kHz, the trapping efficiency of LCC9 cells dropped from about 80% to about 60% for vehicle and Ful treatments. The E2 treated cells decreased to 10% ± 2.6% after 72 hours.

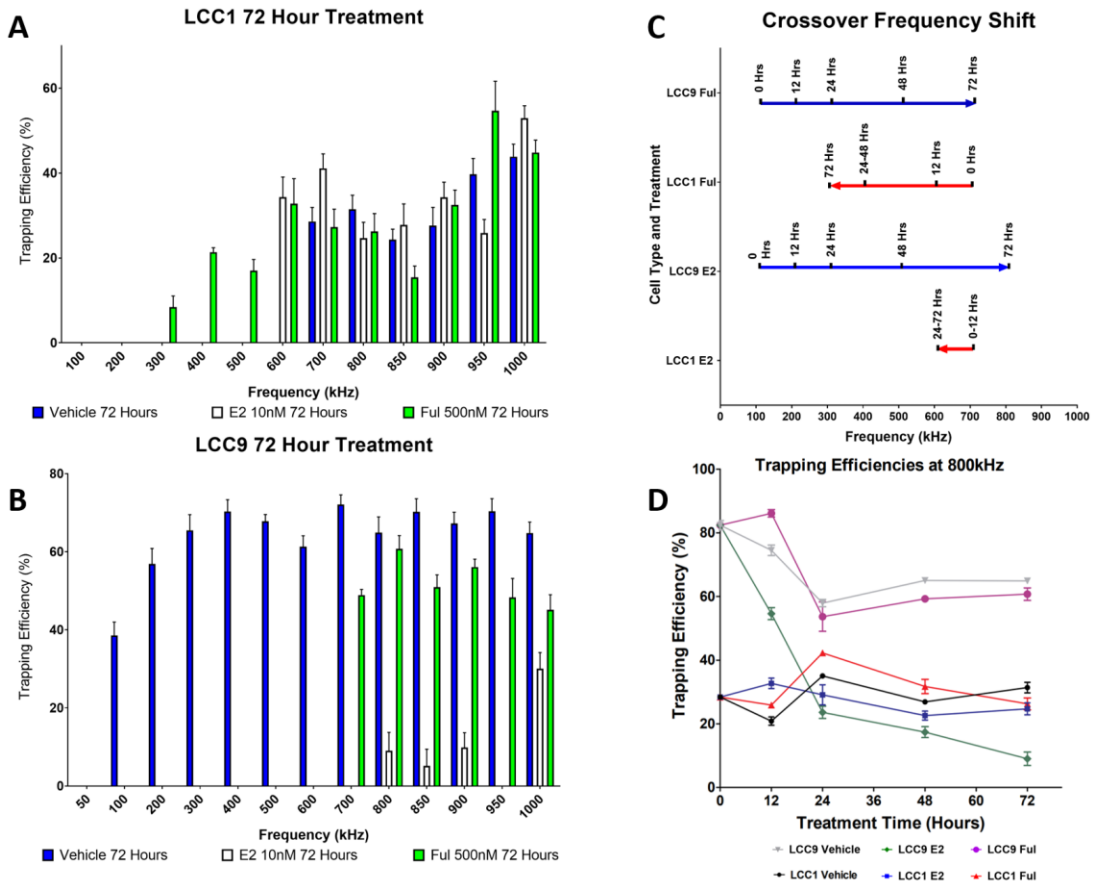


**Figure 3.2:** DEP profiles for (A) LCC1 and (B) LCC9 cells following 72 hour treatments. (C) Visual representation of f0 shifts for E2 and Ful treated LCC1 and LCC9 cells. Note that 0 hour f0 is based on vehicle treatment. (D) Trapping efficiency shifts for vehicle, E2 and Ful for LCC1 and LCC9.

### 3.3.2 Cell Morphology

SEM images of vehicle, E2, and Ful treated LCC1 and LCC9 cells were taken (Figure 3.3) to correlate visible surface modifications to the DEP profiles. The images in Figure 3.3 were chosen from a sample of approximately 50 cells imaged after 72 hours of treatment. Representative images for single cells are shown at 10,000X magnification for the cell surface as recorded for each treatment. The cell surfaces of the LCC1 vehicle treated cells were ruffled with protrusions and generally porous. When exposed to E2, the

LCC1 cells grew longer protrusions and developed spherical lumps on the surface. In contrast, when treated with Ful, LCC1 cells displayed significantly fewer surface protrusions and the cells became more porous.

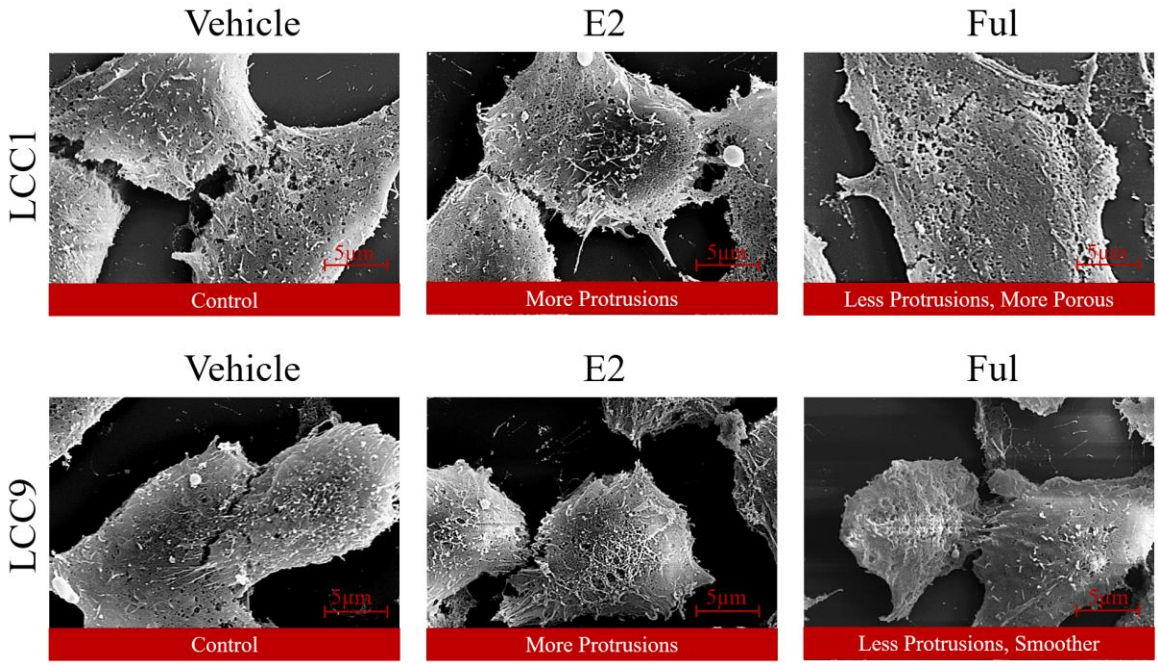


**Figure 3.3:** SEM images of vehicle, E2, and Ful treated LCC1 and LCC9 cells after 72 hours of drug exposure.

Vehicle treated LCC9 cells had a rough surface morphology with many surface protrusions. While LCC9 cells exhibited some porous-like features, their overall surface was less porous and had smaller openings when compared with LCC1 vehicle treated cells. Similar to the LCC1 E2 treatment, the LCC9 cells' surface became more rough with longer protrusions after exposure to E2. Additionally, the cells became more rounded. However, after Ful treatment, the LCC9 surfaces appeared smoother, non-porous, and exhibited fewer surface protrusions.

With respect to cell size, treatment with E2 or Ful had its own unique effects on the two cell lines. Cell size mean and mode values following treatment with vehicle, E2 or Ful

for LCC1 and LCC9 cells for each time period are displayed in Table 2.

| Treatment | Size Type | LCC1 (µm) | | | | LCC9 (µm) | | | |
|---|---|---|---|---|---|---|---|---|---|
| | | 12 Hr | 24 Hr | 48 Hr | 72 Hr | 12 Hr | 24 Hr | 48 Hr | 72 Hr |
| Vehicle (EtOH) | Mean | 13.0 ± 2.0 | 13.0 ± 1.0 | 13.0 ± 2.5 | 13.0 ± 2.0 | 14.0 ± 1.0 | 14.0 ± 0.5 | 14.0 ± 1.0 | 14.5 ± 1.5 |
| | Mode | 13.0 | 13.5 | 13.0 | 13.0 | 14.0 | 14.0 | 13.5 | 14.0 |
| E2 | Mean | 13.0 ± 2.0 | 13.5 ± 1.5 | 14.0 ± 1.0 | 14.0 ± 1.5 | 14.0 ± 2.0 | 13.5 ± 1.5 | 12.5 ± 0.5 | 10.5 ± 1.0 |
| | Mode | 14.0 | 14.0 | 15.5 | 15.0 | 14.0 | 12.5 | 11.5 | 10.0 |
| Ful | Mean | 14.0 ± 1.5 | 15.0 ± 1.5 | 15.5 ± 1.0 | 16.0 ± 2.5 | 14.0 ± 0.5 | 13.0 ± 1.5 | 12.5 ± 1.0 | 11.0 ± 1.5 |
| | Mode | 15.0 | 15.5 | 16.0 | 17.0 | 14.5 | 14.0 | 12.0 | 11.0 |

**Table 2** The mode and mean axial length cell size ± standard error of means for vehicle, E2 and Ful treated LCC1 and LCC9 cells. Data shown are the mean ± standard error of means for 50 cells.

Treatment with vehicle alone had no effect on cell size in either cell line as assessed by the mean or the mode longest axial length. However, when exposed to the E2, the average LCC1 cell size enlarged slightly from 13.0 ± 2.0 µm to 14.0 ± 1.5 µm and the modal cell size increased from 14 µm to 15 µm. In contrast, the mean LCC9 cell size decreased in response to E2 from 14.0 ± 2.0 µm to 10.5 ± 1.0 µm at 12 hours and 72 hours, respectively with a corresponding change in the modal cell size. Additionally, when exposed to Ful, LCC1 cells enlarged to 16.0 ± 2.5 µm, while LCC9 Ful-treated cells decreased in mean size (11.0 ± 1.5 µm).

### 3.3.3 Gene Expression

An unbiased differential RNA expression strategy was performed to investigate the biochemical correlates of the differential DEP properties of LCC1 and LCC9 cells. IPA (Ingenuity pathway analysis) was used to evaluate the gene set enrichment of those differentially expressed RNA in approximately 200 known signaling pathways in these two cell lines. The Z-score patterns of the canonical pathways indicated that global pathways were essentially identical in these two cell lines under control (vehicle treated) conditions. Pathway analysis therefore confirmed that LCC1 and LCC9 cell lines are closely related genetically , a finding that is consistent with the derivation of the LCC9 as a Ful-resistant variant of LCC1 cells [26, 27]. The only pathway-specific change observed involved six molecules associated with the aryl hydrocarbon (Ah) receptor signaling pathway. This pathway exhibited a weakly positive Z score of 0.447. Conceptually, the molecules identified within this pathway might contribute to the altered E2 and Ful responsiveness in the LCC9 cells. Expression of ESR1 (encoding ER-alpha), CCNE (cyclin E2), CCND3 (cyclin D3), and GSTP1 (glutathione S-transferase pi 1) were downregulated mRNAs and CTSD (cathepsin D) and nuclear receptor interacting protein 1 (NRIP1) mRNAs were upregulated in LCC9 relative to the LCC1 cells.

Differential mRNA expression in LCC1 and LCC9 cells was also examined at the individual gene level using a filter to highlight the changes that were the most statistically significant ($p \leq$ E-06) as well as the greatest in magnitude. The relative expression of mRNAs (LCC9:LCC1) measured using the named gene probes are plotted as a function of p value in Figure 3.4. In the upper panel, the red bars indicate each mRNA whose expression was significantly increased in the Ful-r LCC9 cells compared to the LCC1 cells. All bars marked with a small dot are expressed in human breast tumors [28-32]. Here, the

statistically most significant change was the 7-fold relative increase in IL20 mRNA expression in LCC9 cells. In breast cancer patients, expression of this pro-inflammatory cytokine is associated with tumor invasiveness and poor clinical outcome (Hsu et al. 2012). Aschaete-scute homology 1 (ASCL1) mRNA which encodes a basic helix-loop-helix (bHLH) transcription factor showed the greatest relative change in magnitude [33]. There was a 13-fold rise in ASCL1 mRNA expression in the Ful-r LCC9 cells; ASCL1 upregulated expression is associated with tumors having neuroendocrine differentiation character and invasive potential [34]. Neuroendocrine breast cancer represents 1-5% of all breast cancer cases, but has a relatively poor prognosis despite expression of rather indolent biomarkers [35, 36]. These two differentially overexpressed mRNAs in LCC9 cells, IL20 and ASCL1, are overexpressed in aggressive tumors in patients, and thus LCC9 cells serve as a good model for DEP profiling of aggressive breast cancer.

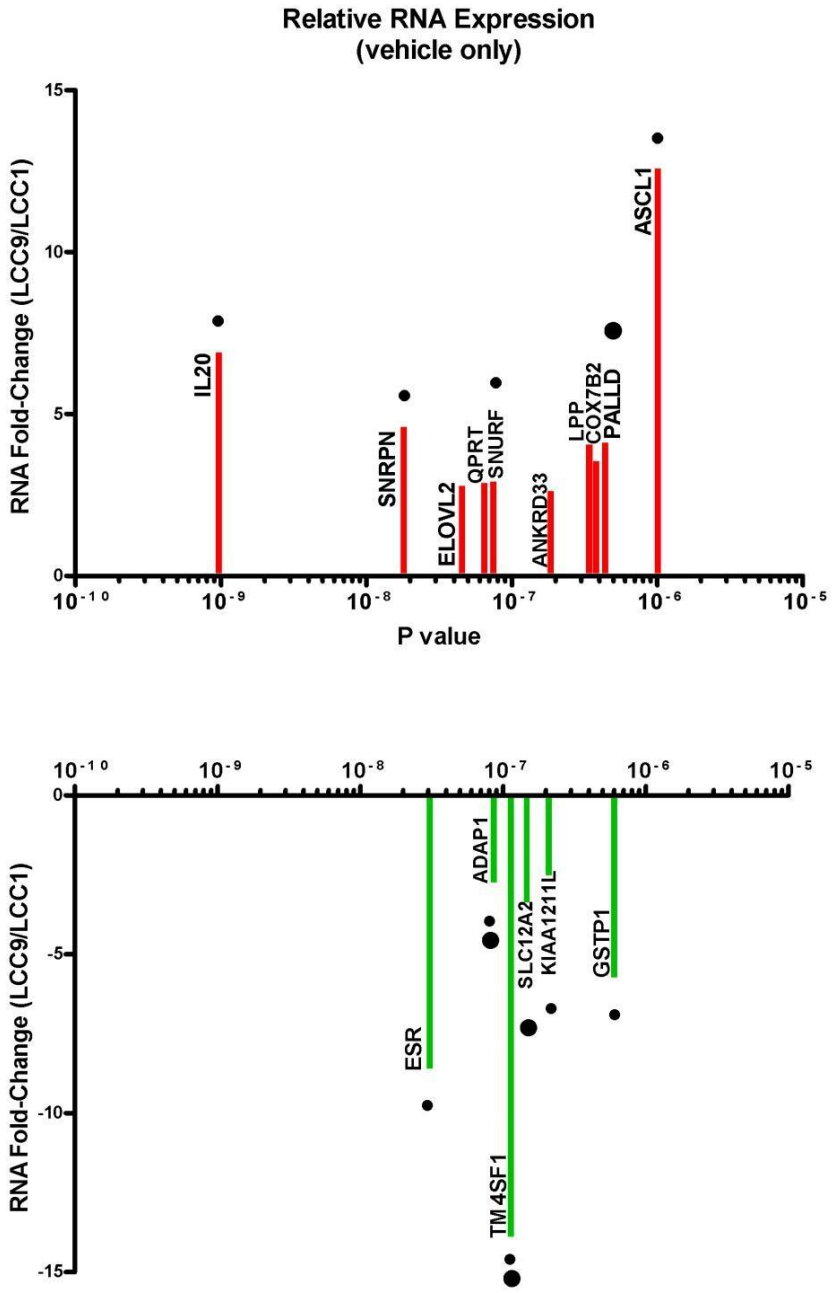


**Figure 3.4:** Ingenuity Analysis of mRNA Expression in LCC1 and LCC9 Cell Lines. Red bars indicate relative overexpression of mRNA in LCC9 cells compared to LCC1 cells. Green bars indicate relative overexpression of mRNA in LCC1 cells compared to LCC9 cells. Each bar is labeled with the gene corresponding to the mRNA. Small dots

indicate mRNAs encoding proteins with known functions in breast cancer; large dots indicate mRNAs encoding proteins with functions that potentially influence cellular DEP properties.

In the lower panel of Figure 3.4, the green bars show the mRNAs that are relatively overexpressed in the Ful-s LCC1 cells. Here Figure 3.4 shows the most significantly overexpressed (8.6-fold) mRNA in LCC1 cells is that of the ER-alpha (ESR1) ($p<3.08E-08$). As an independent studies have previously showed that ER-alpha RNA and protein expression are decreased in LCC9 cells [37, 38], the confirmation of decreased ESR1 mRNA expression here serves to validate the gene array analysis. In addition, expression of transmembrane 4 L6 antigen family member 1 (TM4SF1) mRNA is 14-fold higher in the LCC1 cells than LCC9 and constitutes the most highly overexpressed mRNA in LCC1 cells relative to LCC9 cells. TM4SF1 is a tetraspanin molecule located in the plasma membrane that promotes proliferation, invasion and metastasis in various forms of cancer and supports nanopodia and lamellipodia formation in endothelial cells [39, 40]. As in the upper panel, mRNAs marked with a small dot are expressed in clinical human breast tumors [41, 42]. The larger dots mark mRNAs encoding proteins that might impact the cell's DEP behavior based on their known biochemical properties. These include TM4SF1, Arf-GTPase-activating protein family member 1 (ADAP1), and solute carrier family 12 Na+/K+/Cl- transporter member 2 (SLC12A2). The top results of the gene array analysis are presented in Appendix 1.

## 3.4 Discussion

The value of DEP in the assessment of cancer cell properties has not been fully realized despite initial studies suggesting that this is a promising technology for

investigation. The sensitivity of DEP in detecting apoptotic cell death via changes in surface phosphatidylserine residues is superior to that of the standard DNA fragmentation assay [43]. Cristofanilli et al showed that DEP was sufficiently sensitive to distinguish overexpression of HER-2/neu on the plasma membrane of MCF-7 human breast cancer cells [44]. Here we found that DEP monitoring of responses to ER ligands can distinguish Ful-s and Ful-r derivatives of MCF-7 cells. To gain insights into biochemical pathways that might mediate the cellular changes detected by DEP, surface morphology, cell size, and gene expression data were analyzed.

As the DEP force is governed by the Clausius-Mossotti relation, the generated DEP profiles can be used to extract information regarding the electrical properties, or polarizability, of the molecules that make up the cells [1]. Previously developed models indicate that the first f0 is directly proportionally to the conductivity of the suspending media and inversely related to the particle size and membrane capacitance [4, 45, 46]. As the suspending media was held constant for this study, size and membrane capacitance alternations are the primary parameters which impact the changes in f0.

The DEP profiles show that LCC1 and LCC9 cells shifted their f0 when exposed to the E2 and Ful. As indicated by previously developed models of the Clausius-Mossotti factor, cell size is inversely proportional to the first f0 [4]. In accordance with this theory, the relative shifts in the first f0 for the LCC1 cells when exposed to E2 and Ful correspond to the relative increases in the cells size. This increase was gradual over the time intervals and corresponded to the gradual f0 shifts.

Additionally, these shifts can be a result of changes in the membrane capacitance. Dopp et al. found that cell surface morphology such as microvilli, porosity, fiber, cell

flattening, folds, and blebs [47] will impact the capacitance. Increases in microvilli and other surface protrusions resulted in higher membrane capacitances as they effectively increase the total surface area of the cell. Figure 3.3 indicates that E2 exposed LCC1 cells were ruffled with more densely populated and longer microvilli than the vehicle. The Ful treated cells grew more porous and flattened, thus increasing their total surface area. These changes correspond to higher membrane capacitances and thus may have resulted in the lower f0.

In contrast, LCC9 saw a significant increase in their f0 when exposed to both E2 and Ful. These shifts corresponded to their decrease in size as E2 cells decreased to a greater extent and had a larger frequency shift than the Ful treated cells. As the LCC9 cells grow independent of E2 and are resistant to the Ful, the apoptosis volume decrease (AVD) phenomena is not a viable explanation for the decrease in the cell size. However, from Figure 3.3 we can observe that the cells become more rounded when treated with E2 and Ful, and effectively decrease the axial cells size. As the measurements were only taken on one plane, the shifts in the overall volume cannot be asserted. However, we can oversee that the treatments caused the loss of surface protrusions and smoother surfaces for both treatments. This correlates to the decreases in the membrane capacitance and the increases in f0.

In addition to the f0 alterations, both cell lines presented variations in their trapping efficiencies when exposed to the treatments. Trapping efficiency is based on the force balance between Stoke's drag force and the DEP force. Within the channel, the DEP force is greatest where there are higher gradients in the field (close to the pillars), and gradually reduces as the field gradients become smaller. Thus, the path of the particle as it passes

through the channel affects which force dominates. However, assuming that the path of the particles for each experiment is equally random, other factors such as the cell membrane capacitance, cell size, and cytoplasm conductivity can account for variations in trapping efficiency. Cell features such as protrusions and microvilli. can contribute to larger cell sizes which allows them to experience larger DEP forces even when their center is further away from the pillars. Similarly, higher membrane capacitances due to higher ion densities, can increase the DEP force experienced by the cells. Thus, the E2 and Ful treated LCC1 cells' overall trapping efficiency increase corresponds to the cell size and surface feature increases. Similarly, the gradual decrease in the trapping efficiency in LCC9 cells following E2 and Ful treatments can also be related to the cell size and surface protrusion reductions.

Although it is possible to ascribe DEP differences between the LCC1 and LCC9 to changes in cell surface area and/or conductivity, the close genetic relationship between LCC1 and LCC9 provides a unique opportunity to examine the underlying gene expression changes underlying such changes in the plasma membrane and cell conductivity. For example, LCC9 showed a 4.1-fold relative increase in the mRNA expression of PALLD (Palladin) ($p < 4.4E-07$). Palladin is an actin associated protein that participates in reorganization of actin structures in breast cancer cells to form podosomes and invadopodia [48]. Palladin expression is associated with more aggressive, invasive breast cancer cell lines and overexpression of palladin in MCF-7 stimulated podosome formation [49]. As the formation of these structures will increase surface roughness and membrane surface area, palladin is a candidate molecule mediating these effects in LCC9 cells to modulate the cells' DEP properties through changes in plasma membrane capacitance. LCC9 cells

also exhibited more modest but highly significant relative decreased expression (2.8- fold) in ADAP1 ($p < 8.6$ E-08) mRNA. ADAP1 is involved with the formation of intercellular bridges through adherens junctions and desmosomes, structures which form linking the extracellular domains of cadherin family proteins to intracellular actin and intermediate filaments, respectively [50]. Loss of these junctional complexes is characteristic of the epithelial-mesenchymal transition which is accompanied by lamellipodia, filopodia, and invadopodia formation, loss of cell apical polarity, and alterations in cell surface proteins; thus, reductions in ADAP1 is another cellular pathway leading to increased cell membrane surface area and possibly, alterations in cell surface electrical charge and cell conductivity as well. Furthermore, LCC9 cells showed a 3.6-fold relative decrease in mRNA expression of the plasma membrane transport protein, SLC12A2 ($p<1.5$E-07). SLC12A2, known to play a role in ionic balance, cell volume and migration [51], has also been shown to be increased in aggressive form of lung adenocarcinoma [52]. The decreased expression of this plasma membrane transport protein could alter the DEP profile of LCC9 cells through both cell volume and cell conductivity changes. Finally, LCC9 cells showed a 13.9-fold relative decrease ($p <1.14$ E-07) in the expression of mRNA encoding a small plasma membrane glycoprotein, TM4SF1. TM4SF1 was first identified as the tumor cell antigen L6 [53]. Being membrane-associated as well as an electrically charged molecule, we suggest TM4SF1 might alter the DEP profile of LCC9 cells by altering the surface charge on the plasma membrane. Based on this gene analysis, we now have clues to the cellular proteins that modulate cell surface morphology, cell membrane charge, and cell size in LCC1 and LCC9 cells and thereby result in DEP profiles that distinguish a Ful-s (LCC1) breast cancer cell from a Ful-r (LCC9) breast cancer cell.

The presented method has shown that the πDEP platform can be utilized for the examination of cancer cell drug responsiveness. When compared with alternative techniques, such as standard proliferation and flow cytometry assays, which can be time consuming and highly laborious, this method is a rapid assay with minimal preparations steps [5]. Additionally, the drug response shifts indicated by the DEP profiles were supplemented with detailed analyses of the biophysical attributes to examine the potential causes for alterations in the cell's electrical properties. This is in contrast to similar studies which have utilized DEP for drug analysis. These studies have been limited in their analysis of biophysical shifts, as they have primarily focused on the cell membrane or cytoplasm as characteristics which contribute to DEP profile changes [6, 54, 55]. Here, we have examined the cellular proteins which could modulate the DEP profiles. Furthermore, we have shown that the πDEP platform can be used to examine the biophysical shifts of cells when exposed to drugs for various durations.

## 3.5 Conclusion

Ful-s (LCC1) and Ful-r (LCC9) derivatives of the MCF-7 cell line model of endocrine therapy sensitive and resistant human breast cancer varieties exhibit distinct DEP characteristics. The DEP analysis indicated Ful-r and Ful-s cells were distinguished by their f0 and trapping efficiencies. Based on the gene expression analysis the significantly differentially expressed mRNAs, PALLD, TM4SF1, ADAP1, and SLC12A2 were identified as candidates encoding proteins able to modulate the cell's DEP character.

## 3.6 References

[1] Pohl, H. A., *Journal of Applied Physics* 1951, *22*, 869-871.

[2] Zellner, P., Shake, T., Sahari, A., Behkam, B., Agah, M., *Anal Bioanal Chem* 2013, *405*, 6657-6666.

[3] Soltanian-Zadeh, S., Kikkeri, K., Shajahan-Haq, A. N., Strobl, J., Clarke, R., Agah, M., *ELECTROPHORESIS* 2017, *38*, 1988-1995.

[4] Gascoyne, P. R. C., Shim, S., Noshari, J., Becker, F. F., Stemke-Hale, K., *ELECTROPHORESIS* 2013, *34*, 1042-1050.

[5] Mulhall, H. J., Cardnell, A., Hoettges, K. F., Labeed, F. H., Hughes, M. P., *Integr Biol (Camb)* 2015, *7*, 1396-1401.

[6] Labeed, F. H., Coley, H. M., Thomas, H., Hughes, M. P., *Biophysical Journal* 2003, *85*, 2028-2034.

[7] Wang, L., Flanagan, L. A., Jeon, N. L., Monuki, E., Lee, A. P., *Lab on a Chip* 2007, *7*, 1114-1120.

[8] Flanagan, L. A., Lu, J., Wang, L., Marchenko, S. A., Jeon, N. L., Lee, A. P., Monuki, E. S., *STEM CELLS* 2008, *26*, 656-665.

[9] Gossett, D. R., Weaver, W. M., Mach, A. J., Hur, S. C., Tse, H. T. K., Lee, W., Amini, H., Di Carlo, D., *Analytical and bioanalytical chemistry* 2010, *397*, 3249-3267.

[10] Henslee, E. A., Torcal Serrano, R. M., Labeed, F. H., Jabr, R. I., Fry, C. H., Hughes, M. P., Hoettges, K. F., *Analyst* 2016, *141*, 6408-6415.

[11] Coley, H. M., Labeed, F. H., Thomas, H., Hughes, M. P., *Biochim Biophys Acta* 2007, *1770*, 601-608.

[12] Yu, Z., Guo, X., Jiang, Y., Teng, L., Luo, J., Wang, P., Liang, Y., Zhang, H., *Breast Cancer* 2017.

[13] Brufsky, A. M., *Cancer Treatment Reviews* 2017, *59*, 22-32.

[14] Sestak, I., *Breast Care* 2017, *12*, 146-151.

[15] Suman, V. J., Ellis, M. J., Ma, C. X., *Chinese clinical oncology* 2015, *4*, 34-34.

[16] Goncalves, R., DeSchryver, K., Ma, C., Tao, Y., Hoog, J., Cheang, M., Crouch, E., Dahiya, N., Sanati, S., Barnes, M., Sarian, L. O. Z., Olson, J., Allred, D. C., Ellis, M. J., *Breast Cancer Research and Treatment* 2017, *165*, 355-364.

[17] Brünner, N., Boysen, B., Jirus, S., Skaar, T. C., Holst-Hansen, C., Lippman, J., Frandsen, T., Spang-Thomsen, M., Fuqua, S. A. W., Clarke, R., *Cancer Research* 1997, *57*, 3486-3493.

[18] Gonzalez-Angulo, A. M., Morales-Vasquez, F., Hortobagyi, G. N., *Breast Cancer Chemosensitivity*, Springer 2007, pp. 1-22.

[19] Van Tine, B. A., Crowder, R. J., Ellis, M. J., *Cancer Discovery* 2011, *1*, 287-288.

[20] Jeselsohn, R., Buchwalter, G., De Angelis, C., Brown, M., Schiff, R., *Nat Rev Clin Oncol* 2015, *12*, 573-583.

[21] Nathan, M. R., Schmid, P., *Oncology and Therapy* 2017, *5*, 17-29.

[22] Dixon, J. M., *New Journal of Science* 2014, *2014*, 27.

[23] Brünner, N., Boulay, V., Fojo, A., Freter, C. E., Lippman, M. E., Clarke, R., *Cancer Research* 1993, *53*, 283-290.

[24] Kuske, B., Naughton, C., Moore, K., MacLeod, K. G., Miller, W. R., Clarke, R., Langdon, S. P., Cameron, D. A., *Endocrine-Related Cancer* 2006, *13*, 1121-1133.

[25] Ritchie, M. E., Phipson, B., Wu, D., Hu, Y., Law, C. W., Shi, W., Smyth, G. K., *Nucleic Acids Research* 2015, *43*, e47-e47.

[26] Clarke, R., Liu, M. C., Bouker, K. B., Gu, Z., Lee, R. Y., Zhu, Y., Skaar, T. C., Gomez, B., O'Brien, K., Wang, Y., Hilakivi-Clarke, L. A., *Oncogene* 2003, *22*, 7316-7339.

[27] Cook, K. L., Clarke, R., *Receptors & clinical investigation* 2014, *1*, e316.

[28] Piscuoglio, S., Ng, C. K. Y., Martelotto, L. G., Eberle, C. A., Cowell, C. F., Natrajan, R., Bidard, F.-C., De Mattos-Arruda, L., Wilkerson, P. M., Mariani, O., Vincent-Salomon, A., Weigelt, B., Reis-Filho, J. S., *Molecular Oncology* 2014, *8*, 1588-1602.

[29] Wright, P. K., May, F. E. B., Darby, S., Saif, R., Lennard, T. W. J., Westley, B. R., *International Journal of Clinical and Experimental Pathology* 2009, *2*, 463-475.

[30] Harrison, K., Hoad, G., Scott, P., Simpson, L., Horgan, G. W., Smyth, E., Heys, S. D., Haggarty, P., *Clinical Epigenetics* 2015, *7*, 92.

[31] Uhlen, M., Zhang, C., Lee, S., Sjöstedt, E., Fagerberg, L., Bidkhori, G., Benfeitas, R., Arif, M., Liu, Z., Edfors, F., Sanli, K., von Feilitzen, K., Oksvold, P., Lundberg, E., Hober, S., Nilsson, P., Mattsson, J., Schwenk, J. M., Brunnström, H., Glimelius, B., Sjöblom, T., Edqvist, P.-H., Djureinovic, D., Micke, P., Lindskog, C., Mardinoglu, A., Ponten, F., *Science* 2017, *357*.

[32] Huntley, R. P., Sawford, T., Mutowo-Meullenet, P., Shypitsyna, A., Bonilla, C., Martin, M. J., O'Donovan, C., *Nucleic Acids Research* 2015, *43*, D1057-D1063.

[33] Huang, S.-B., Wu, M.-H., Lin, Y.-H., Hsieh, C.-H., Yang, C.-L., Lin, H.-C., Tseng, C.-P., Lee, G.-B., *Lab on a Chip* 2013, *13*, 1371-1383.

[34] Vias, M., Massie, C. E., East, P., Scott, H., Warren, A., Zhou, Z., Nikitin, A. Y., Neal, D. E., Mills, I. G., *BMC Medical Genomics* 2008, *1*, 17.

[35] Roininen, N., Takala, S., Haapasaari, K.-M., Jukkola-Vuorinen, A., Mattson, J., Heikkilä, P., Karihtala, P., *BMC Cancer* 2017, *17*, 72.

[36] Weigelt, B., Geyer, F. C., Reis-Filho, J. S., *Molecular Oncology* 2010, *4*, 192-208.

[37] Gu, Z., Lee, R. Y., Skaar, T. C., Bouker, K. B., Welch, J. N., Lu, J., Liu, A., Zhu, Y., Davis, N., Leonessa, F., Brünner, N., Wang, Y., Clarke, R., *Cancer Research* 2002, *62*, 3428-3437.

[38] Klinge, C. M., Riggs, K. A., Wickramasinghe, N. S., Emberts, C. G., McConda, D. B., Barry, P. N., Magnusen, J. E., *Molecular and cellular endocrinology* 2010, *323*, 268-276.

[39] Huang, Y.-K., Fan, X.-G., Qiu, F., *International Journal of Molecular Sciences* 2016, *17*, 661.

[40] Zukauskas, A., Merley, A., Li, D., Ang, L.-H., Sciuto, T. E., Salman, S., Dvorak, A. M., Dvorak, H. F., Jaminet, S.-C. S., *Angiogenesis* 2011, *14*, 345-354.

[41] Liu, Y., Zhao, S., Song, M., Zhang, H., *Int J Clin Exp Med* 2017, *10*, 7734-7742.

[42] Allioli, N., Vincent, S., Vlaeminck-Guillem, V., Decaussin-Petrucci, M., Ragage, F., Ruffion, A., Samarut, J., *The Prostate* 2011, *71*, 1239-1250.

[43] Wang, X., Becker, F. F., Gascoyne, P. R., *Biochimica et Biophysica Acta* 2002, *1564*, 412-420.

[44] Krippl, P., Langsenlehner, U., Renner, W., Yazdani-Biuki, B., Köppel, H., Leithner, A., Wascher, T. C., Paulweber, B., Samonigg, H., *Clinical Cancer Research* 2004, *10*, 3518-3520.

[45] Pethig, R. R., *Dielectrophoresis: Theory, Methodology and Biological Applications*, John Wiley & Sons 2017.

[46] Pethig, R., Talary, M. S., *IET Nanobiotechnol* 2007, *1*, 2-9.

[47] Dopp, E., Jonas, L., Nebe, B., Budde, A., Knippel, E., *Environmental Health Perspectives* 2000, *108*, 153-158.

[48] Gilam, A., Conde, J., Weissglas-Volkov, D., Oliva, N., Friedman, E., Artzi, N., Shomron, N., *Nature communications* 2016, *7*, 12868.

[49] Goicoechea, S. M., Bednarski, B., García-Mata, R., Prentice-Dunn, H., Kim, H. J., Otey, C. A., *Oncogene* 2009, *28*, 587-598.

[50] Greene, B., Head, L., Gawad, N., Hamstra, S. J., McLean, L., *Journal of Otolaryngology - Head & Neck Surgery* 2015, *44*, 3.

[51] Damin, C., Wen, Z., John, S. K., Shaoshan, H., Dandan, S., *Current Medicinal Chemistry* 2015, *22*, 1171-1181.

[52] Sun, P.-L., Jin, Y., Park, S. Y., Kim, H., Park, E., Jheon, S., Kim, K., Lee, C.-T., Chung, J.-H., *QJM: An International Journal of Medicine* 2016, *109*, 237-244.

[53] Carter, P., Presta, L., Gorman, C. M., Ridgway, J. B., Henner, D., Wong, W. L., Rowland, A. M., Kotts, C., Carver, M. E., Shepard, H. M., *Proceedings of the National Academy of Sciences* 1992, *89*, 4285-4289.

[54] Kumar, R. T. K., Liu, S., Minna, J. D., Prasad, S., *Biochim Biophys Acta* 2016, *1860*, 1877-1883.

[55] Hoettges, K. F., Hubner, Y., Broche, L. M., Ogin, S. L., Kass, G. E. N., Hughes, M. P., *Analytical Chemistry* 2008, *80*, 2063-2068.

# 4 A Monolithic Dielectrophoresis Chip with Impedimetric Sensing for Assessment of Pathogen Viability

This chapter was reproduced from a manuscript under review in Journal of MicroElectroMechanical Systems (JMEMS).

## 4.1 Introduction

An estimated 7.1 million people suffer from some form of microbial infection, which results in nearly 12,000 annual deaths in the United States [2]. Thus, fast and cost-effective detection of microbial pathogens is imperative to ensure a safe and contamination-free water supply [3]. Over the past several decades, various techniques have been developed for the detection of numerous pathogens [3]. In particular, polymerase chain reaction (PCR) has emerged as the gold standard for highly specific detection of target bacteria in water. PCR is a nucleic acid amplification technology that is based on the isolation, amplification and quantification of a short DNA sequence known to be specific to the target. Although this technique requires less time than other techniques, such as culture based assays, PCR systems typically utilize laborious, and time consuming experimentation (typically several hours) and filtration techniques to achieve required sensitivity [1, 4]. Additionally, it can require external enrichment of samples prior to PCR analysis. Furthermore, PCR assays cannot directly confirm whether the DNA detected originated from a live or dead organism. As a result, alternative methods and technologies are necessary for rapid and low-cost bacteria detection.

Other popular methods have been based on culture and colony counting assays, sensors embedded with biological materials, enzyme-linked immunosorbent assays (ELISA), and gel electrophoresis [5-9]. Culturing via plate colony counting is a widely used technique due to well-established methods and ability to confirm that the targets are

viable. However, they are extremely time intensive, subject to contamination, and underestimate the number of bacteria in samples by ignoring potentially viable but non-culturable organisms. In contrast, other detection techniques such as biosensors and ELISA, incorporate biological materials such as antibodies, organelles, enzymes, or biomimic substances. These methods use the interaction of the biological material and pathogens to create a signal which is sensed through optical, electrochemical, thermometric, piezoelectric or magnetic transducers [10, 11]. Although there are a wide variety of these sensors, the majority of them remain highly labor intensive and time consuming. Additionally, several of these methods are limited in their detection resolutions which reduces the analysis reliability of low abundance samples without external enrichment steps.

Dielectrophoresis (DEP) has shown to be a promising tool for the selective concentration of microorganisms [12]. DEP is the motion of electrically-polarizable particles that are suspended in an electrolyte when subjected to a spatially non-uniform electric field [12]. DEP forces can be used to transport particles to either electric field gradient maxima or minima. Additionally, impedance detection has shown to consistently and inexpensively detect bacteria [1, 7, 8]. These detection methods utilize changes in impedance values to monitor bacteria levels. For growth-based impedance assays, a sample is monitored through the analysis of shifts in the electrical parameters of the growth media. The electrical conductivity of the growth media fluctuates due to active microbial metabolism, which results in impedance shifts [12, 13]. However, this method is based on the culturing of cells, making it a time consuming process. Alternatively, microfluidic devices have been used for the detection of pathogen cells directly using impedance

spectroscopy. These methods do not require cell culturing and can significantly reduce experimentation times. Li et al. showed that live and heat-killed bacteria can be detected through impedance spectroscopy. However, this method is limited in its detection limits due to a lack of initial enrichment of samples [14]. Thus, through the combination of these two techniques, several groups have been able to electrically-enrich and detect particles in various microfluidic assays [1, 7, 8, 11, 15, 16].

Conventional DEP platforms that are integrated with impedance spectroscopy typically rely on metallic electrodes which come in contact with the particle solutions [11]. The excitation of DEP electrodes induces an electric field which can be tuned to direct particles towards or away from the electrode surfaces, while additional electrodes are used for impedance sensing. Several groups have demonstrated great selectivity and throughput for these devices. Wang et al. showed that DEP enrichment and impedimetric detection of bacteria can reach detection limits as low as $5 \times 10^2$ colony-forming units/mL through the use of silver nanoparticles for signal enhancement [17]. Despite the improved signal quality, the required coating of bacterial surfaces with nanoparticles makes this a more laborious process. Moreover, this can affect the biophysical attributes of cells, making analysis of important parameters, such as viability, difficult. Furthermore, conventional DEP devices rely on the direct contact of bacterial cells with the electrodes, which results in several limitations, including electrode fouling and electrolysis inside the microchannel. Even groups such as Kim et al., which utilized a passivation layer over focusing electrodes, have limited use of electrodes due to lack of passivation of sensing electrodes [18].

Insulator-based DEP (iDEP) devices have also been integrated with impedance spectroscopy for the detection of pathogens. For these devices, insulating structures are

used to create unique geometries in the channel. Electric fields are distorted by these structures to generate the non-uniform gradients required for DEP. Sabounchi et al. demonstrated the application of iDEP features to enrich B. subtilis cells and electrically measure them through impedance analysis. Phase analysis shown that their device had a detection limit of 103 colony-forming units/mL [7]. Yet, the incorporation of a SiO2 layer over the electrodes caused the device to be limited in reuse. Issues such as one-time-use electrodes and the application of large voltages due to non-localized electric fields are common to many of these iDEP with impedance detection microfluidic devices [19].

Here, we present an alternative approach to conventional pathogen detection methods (i.e. PCR, iDEP with impedance detection) through a microfluidic chip which combines off-chip passivated insulator-based dielectrophoresis (OπDEP) and bioimpedance measurements for the selective detection of live/dead bacteria. Our unique OπDEP design generates localized capacitively coupled AC electric fields within the microchannel and uses negative or positive DEP to enrich the target species. The unique OπDEP design has no direct contact between electrodes and samples preventing common issues associated with electrode-based DEP as well as traditional insulator-based DEP techniques such as fouling, bubble formation, cross contamination and higher manufacturing costs.

In this study, we combine the capabilities of the OπDEP platform and high frequency impedance spectroscopy to perform live/dead assessment of bacteria. Staphylococcus epidermidis cells were initially trapped for enrichment and then selectively released for impedance sensing. Impedance results were analysed to estimate the proportions of live and dead bacteria in the samples. Flow cytometry measurements were

carried out in parallel to supplement and compare results produced by the OπDEP with integrated impedance sensing analysis. Thus, the monolithic chip reported here enables the creation of distributed sensor nodes at high risk points and continuous monitoring and characterization of bacteria in various water matrices.

## 4.2 Experimental Methods

### 4.2.1 Device Fabrication

Fabrication of the monolithic chip utilized a similar methodology to the previously reported πDEP fabrication process [16]. Figure 4.1 depicts the fabrication process for the two compartments of the chip: a disposable microfluidic component and a reusable transducer component. The disposable microfluidic component consists of an array of closely-spaced pillars to generate high-electric field gradients for DEP enrichment, as well as a narrow channel to focus the passage of enriched bacteria following their release. The polydimethylsiloxane (PDMS) disposable microfluidic component was formed through the use of an SU-8 silicon negative master wafer, shown in Figure 4.1.

To form the negative master wafer, SU-8 2025 photoresist was patterned on a <100> silicon wafer using photolithography. PDMS (Dow Corning, MI, USA) and curing agent was mixed in a 10:1 weight ratio and degassed to remove air bubbles. It was then poured over the silicon master and cured at 100°C for 40 minutes. The solidified PDMS was then peeled off, diced and punched at the inlets and outlets. The device was then plasma bonded to a 100 µm thick glass slide (Electron Microscopy Sciences, PA, USA) to passivate the electrodes from the microfluidic channel.

The reusable/detachable transducer component was fabricated on a separate glass substrate. Electrodes were patterned on the separate glass substrate by photolithography,

e-beam deposition of chrome/gold, and metal lift-off. The transducer component consists of an array of gold electrodes used for the excitation of DEP forces on bacteria around the pillars and for impedance sensing along the focusing channel.

The two components were placed on top of each other with minimal alignment and attached using tape. Figure 1 shows close-ups of the DEP and impedance sensing regions. The microchannel is 40 µm deep with two rows of insulating pillars (diameter: 100 µm; distance: 50). The focusing channel is 20 µm wide and 400 µm long. The electrode which surround the DEP and impedance electrodes are both spaced 1000 µm apart. The overall size of entire chip is 3 cm × 2.5 cm.

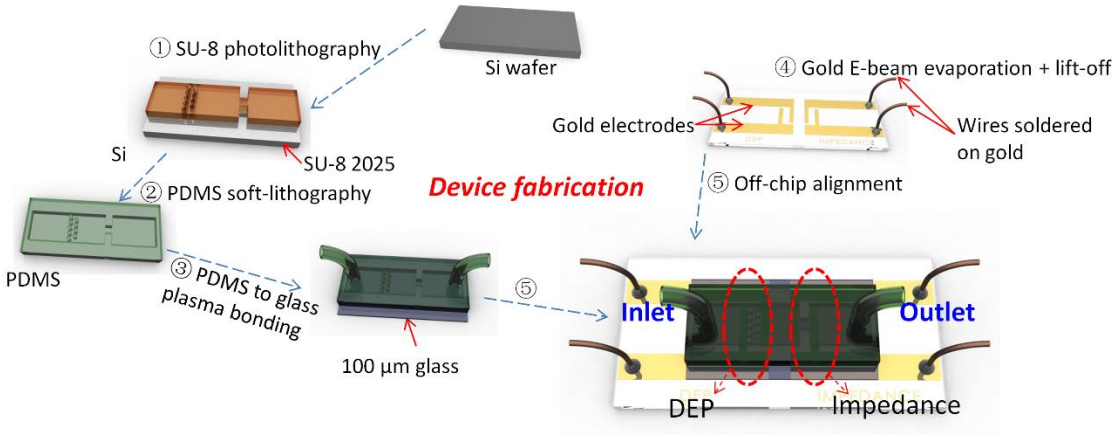


**Figure 4.1: .** ① Pattern SU-8 on a silicon wafer through photolithography; ② Pour liquid the Si master and cured at 100˚C for 40 min; ③ Remove cured PDMS from wafer and punch ports and bond to glass slide using oxygen plasma; ④ Deposit electrodes on separate glass slide through e-beam evaporation and lift-off; ⑤ Align and attach the two parts. Note that ③ is the disposable microfluidic component and ④ is the reusable transducer component of the monolithic chip.

### 4.2.2 Cell Preparation

Staphylococcus *epidermidis* strain (ATCC 14990) was cultured in brain heart infusion media (Bactrius Limited, Houston TX). *S. epidermidis* cells were cultured in 100 mL of broth medium at 37°C and 165 rpm to the exponential growth phase (OD600 ~ 0.8). Cells were then transferred into two sterile 50 mL centrifuge tubes, and subjected to two washes by centrifugation (5000 × g for 10 min) and re-suspension in 1× PBS. A calibration curve relating OD600 to microscopic cell counts was created and used to quantify the washed bacteria via spectrophotometry thereafter.

S. *epidermidis* was killed by heating the DI water or PBS suspended bacteria to 65°C for 15 minutes. Cells were then tagged with red/green fluorescence for 20 minutes using a Live/Dead viability kit (LIVE/DEAD Backlit, Invitrogen). S. *epidermidis* cells were then centrifuged and re-suspended five times in DI water to achieve a final measured conductivity of 850 µS/m. The DI water conductivity was measured with a conductivity meter (SG7, Mettler Toledo, Scherzenbach, Switzerland).

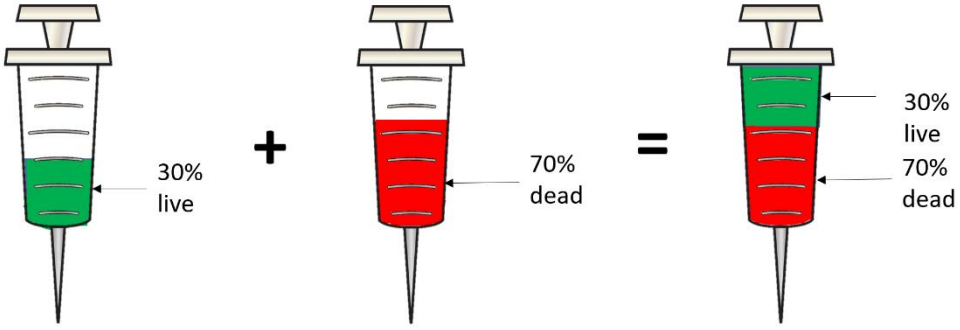


**Figure 4.2:** Example of live/dead solution mixtures. A 1 mL syringe was used such that a specific percentage was derived from a live bacteria solution with a concentration of $10^6$ cells/mL and any residue volume was derived from a dead bacteria solution with a concentration of $10^6$ cells/mL.

To analyse the sensitivity of the device, various ratios of live to dead bacteria concentrations were utilized. Starting from an approximate concentration of $10^6$ cells/mL in both live and dead pools, live/dead volume ratios of 1:0, 3:7, 1:1, 7:3, and 0:1. These ratios corresponded to the 0, 30%, 50%, 70%, and 100% live or dead mixtures. A visual depiction of this process is shown in Figure 4.2.

### 4.2.3 Principles of Microfluidic Device Operation

An overview of the device operation is shown in Figure 3. Prior to device operation, PDMS microfluidic devices were placed under vacuum for at least 30 minutes to reduce priming issues. Following vacuum exposure, the device was connected to a 1 mL syringe with a fluorescently tagged cell solution. The solution was pushed through the microfluidic channel at a constant flow rate of 50 µL/hr by a Pump11 Elite syringe pump (Harvard Apparatus, MA, USA). The electrodes which surround the DEP region were connected to a 50 MHz function generator (B&K Precision, CA, USA) and a voltage amplifier (FLC Electronics AB, Sweden) to initiate cell enrichment.

For initial enrichment, both live and dead bacteria were subjected to DEP forces induced by the application of the AC electric field causing them to "trapping" around the insulating pillars, as seen in Figure 4.3 (Voltage **ON**).

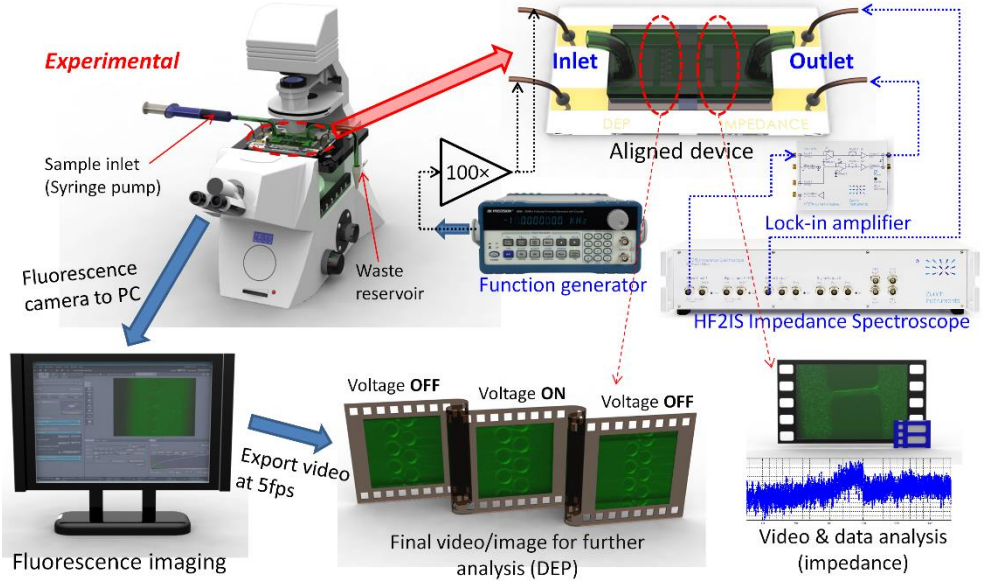


**Figure 4.3:** Schematic of the operation of the device including experimental setup and images of DEP trapping/release and impedance measurements.

The DEP force experienced by the bacteria can be modelled as the force on a lossy dielectric spherical particle suspended in a medium, as shown below:

$$\mathbf{F}_{DEP} = 2\pi R^3 \varepsilon_m Re\left[ f_{CM} \right] \nabla \left|\mathbf{E}\right|^2 \tag{4.1}$$

where $R$ is the radius of the particle, $\varepsilon_m$ is the permittivity of the medium, E is the local electric field. $Re\left[ f_{CM} \right]$ is the real part of the Clausius-Mossotti (CM) factor which for a lossy dielectric sphere is:

$$f_{CM} = \left(\varepsilon_p^* - \varepsilon_m^*\right) / \left(\varepsilon_p^* + 2\varepsilon_m^*\right) \tag{4.2}$$

where $\varepsilon_p^*$ and $\varepsilon_m^*$ are the complex permittivities of the particle and the medium, respectively. A thorough modelling and analysis of DEP was presented by Wang, et.al. in 1997 [17]. From Equation 4.2, we can observe that the dielectric properties of the particle in

comparison to the medium greatly impacts the movement of the particle under the DEP forces. When the particle permittivity is greater than the medium it is suspended in, the CM factor becomes positive translating to a positive DEP (pDEP) force which propels particles towards the areas of high electric field gradients. Conversely, when the particle permittivity is smaller than the medium it is suspended in, the CM factor becomes negative translating to a negative DEP (nDEP) force which propels particles towards the areas of low electric field gradients. This device capitalizes on pDEP forces to enrich both live and dead bacteria around the insulating pillars.

In addition to the DEP force, particle trajectory is also influenced by the frictional force term due to hydrodynamic drag as expressed by Stoke's equation:

$$\boldsymbol{f = 6r\pi\eta v} \tag{4.3}$$

where $\boldsymbol{v}$ is the flow velocity relative to the particle [18]. In order to observe DEP trapping around the insulating pillars, the DEP force must overcome the hydrodynamic drag induced by the bulk fluid flow. Additional hydrodynamic forces such as buoyancy can be considered negligible due to the low Reynolds numbers and relatively low flow rates used for the experiments.

To determine suitable operation parameters for selective enrichment and release of live and dead particle, the electric field magnitude and frequency were tuned based on optimization DEP experiments. The frequencies used in the optimization experiments were 1 kHz, 10 kHz, 50 kHz, 100 kHz, 200 kHz, 300 kHz, 400 kHz, 500 kHz, 600 kHz, 700 kHz, 800 kHz, 900 kHz, and 1 MHz. Various voltages were applied over this frequency. Trapping of the cells was observed using a Zeiss Axio Observer. Z1 inverted epifluorescence microscope (Germany) with a 10× objective lens and imaged using a Zeiss

AxioCam MRc camera (Germany). Trapping efficiencies were calculated as the ratio of trapped cells to the total number of cells in each run.

Following DEP enrichment, cells were selectively released by turning off the signal, as shown in Figure 4.3 (Voltage **OFF**). Additionally, to prevent the detection of non-enriched samples, the electric field signal was immediately turned back on following the signal removal. This ensured that only the selectively enriched samples were measured. Enriched bacteria were then sensed in the narrow detection region near the outlet through impedance spectroscopy. Based on single shell models of cells as defined by [12], the impedance of each bacteria cell could be modelled as an equivalent electrical circuit with various resistors and capacitors used to represent different components of the cell. However, because cells were enriched prior to electrical sensing, recorded impedance values could be modelled as the summation of each individual cell. Thus, the recorded values were population level measurements rather than measured at single cell level.

### 4.2.4 Flow Cytometry

Validation experiments were carried out via flow cytometry using a BD Accuri$^{TM}$ C6 Flow Cytometer (BD Biosciences), according to a protocol previously developed by the Swiss Federal Institute of Aquatic Science and Technology (Eawag, Switzerland; Reference). The method consists of introduction of two nucleic acid-binding stains to the bacterial suspension: SYBR® Green I (SG), a DNA-binding dye that can penetrate the membrane of intact undamaged cells as well as that of damaged cells; and Propydium Iodide (PI), a large and positively charge DNA and RNA-binding dye that can only penetrate damaged cell membranes but is excluded from cells with intact membranes.

When co-stained, cells with damaged membranes can be differentiated from intact cells via a multi-parametric flow cytometry analysis.

Briefly, aliquots of *S. epidermidis* (between $10^5$ and $10^6$ cells/mL in 1× PBS) were treated at 65°C for 15 minutes to promote cell damage, and mixed at a series of ratios with undamaged cells in 500 μL volumes. The conditions tested contained 0, 30, 50, 70, and 100% of damaged bacteria with respect to the undamaged counterpart. Bacterial staining consisted of an initial pre-warming step at 37°C for 3 minutes, followed by addition of 5 μL of either stain (SG, 1× final concentration; PI, 6 μM final concentration; or SG+PI, 1× + 6 μM final concentration), and incubation in the dark at 37°C for 15 minutes. 1× PBS blanks and unstained control samples were also included in each experiment. Detection of SY and PI is enabled by FL1 and FL3 detectors in the BD Accuri™ C6 Flow Cytometer and plotted on a 2-dimensional, log-scale FL1-A vs FL3-A density plot [24].

## 4.3 Results and Discussion

### 4.3.1 Dielectrophoretic Profiles

Dielectrophoretic profiles were determined for both the live and dead bacteria separately with the OπDEP platform. Operational parameters for the AC signal were optimized by sweeping the voltage and frequency of the electric field as shown in Figure 4.4. It was found that at 150 Vpp the onset of trapping was 50 kHz for the live bacteria and 200 kHz for the dead bacteria. It was also observed that at 300 Vpp 400 kHz had trapping efficiency close to 100% for live bacteria, while the dead bacteria had a peak trapping efficiency of 75% at 500 kHz (Figure 4.4A). Additional experiments were conducted at 250 Vpp (Figure 4.4B). At this magnitude, it was found that the onsets for the live and dead bacteria remained 50 kHz and 200 kHz, respectively, but that the trapping efficiencies

increased. The live bacteria had trapping efficiencies above 80% for 50 kHz-500 kHz and close to 100% trapping at 300 kHz and 400 kHz. Similarly, the dead bacteria had trapping efficiencies higher than 70% for 200-500 kHz with a maximum trapping efficiency of 90% at 400 kHz.

Variations in the trapping efficiency values are due to the balance of the DEP force and the Stoke's drag. Thus, the larger the electric field magnitude (applied voltage) resulted in higher trapping efficiencies and lower onset frequencies for pDEP. Furthermore, the distinctive onset frequencies for the live/dead cells are also a function of the DEP force and Stoke's drag, where the initial trapping is when the DEP force dominates. However, the differences in the onset frequencies between the live and dead bacteria is due to the differences in the cell morphology and electrical properties. As indicated by Equation 4.3, the DEP force is directly related to complex permittivities of the cells. Previously reported analyses of live/dead bacteria have indicated that live bacteria tend to have larger membrane conductivities than that of dead bacteria. The reduced conductivities translate to smaller complex permittivites which results in the decrease of the DEP force, as well as an increase in the onset pDEP frequency.

It was found that the operation parameter of 250 Vpp was optimal for selectively trapping only the live bacteria cells at 100 kHz and trapping both live and dead bacteria at 200 kHz or higher. This promising result would allow for the measurement of the live and dead bacteria through impedance measurements.

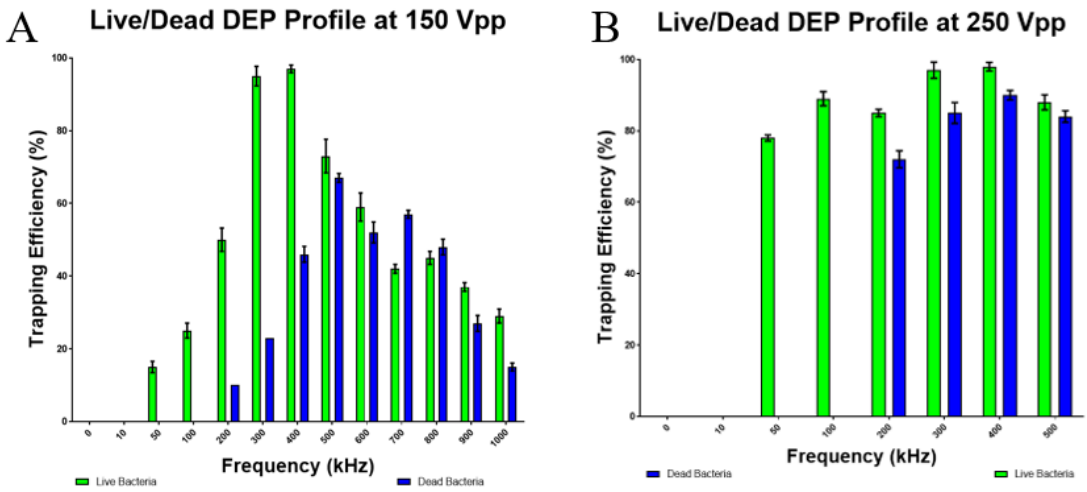


**Figure 4.4:** DEP profiles for optimization experiments. A) is for 150Vpp and B) is for 250Vpp for the electric field magnitudes. The frequencies were varied based on maximum range of equipment.

### 4.3.2 Impedance Spectroscopy Measurements

Impedance measurements for the live/dead samples were taken by first exciting the DEP region at 250 Vpp and 400 kHz to trap both the live and dead bacteria. The frequency was then dropped to 100 kHz to release the dead bacteria, while maintaining the live cells around the pillar. The electric field was then removed so as to release the live bacteria cells.

The 250 Vpp and 400 kHz electric field was then turned so that only the enriched sample would be measured.

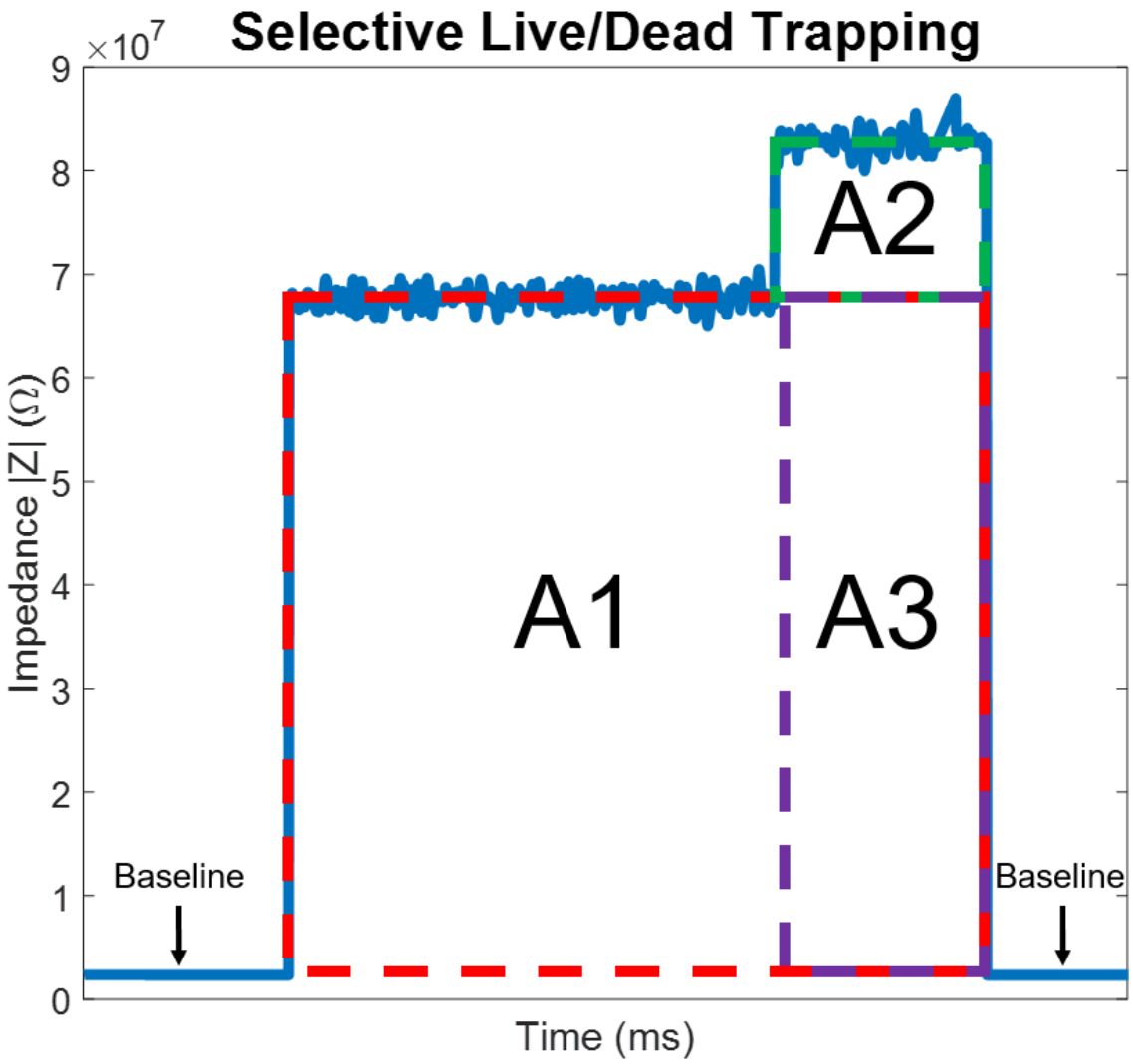


**Figure 4.5:** Raw impedance measurement where A1 is the corresponding dead bacteria and A2 is the corresponding live bacteria.

Sensitivity of the device was determined by varying the S. *epidermidis* live to dead ratio. Enrichment time was varied as 60, 180, 300, 480 and 600 seconds. Figure 4.5 displays an example of the impedance measurement to demonstrate the bioimpedance as the electric field was varied. The solution concentration was constant at $10^6$ cells/mL with a live/dead

ratio of 3:7. The baseline impedance was 3.0 x$10^4$ Ω. This value was a combination of noise and the impedance value of the DI medium. Following frequency shift of the electric field from 400 kHz to 100kHz, the release of the dead bacteria cells generated a step increase in the impedance output. Once the electric field was removed there was another step increase in the impedance output which corresponded to the combination of the enriched live and free flowing dead bacteria. To analyse the raw data, a filtering algorithm was utilized to smooth the curve. The line and dead bacteria was calculated as A2 and A3 respectively in Figure 4.5. The number of bacteria cells passing through the channel was confirmed with videos of DEP and BIS region during chip operation.

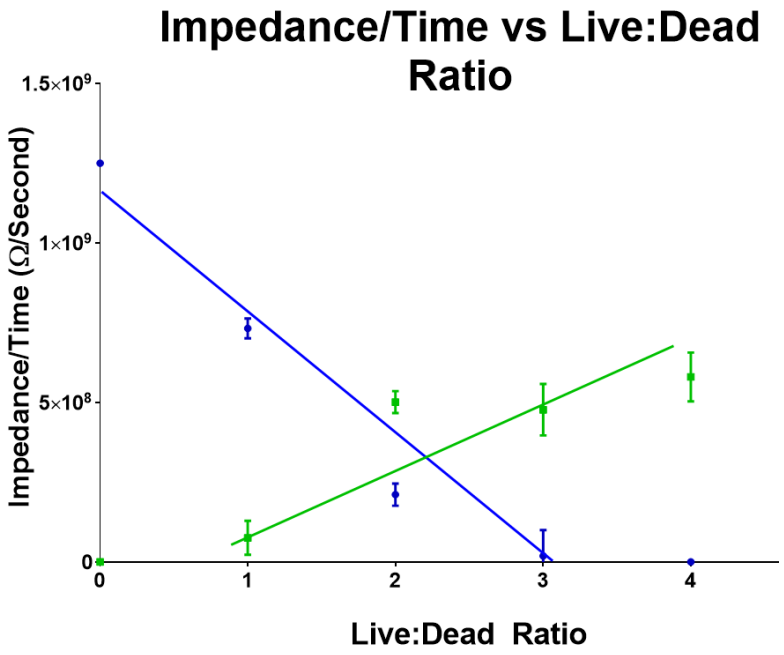


**Figure 4.6:** Impedance/Time for varying ratios, where 0 is 1:0, 1 is 7:3, 2 is 1:1, 3 is 3:7, and 4 is 0:1 live: dead respectively. Blue is live cells and Green is dead cells.

The area under the step increase for each ratio when enriched for 300s was plotted on Figure 4.6. It can be seen that unique impedance per second values were obtained for

each ratio for both the live and dead cells. Thus, it was observed that for higher amounts of live cells, there were larger step increases for longer durations in A2. Similarly, higher amounts of dead bacteria, resulted in larger step increases in A1 and A3. The best fit line was also plotted on Figure 4.6 and found to have an R-squared value of 0.9483. This shows there is a linear trend between the ratio of live/dead and the output impedance measurement. The linear tread also enables us to not only detect these microbes in the solution but also the amount of live/dead bacteria based on the step increase. It should be noted that the theoretical 100% live sample had some increase in the peak for A1. This indicated that were some cells which could be identified as dead.

A similar trend was found when the live/dead ration was constant at 1:1 and the enrichment time was varied. Figure 4.7 depicts the area under the step increase as a function of the enrichment times. As the enrichment time increases, so does the step increase area. It was found that the relationship for these parameters was exponential in nature. Although not a linear relationship, it was that we were still able to determine the amount of live/dead bacteria based on the impedance measurements.

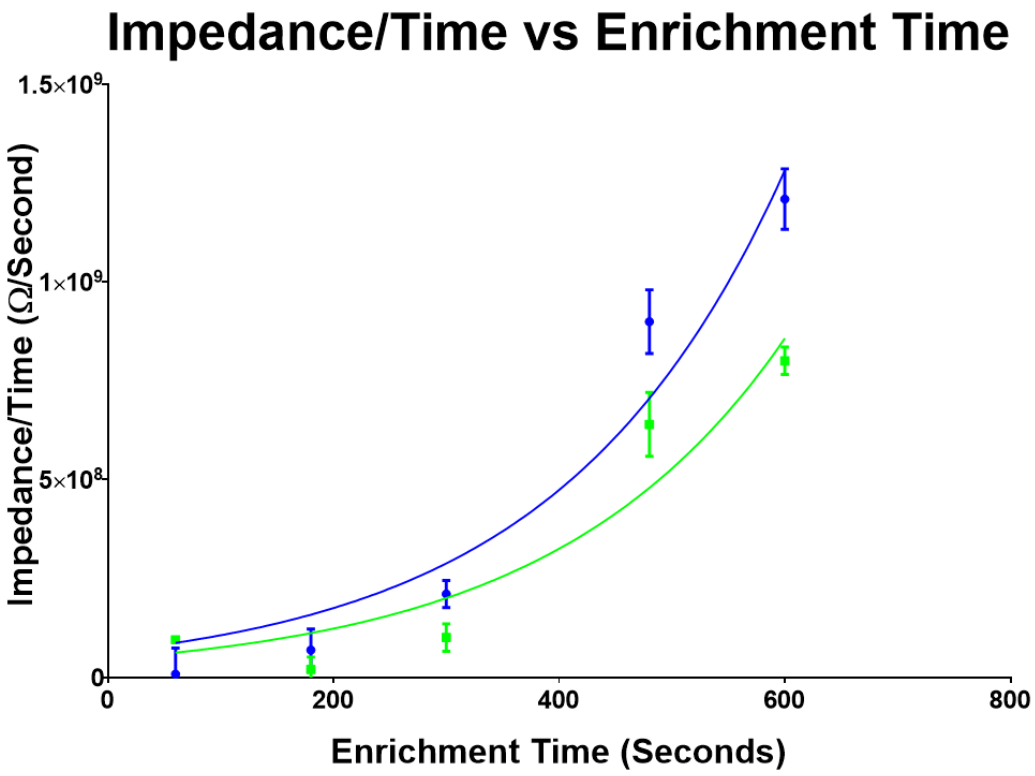


**Figure 4.7:** Impedance/Time for varying enrichment times while at a constant live: dead ratio of 1:1. Blue is dead cells and Green is live cells.

A similar trend was found when the live/dead ration was constant at 1:1 and the enrichment time was varied. Figure 4.7 depicts the area under the step increase as a function of the enrichment times. As the enrichment time increases, so does the step increase area. It was found that the relationship for these parameters was exponential in nature. Although not a linear relationship, it was that we were still able to determine the amount of live/dead bacteria based on the impedance measurements

### 4.3.3 Flow Cytometry

Flow cytometry assays were run in parallel to DEP with impedance measurements to compare the two methods. Figure 4.8 depicts summarizes the result of the flow

cytometry. To estimate identify the percentage of live vs dead cells in the samples, boundaries were drawn to indicate specific conditions which could be used to determine cell status. The boundaries were drawn around the live and dead clusters that resulted from the flow cytometric analysis of samples containing either 100% live or 100% dead cells, respectively (Figure 4.8). Although the boundaries were drawn to exclusively contain the desired clusters, the presence of an intermediate or transition state between the live and dead clusters was observed and was partially excluded from both of the clusters. The resulting live and dead groupings are shown as the red dotted lines in Figure 4.8, where P1 are live cells and P2 are dead cells.

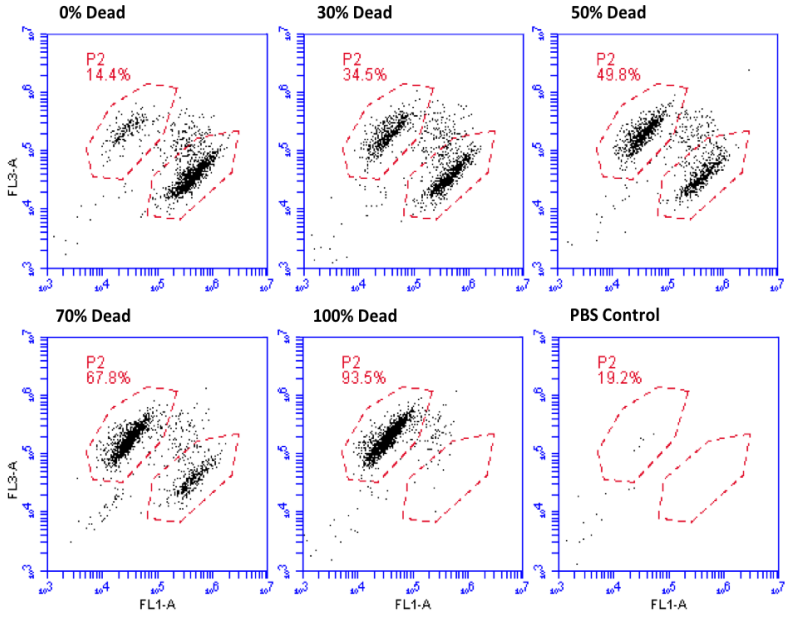


**Figure 4.8:** Live/Dead ratio comparisons between DEP enrichment and impedance detection and flow cytometry.

It was observed that some percentage of cells were dead even in the 100% live solution. This is due to minimal amounts of bacteria which could have died either during

the preparation process or while they were suspended in the PBS. It was found that overall the ratios of live/dead cells were similar to the theoretical ratios.

### 4.3.4 Comparison

Live/dead ratios were derived from the DEP and impedance measurement and flow cytometry assays. The results from these experiments were compared as indicated in Figure 4.9. From these graphs, it can be observed that the majority of live cell concentrations detected using DEP and impedance measurements were higher than flow cytometry measurements. This can be the result of the residual dead bacteria which was not released when the electric field frequency was lowered. This may be a result of attachment to surrounding live cells or to the PDMS insulating posts.

Additionally, it can be observed that for the live/dead ratios of 3:7, 1:1, 7:3, and 0:1, combined DEP and impedance measurements produced closer results to the theoretical ratios than flow cytometry for live cell concentrations. In contrast, flow cytometry and DEP with impedance measurements produced similar results for the dead bacteria concentrations.

The results presented here indicates that the OπDEP platform holds promise as a tool for live/dead pathogen assessments. This is a significant improvement over similar DEP and impedance measurement devices. Techniques such as dieletrophoretic impedance measurement (DEPIM) have shown detection limits of between $10^4$ to $10^3$ colony-forming units/mL [25]. However, these methods have noted that conductance measurements slowly increase even for control suspensions containing no pathogens due to issues with pre-filtering. As a result, these assays can be unreliable for low abundance populations [25]. In contrast, our monolithic platform has demonstrated sensitivities as low as 100s of

bacteria/mL [1]. Techniques which have combined the DEPIM and electropermabilization have shown improved detection limits to similar ranges [25]. However, the electropermabilization technique relies on the transport of ions through perforated cell membranes [25]. This causes a transient increase in the membrane permeability. Although detection sensitivity is improved through this process, the electropermabilization modifies the intrinsic electrical properties of these cells, which makes analysis of cell more challenging or unclear. The method presented in this paper relies solely on the DEP force and impedance analysis, both techniques of which do not affect the intrinsic electrical properties of cells.

Suehiro et al. have tested the detection of viable versus nonviable through dielectrophoretic enrichment and impedance measurements [19, 26]. Although they were able to demonstrate significant DEP and impedance differences between viable and heat sterilized nonviable pathogens, their method was very limited in the differentiation of the two population when mixed. In fact, when viable cell and heat sterilized nonviable cell mixtures were tested, conductance values were nearly in agreement with those of pure viable cells [19, 26].

In contrast, our platform has demonstrated the detection of live/dead bacteria through the selective release of cells and impedance analysis. This has applications for cytotoxicity investigations where pathogens can be pre-treated with various chemical stimuli and analyzed through the described methodology. Additionally, because DEP is the governing force for selective enrichment and release, the platform can be further calibrated to enable the drug sensitivity analysis. Moreover, the real-time detection can be further calibrated to eliminate the need for fluorescence tagging making this an all electrical, label-

free system.

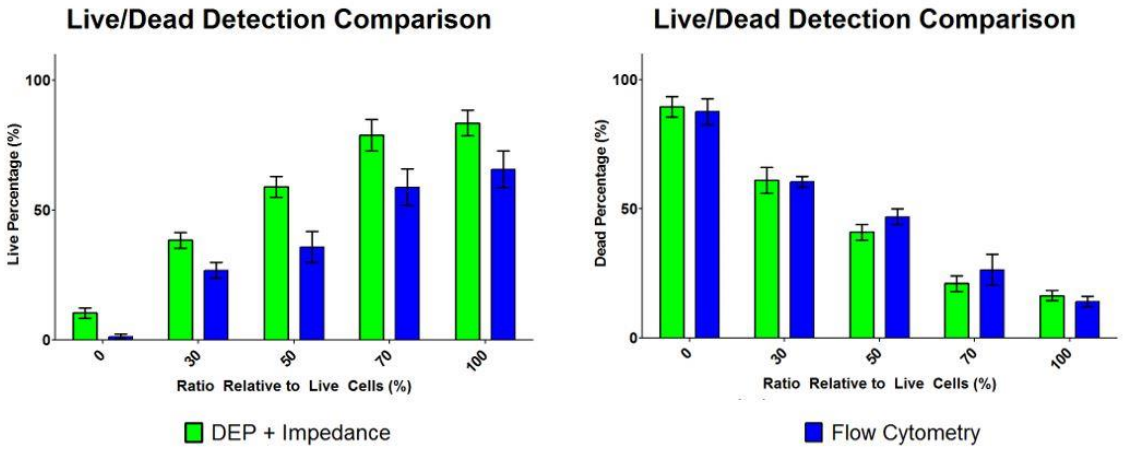


**Figure 4.9:** Live/Dead ratio comparisons between DEP enrichment and impedance detection and flow cytometry.

This indicates that the OπDEP platform can be used for as a tool for live/dead pathogen assessments. This has application for cytotoxicity investigations where pathogens can be pre-treated with various chemical stimuli and analysed through the described methodology. Additional, because DEP is the governing force for selective enrichment and release, the platform can be further calibrated to enable drug sensitivity analysis. Moreover, the real-time detection can be further calibrated to eliminate the need for fluorescence tagging, making this an all electrical, label-free system.

## 4.4 Conclusion

We developed a monolithic DEP chip with integrated impedance spectroscopy capabilities. It was found that that live/dead cells could be enriched and selectively released for downstream electrical sensing. An algorithm was used to analyse recorded impedance data to determine approximate cell concentrations. These results were compared to those obtained by flow cytometry as a bench-mark, indicating that the OπDEP platform with

integrated impedance measurements can be used as a rapid assay for live/dead pathogen detection. Further calibration and investigation of this technique can enable the use of the OπDEP platform for viability or cytotoxicity assays.

## 4.5 High-throughput Microfluidics Assay

### 4.5.1 Introduction

The development of a low-cost, disposable, high-throughput microfluidic assay integrating bacteria enrichment using DEP and capacitively-coupled impedance sensing is demonstrated for the evaluation of the inherent electrical properties of cells. This assay incorporates an array of microfluidic channels which combine into a single impedance sensing chamber. Using this unique design, *Staphylococcus epidermidis* was selectively enriched through DEP forces induced by AC electric field excitation. The concentrated sample was then released into the impedance sensing region and measured, resulting in rapid measurements through a high-throughput assay. This paper reports the design and fabrication of a high throughput microfluidic device for dielectrophoretic trapping and electrical characterization of biological cells, featuring at least one order of magnitude increase in the flow rate (1mL/hr or ~17μL/hr) compared to the current state-of-the-art methods [1, 14, 16, 17]. The chip features OπDEP for selectively trapping bioparticles, and utilizes a focusing region followed by impedance spectroscopy for detection of concentrated samples at the center of the device. This enhances the sensitivity of the chip, making it the highest throughout iDEP-based chip.

### 4.5.2 Methodology

Structural SU-8 photoresist is used to create a silicon master mold using conventional photolithography techniques [20] as depicted in Figure 4.10. The PDMS microfluidic assay

is fabricated using soft lithography, and plasma bonded to a glass cover slide. Chrome/gold electrodes are deposited onto a separate Pyrex wafer. The biochip assay is then aligned and taped to the electrode substrate to form the assembly shown in Figure 11A. This allows the reuse of the electrodes and reduction of the cost of each chip to less than $2 per experiment. The chip features twenty parallel channels containing insulating pillars as shown in Figure 11B. A sample of Staphylococcus epidermidis is injected into the chip using a syringe pump. A function generator is used to induce an AC electric field across the assay to enrich the sample for 60 second periods, with 10, 20, and 30 second rests in between. Trapping is observed using an inverted fluorescence microscope. An impedance analyzer is used to take measurements at the center of the device, shown in Figure 11C, following cell enrichment and release.

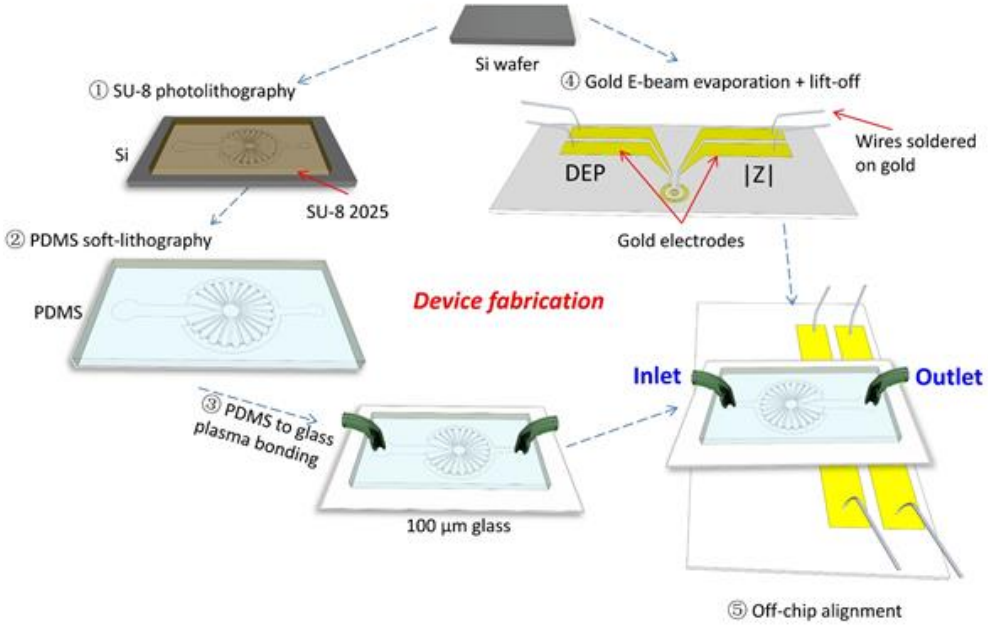


**Figure 4.10:** Overview of device fabrication process.

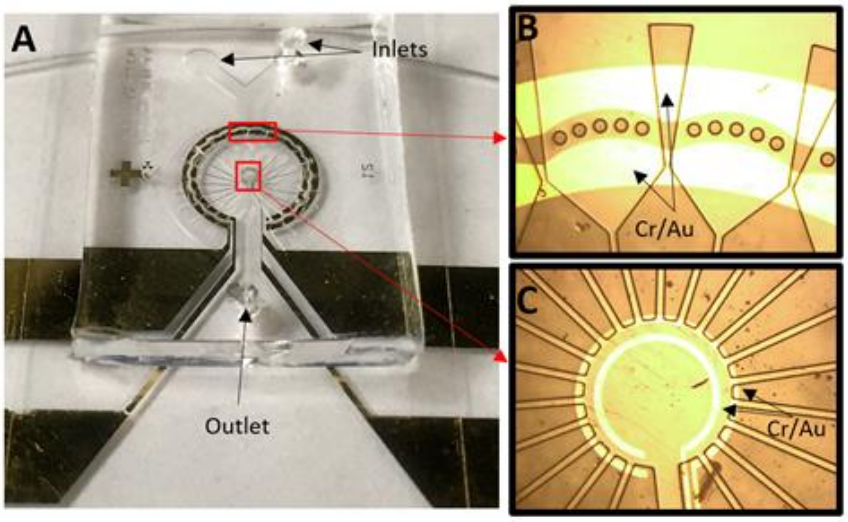


**Figure 4.11:** Optical images of biochip, which has a circular design to minimize the area and enhance the uniformity of electric field distribution across parallel regions. (A) Top view of assembled chip. Close up of (B) DEP trapping region featuring insulated pillars 100μm in diameter and (C) impedance detection region.

### 4.5.3 Results and Discussion

Figures 12A-C illustrate the trapping of the bacteria within the device. We tested the chip at a high flow rate of 1mL/hr and at a voltage of 200 Vpp with a range of frequencies from 0 to 1 MHz. The DEP trapping efficiency was calculated for selected frequencies, as shown in Figure 12A. The chip yielded close to 100% trapping efficiency for frequencies above 50 kHz at a high flow rate. The results clearly show that the proposed biochip has the potential to achieve even higher throughputs. Impedance measurement was also sensitive to the released bacteria passing through the center of the chip as shown in Figure 13. The chip design presented here is a significant improvement over recent work presented at the MEMS 2016 conference, in which flow rates close to only 100 μL/hr were achieved [1]. Further experiments are being conducted to determine the maximum flow rate and

sensitivity that can be achieved for bacteria detection, enabling the chip for use as a standalone platform for real-time water monitoring applications.

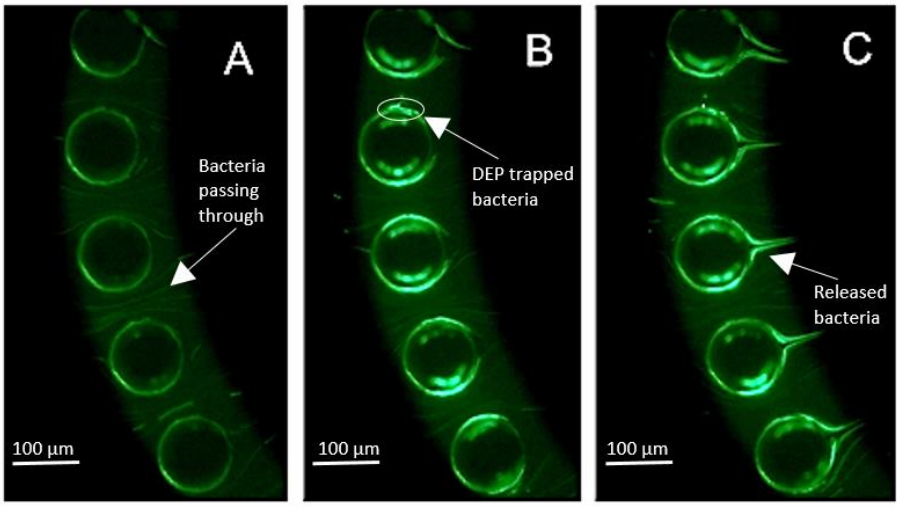


**Figure 4.12:** Detailed view of DEP trapping region (A) before, (B) during, and (C) after release of S. epidermidis bacteria.

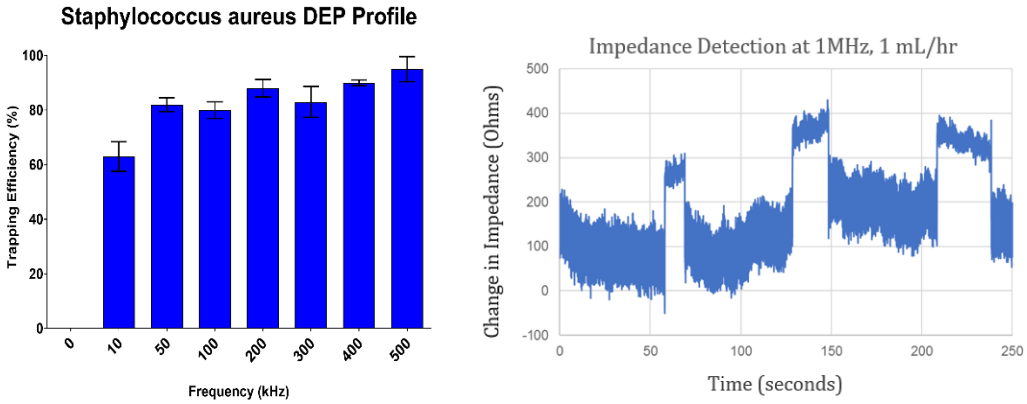


**Figure 4.13:** Estimated trapping efficiencies plotted for selected frequencies. Impedance measured at the center of the device following enrichment of S. epidermidis cells at a voltage of 200 $V_{pp}$ with a frequency of 1 MHz.

## 4.6 References

[1] Kikkeri, K., Agah, M., *2017 IEEE 30th International Conference on Micro Electro Mechanical Systems (MEMS)* 2017, pp. 358-361.

[2] Organization, W. H., 2014.

[3] Grabow, W., *Water S. A.* 1996, *22*, 193-202.

[4] Wassenberg, M., Kluytmans, J. A., Box, A., Bosboom, R., Buiting, A., Van Elzakker, E., Melchers, W., Van Rijen, M., Thijsen, S., Troelstra, A., *Clinical Microbiology and Infection* 2010, *16*, 1754-1761.

[5] Yang, L., Li, Y., Griffis, C. L., Johnson, M. G., *Biosensors and bioelectronics* 2004, *19*, 1139-1147.

[6] Gawad, S., Cheung, K., Seger, U., Bertsch, A., Renaud, P., *Lab on a Chip* 2004, *4*, 241-251.

[7] Sabounchi, P., Morales, A. M., Ponce, P., Lee, L. P., Simmons, B. A., Davalos, R. V., *Biomedical Microdevices* 2008, *10*, 661.

[8] del Moral-Zamora, B., Punter-Villagrassa, J., Oliva-Brañas, A. M., Álvarez-Azpeitia, J. M., Colomer-Farrarons, J., Samitier, J., Homs-Corbera, A., Miribel-Català, P. L., *Electrophoresis* 2015, *36*, 1130-1141.

[9] Kant, K., Shahbazi, M.-A., Dave, V. P., Ngo, T. A., Chidambara, V. A., Linh, Q. T., Bang, D. D., Wolff, A., *Biotechnology advances* 2018.

[10] Foudeh, A. M., Didar, T. F., Veres, T., Tabrizian, M., *Lab on a Chip* 2012, *12*, 3249-3266.

[11] Lazcka, O., Del Campo, F. J., Munoz, F. X., *Biosensors and bioelectronics* 2007, *22*, 1205-1217.

[12] Pethig, R. R., *Dielectrophoresis: Theory, Methodology and Biological Applications*, John Wiley & Sons 2017.

[13] Li, M., Li, W. H., Zhang, J., Alici, G., Wen, W., *Journal of Physics D: Applied Physics* 2014, *47*, 063001.

[14] Li, H., Multari, C., Palego, C., Ma, X., Du, X., Ning, Y., Buceta, J., Hwang, J. C. M., Cheng, X., *Sensors and Actuators B: Chemical* 2018, *255*, 1614-1622.

[15] Hoettges, K. F., Dale, J. W., Hughes, M. P., *Phys Med Biol* 2007, *52*, 6001-6009.

[16] Lopez-Barbosa, N., Campaña, A. L., Noguera, M. J., Florez, S. L., Aroca, M. A., Cruz, J. C., Osma, J. F., *Biosensing Technologies for the Detection of Pathogens-A Prospective Way for Rapid Analysis*, InTech 2018.

[17] Wang, R., Xu, Y., Sors, T., Irudayaraj, J., Ren, W., Wang, R., *Microchimica Acta* 2018, *185*, 184.

[18] Páez-Avilés, C., Juanola-Feliu, E., Punter-Villagrasa, J., del Moral Zamora, B., Homs-Corbera, A., Colomer-Farrarons, J., Miribel-Català, P. L., Samitier, J., *Sensors* 2016, *16*, 1514.

[19] Hamada, R., Takayama, H., Shonishi, Y., Mao, L., Nakano, M., Suehiro, J., *Sensors and Actuators B: Chemical* 2013, *181*, 439-445.

[20] Nakidde, D., Zellner, P., Alemi, M. M., Shake, T., Hosseini, Y., Riquelme, M. V., Pruden, A., Agah, M., *Biomicrofluidics* 2015, *9*, 014125.

[21] Wang, X. J., Wang, X., Gascoyne, P., *Journal of Electrostatics* 1997, *39*, 277-295.

[22] Castellanos, A., Ramos, A., Gonzalez, A., Green, N. G., Morgan, H., *Journal of Physics D: Applied Physics* 2003, *36*, 2584.

[23] Berney, M., Hammes, F., Bosshard, F., Weilenmann, H.-U., Egli, T., *Applied and environmental microbiology* 2007, *73*, 3283-3290.

[24] Gatza, E., Hammes, F., Prest, E., *White paper*. *BD Biosciences* 2013.

[25] Suehiro, J., Shutou, M., Hatano, T., Hara, M., *Sensors and Actuators B: Chemical* 2003, *96*, 144-151.

[26] Suehiro, J., Hamada, R., Noutomi, D., Shutou, M., Hara, M., *Journal of Electrostatics* 2003, *57*, 157-168.

# 5 Low-Cost Rapid Dielectrophoretic Separation of Heterogeneous Cell Mixtures

This chapter was reproduced from a manuscript under review in Nature Microsystems and Nanoengineering.

## 5.1 Introduction

Purification of heterogeneous mixtures through separation techniques is imperative for numerous analytical applications [1-4]. Separation and sorting of biological particles including cells is vital as a preparative step to enable the meticulous analysis of purified samples. Isolation of heterogeneous cell populations into more distinct homogenous subpopulations will enable further molecular, chemical, or biophysical characterization of the cellular activities. Such detailed analysis can be further utilized for the monitoring of diseases in patients or detecting harmful pathogen activities in the environment [5-8]. Specifically, potentially high risk bioparticles such as nonviable cells, cancerous cells, disease-infected cells or bacterial cells can be separated from surrounding (non-target) particles and be evaluated.

Numerous assays have been developed for the separation and sorting of micron-scale particles [1-3, 9]. These techniques can be characterized as passive or active methods or combinations of the two. Methods such as inertial microfluidics and dean flow fractionation are passive techniques that rely on the superposition of shear-gradient-induced lift and wall-effect induced lift forces to induce differential particle velocities based on particle size [1, 10]. Another passive separation technique which extends this concept is deterministic lateral displacement. This method uses asymmetric bifurcations of laminar flows through an array of unique structures in the microchannels. Heterogeneous

samples in these devices are separated as particle paths are deterministic which are dependent on their size and deformability [1]. Although several groups [10, 11] have shown the sorting of various microparticles through these passive techniques, the reliance on particle size limits the capabilities of these system to separate similarly sized populations or provide additional information on the separated cells.

Active methods such as fluorescence-activated cells sorting (FACS) and magnetic-activated cell separation (MACS) have shown to effectively separate particles based on either fluorescence or magnetic labeling [12, 13]. However, the need for labeling adds additional time, steps and resources needed for assay development while also increasing the chances of cell modifications due to external stimuli (label). In contrast, optically active methods such as optical tweezers rely on single-beam gradient force traps for dielectric particles. This method has shown high selectively for particles with very distinctive refractive indices [2] . However, many researchers have noted that the optical force exerted on the particles tends to be smaller in magnitude than other active methods, limiting its resolution for particles with similar refractive indices. Furthermore, the majorities of these optical separation techniques require complicated imaging equipment and experimental setup.

A label-free alternative that has demonstrated high separation capabilities is dielectrophoresis (DEP) [1, 14-16]. When particles are exposed to a non-uniform electric field, they are subjected to a translational DEP force. The force either pushes them toward electric field gradient maxima (positive DEP or pDEP) or toward electric field gradient minima (negative DEP or nDEP) based on the frequency. This phenomenon is dependent on the complex permittivities of the particle and suspending medium [17, 18]. Complex

permittivities of particles are dependent on the biophysical attributes of each cells type. Thus, modulation in electric field parameters can be used to induce different particle trajectories for specific cell types, thereby separating or sorting target cells. One commonly cited method of DEP is field flow fractionation (FFF) DEP, which uses differences in the retention time of particles and DEP forces for the separation of mixtures. Although this technique has shown great promise for the identification of differently sized particles [16, 19], the majority of these devices fall to the limitations of traditional electrode-based DEP (eDEP) and insulator-based DEP (iDEP) such as electrode fouling, electrolysis, and sample contamination) [14, 20]. Moreover, FFF DEP assay do not isolate cell populations in the microfluidic channels but rather create bands of cell populations to classify different groups.

Our approach incorporates passivated-electrode insulator-based dielectrophoresis (πDEP) to create a separation channel exposing cells to DEP forces as they traverse through the chip. In πDEP, a passivation layer is used to prevent disadvantages associated with traditional eDEP and iDEP as outlined previously [15, 21]. In the separation channel, both localized electric fields and highly flexible designs will enable the separation of micro/nano particles. The chips have been tested for two different applications. One is to separate rare circulating tumor cells (CTCs) from blood and the other is to separate neurons from satellite glial cells (SGCs). Both of these applications of our paramount importance in biological and biomedical fields.

CTCs are cancer cells which have been shed from primary tumor sites into the vasculature and have the potential to disseminate throughout the body [22]. Numerous studies have indicated that CTCs may be used as predicative markers for the metastatic level and overall

disease progression of cancers [22, 23]. The presence of high levels of CTCs can be correlated with cancer aggressiveness and increased metastasis, which is the source for 90% of cancer related deaths [24]. Although the isolation and characterization of CTCs can provide a great deal of valuable information regarding cancers, they are generally in low abundances in blood samples. With only 1 to 100 in a single mL of whole blood, there is a clinical need for the rapid separation and analysis of CTCs from red and white blood cells [22].

Glial cells are cells which surround neurons in the central and peripheral nervous system but do not fire action potentials [12, 25]. Although these two unique cell populations can be analyzed based on their cell-to-cell interactions, the individual investigation of these cell types can be imperative. For example, diseases such as sensory neuronopathy or sensory neuron diseases (SND) are characterized by the degeneration of sensory neurons. Similarly, SGC degeneration is linked to chronic pain, which affects nearly 20% of the adult population [26].

The following sections describe the development of our microfluidic chip along with the characterization of its separation efficiency using micro and nano beads. As mentioned, the performance of the chips was further validated through CTC and neuron isolations.

## 5.2 Methodology

### 5.2.1 Device Fabrication

Figure 5.1 depicts the microfluidic device and electrodes with close ups of the separation region (SR). Conventional photolithography techniques were employed to fabricate a negative silicon master [27]. Polydimethylsiloxane (PDMS) microfluidic channels were fabricated using soft lithography, and plasma bonded to a 100μm glass slide.

Cr/Au electrodes were deposited onto a separate Pyrex wafer through physical vapor deposition followed by metal lift-off. An overview of the fabrication process is displayed in Figure 5.2. The SR incorporates eight parallel rows, each of which have nine 100 µm diameter semi-circles on the top and bottom sidewalls, spaced 50 µm apart. Overall size of the chip is 3 cm × 2.5 cm, with a channel depth of 40 µm. The SR utilizes tunable electric fields to induce DEP forces to separate the mixtures through the use of an AC function generator.

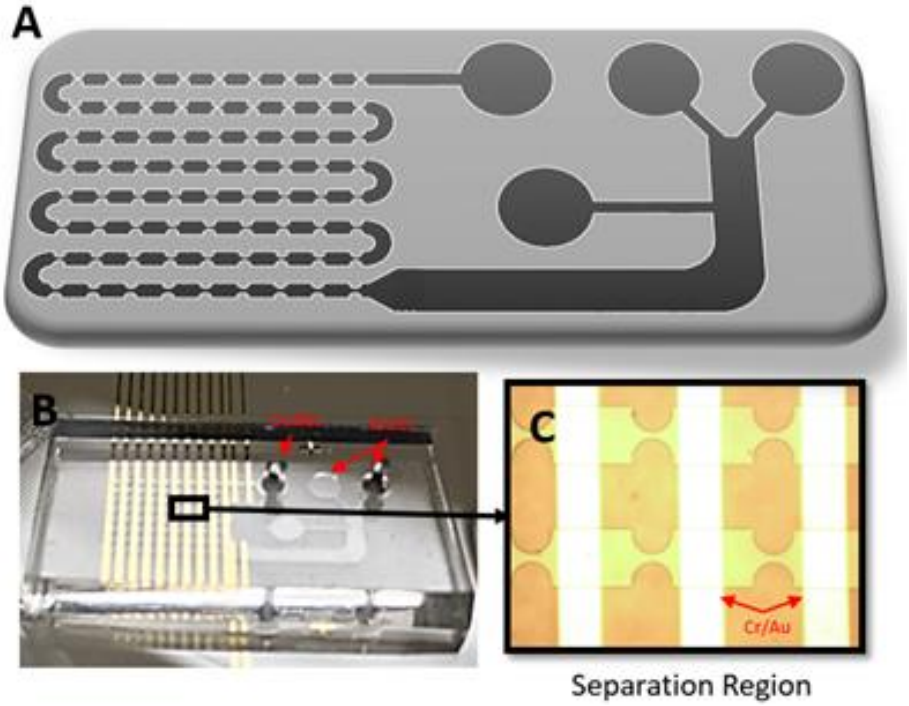


**Figure 5.1:** (A) Top view of microfluidic channel which shows the multiple rows for DEP separation. (B) Optical image of microfluidic chip and Cr/Au electrodes. (C) Close up of SR.

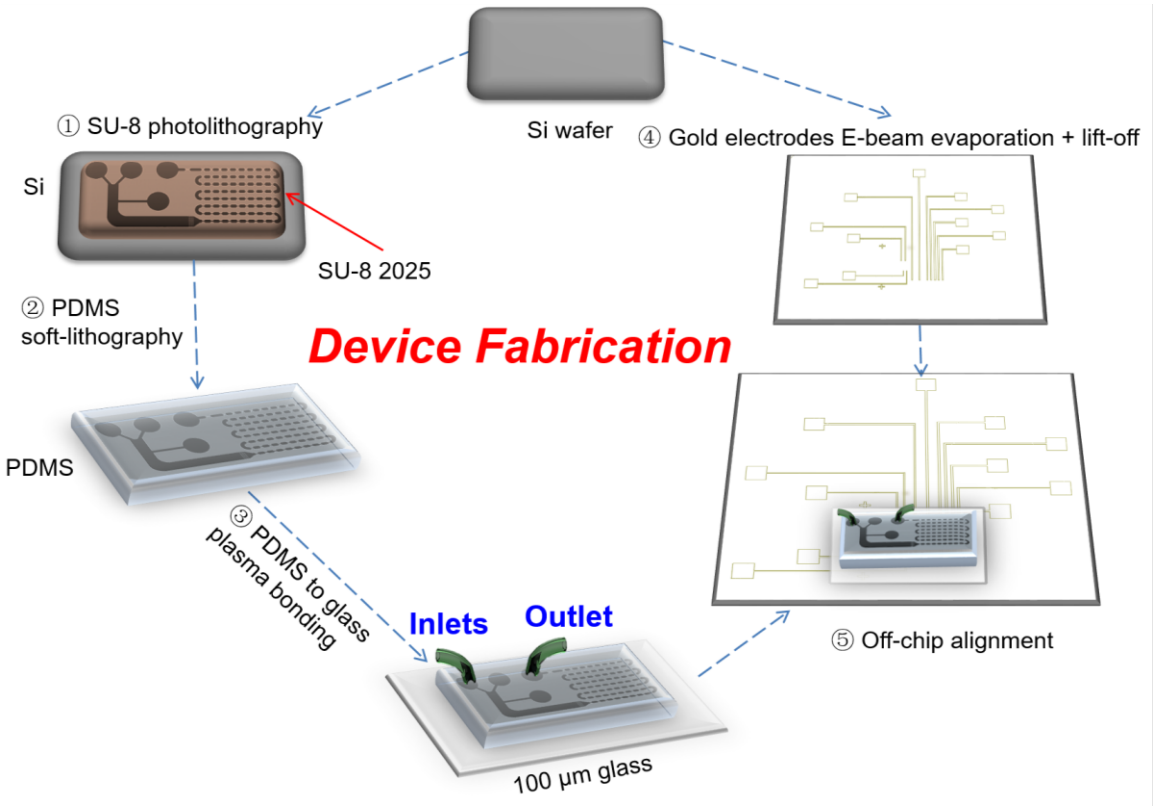


**Figure 5.2:** Overview of device fabrication.

### 5.2.2 Circulating Tumor Cell Sample Preparation

The triple negative MDA-MB-231 breast cancer cells were obtained from the Tissue Culture Shared Resources at Georgetown University Medical Center, Washington, DC. MDA-MB-231 cells were grown in T-25 flasks with culture media. Ingredients for the media include Minimum Essential Medium (MEM Richter's modification) (Life Technologies, NY, USA), 5% charcoal-stripped Calf Serum Charcoal Stripped (Valley Biomedicals, VA, USA) and antibiotics, 100 U/mL penicillin and 100µg/mL streptomycin (Mediatech, VA, USA). The cells were housed in an incubator at 37°C and 5% $CO_2$.

Prior to experimentation, cells were harvested with trypsin and re-suspended in a 113 ± 0.54 µS/cm DEP buffer. Ingredients for the DEP buffer are 8.5 g sucrose (Sigma Aldrich, MO, USA), 0.725 mL MEM (Life Technologies, NY, USA), and

100 mL of deionized water [20]. Cells were washed twice by centrifuge (1500 rpm for 7 minutes) and then re-suspended in the DEP buffer to avoid alterations in the solution conductivity. A Conductivity Meter SG7 (Mettler Toledo, Scherzenbach, Switzerland) was used to verify the final conductivity. The final cell concentration in the samples were adjusted using a hemocytometer. Cell viability in these suspensions was greater than 90% as determined by Trypan blue dye exclusion for each sample.

To simulate CTCs, MDA-MB-231 solutions were mixed with unfiltered whole blood obtained from Wake Forest University Comprehensive Cancer Center. The whole blood was stored at -80°C and thawed prior to mixing. Solutions of whole blood and CTCs were diluted to a 1:10 final concentration of whole blood to DEP buffer. CTC abundances were calculated with a hemocytometer and three petri dish samples for low counts.

### 5.2.3 Neuron and Satellite Glial Sample Preparation

Sensory neurons and satellite glial cells (SGCs) were obtained from the Public Health Center at the Virginia-Maryland College of Veterinary Medicine on the same day as extraction. Primary adult sensory trigeminal ganglia were extracted from 6 week old Swiss Webster mice (Hilltop Lab Animals, Scottsdale, PA) and dissociated using our previously established methods (reference Bertke 2011 PMID 21507969). Following extraction, ganglia were dissociated enzymatically in pre-warmed papain (20 U/ml, Worthington Biochemical Corporation, Lakewood NJ), collagenase II (4 mg/ml, Worthington Biochemical Corporation), and neutral protease (4.6 mg/ml, Worthington Biochemical Corporation), followed by mechanically trituration by pipette to obtain a single cell suspension. Cell suspension was layered on top of a four-layer OptiPrep (Sigma-

Aldrich) gradient and centrifuged at 8000 rcf for 20 min to remove excess axonal debris. Neurons and satellite glial cells were collected from layers two and three of the Optiprep gradient, washed twice in Neurobasal A medium supplemented with B27 Supplement and 1% penicillin-streptomycin (Thermo Fisher Scientific), and resuspended in Neurobasal A medium supplemented with B27 Supplement, 1% penicillin-streptomycin, Glutamax (2 mM), nerve growth factor (NGF, 10 ng/ml), glial cell derived neurotrophic factor (GDNF, 10 ng/ml), and neurturin (NTN, 10 ng/ml). Neurotrophic factors were sourced from PeproTech, Rocky Hill, NJ. Cell viability was determined by phase contrast visual inspection and trypan blue exclusion. Cell suspension was maintained at 37°C until separated. Cell mixtures were then washed twice by centrifuge (1500 rpm for 7 minutes) and then re-suspended in the DEP buffer to avoid alterations in the solution conductivity. A Conductivity Meter SG7 (Mettler Toledo, Scherzenbach, Switzerland) was again used to verify the final conductivity.

### 5.2.4 Experimental Setup

The PDMS microfluidic compartments were placed under vacuum for 30 minutes prior to experimentation to diminish issues associated with priming. Figure 5.3 displays an overview of chip operation. Operation of the biochip was performed by injecting a 1 mL analyte solution using a Pump11 Elite syringe pump (Harvard Apparatus, MA, USA) at a constant rate of 50 µL/hr. The SR electrodes were connected to a 50 MHz function generator (4079 50 MHz Dual-Channel Arbitrary Waveform/Function Generator, B&K Precision, CA, USA) and a voltage amplifier (A800DI Voltage Amplifier, FLC Electronics AB, Sweden). In the SR, the solution was manipulated through tunable electric fields. For high concentration samples, the separation occurs over the entire length of the SR.

A Zeiss Axio Observer epifluorescence microscope was used to monitor the trapping/separation efficiency of particles and cells. Trapping/separation efficiencies were calculated based on the number of particles that were either pushed towards the minima (nDEP) or maxima (pDEP) of the electric field gradients. For polystyrene beads, MDA-MB-231 cells and red blood cells, DEP profiles were initially analyzed separately. A frequency sweep was performed to determine optimal separation ranges for each mixture.

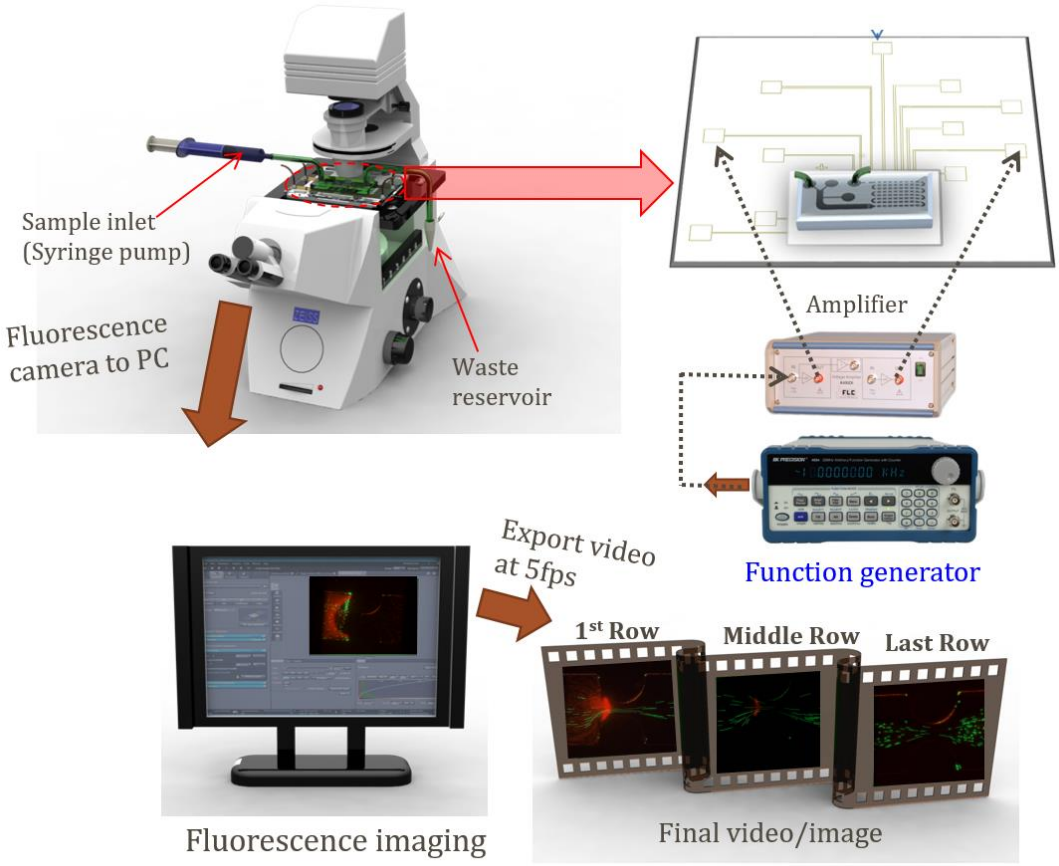


**Figure 5.3:** Overview of device operation.

Although the πDEP device is a label-free, all-electronic assay, initial experimentation was validated of chip performance was done through cross examination with a Zeiss Axio Observer epifluorescence microscope. Trapping efficiencies were calculated based on the

number of particles which were either pushed towards the minima (nDEP) or maxima (pDEP) of the electric field gradients. For polystyrene beads, MDA-MB-231 cells and red blood cells, DEP profiles were initially analyzed separately. A frequency sweep was performed to determine optimal separation ranges for each mixture.

## 5.3 Results and Discussion

### 5.3.1 Polystyrene Bead Characterization and Separation

The 2 μm and 500 nm beads were characterized separately to determine their DEP profiles (Figure 5.4). Each type of bead was suspended in deionized water. Results showed that the 500 nm beads had a crossover frequency of approximately 450 kHz. In contrast, the 2 μm beads had a crossover frequency of approximately 1 kHz. The distinction in the crossover frequency is due to variation in the Clausius-Mossotti (CM) factor based on their relative sizes. Using this variation, the mixtures of the 2 μm and 500 nm beads were theorized to be most effectively separated between 5-400 kHz and 80Vpp. At these frequencies, the 500 nm beads experienced a dominating nDEP force and were pushed toward the electric field gradient minima. On the other hand, the 2 μm beads experienced a dominating fluid force that caused them to travel with the fluid through the SR channel.

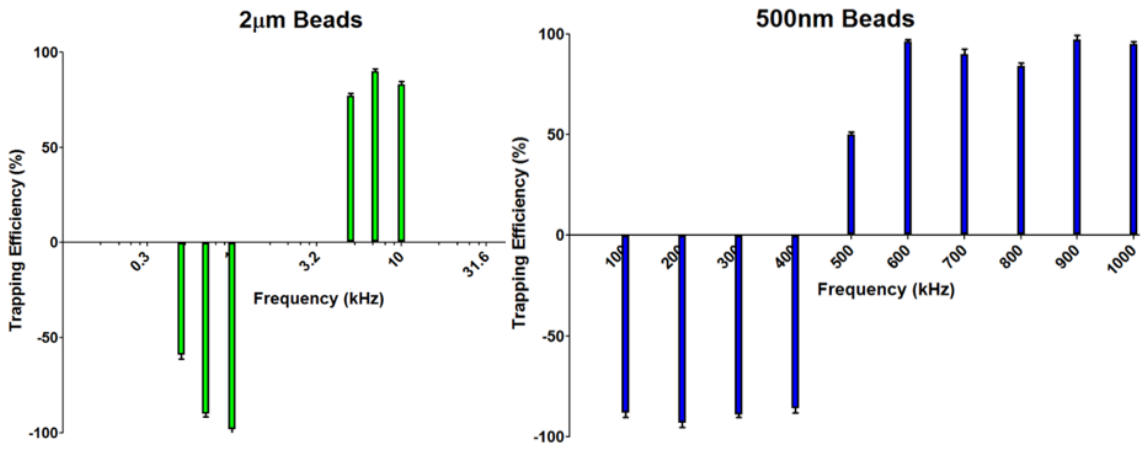


**Figure 5.4:** Estimated trapping efficiencies plotted for selected frequencies, where the negative values indicate nDEP and positive are pDEP. Efficiencies were calculated as number of beads fixed to electric field gradient maxima/minima divided by total beads in the channel. 2 μm beads x-axis is logarithmic.

Separation capabilities of the device was determined by injecting a 1:1 mixture of 2 μm to 500 nm fluorescent polystyrene beads suspended in deionized water at a constant rate of 50 μL/hr. The most effective separation was determined to be at 10kHz and 80Vpp. At this frequency and voltage, the 500 nm beads moved towards the minima of the electric field gradient (nDEP), while the 2 μm beads flowed through the SR channel as shown in Figure 5. Figure 6 indicates the electric field gradient maxima. It should be noted that some of these 500 nm beads flowed through the channel based on their streamlined path. As the sample mixture traversed the SR, the nanoparticles were gradually trapped and hence the outlet contained only the homogenous solution of micron-sized beads as seen in Figure 5. Magnitude and frequency of the electric field in this powerful analytical instrument can be programmed to create different separation profiles. Variation of the device geometry and

electric field parameters resulted in the creation of distinctive bands.

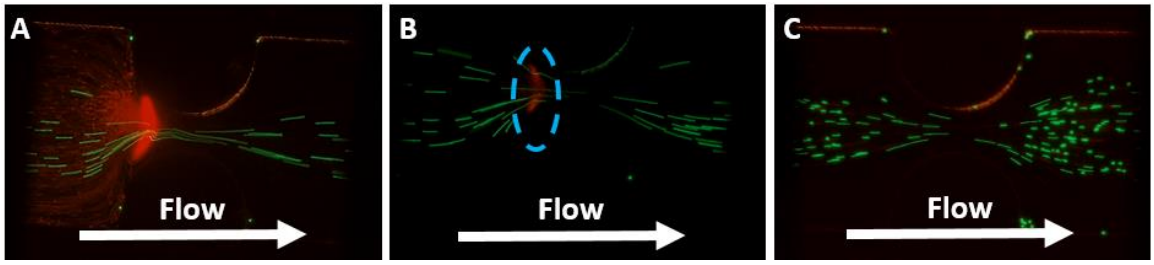


**Figure 5.5:** 2 μm (green) and 500 nm (red) bead separation at 10 kHz. (A) first row of SR where 500 nm beads are forced to electric field minima (nDEP), while the 2 μm flow through as stokes' drag dominates. Note that some 500 nm beads flow through. (B) middle row, where residual 500 nm beads are filtered. (C) 2 μm beads are completely separated from 500 nm beads at final row.

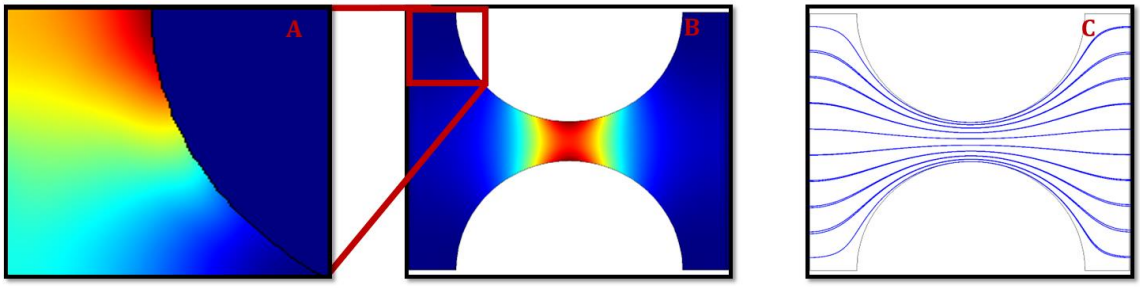


**Figure 5.6:** Channel electric field simulation: (A) is a close up and scaled electric field gradient. (B) is the channel electric field gradients. (C) is the electric field lines.

### 5.3.2 Circulating Tumor Cells Characterization and Separation

Initially, individual solutions of triple negative (highly aggressive) breast cancer MDA-MD-231 and diluted mouse blood were investigated separately. Experiments were

then conducted using MDA-MD-231 cells and mouse blood mixtures to simulate CTCs at varying concentrations in 1 mL of blood. The electric field magnitude and frequency was modulated over the range of 50-100 Vpp, and 1 kHz -1 MHz. Figure 5.7 show representative images of MDA-MB-231 cells, blood cells, and CTCs and blood mixtures under different frequency conditions. The unique behaviors of each sample displays both the frequency dependence of these cells and variations which occur due to the interaction of mixtures. As seen for 100 kHz and above, homogenous solutions of MDA-MB-231 cells experienced pDEP forces which caused them to trap around the semi-circles. However, when mixed with blood cells, no CTCs were observed to be trapped around the semi-circles. This is likely due to changes in the surrounding medium permittivities due to the addition of blood sample to the DEP buffer. However, selective capturing of CTCs from the sample was achieved at voltages above 80 Vpp for frequencies above 200 kHz as shown in Figure 5.8. Operation of the device at these frequencies caused the CTCs to trap around the insulating structure through pDEP. Some CTCs that were trapped at 700 kHz rotated due to the influence of the bulk fluid flow. Whole blood cells under these conditions were observed to pass through the SR and reach the outlet. As they traversed the SR, the red blood cells began to pearl chain and align themselves to the electric field lines as shown by Figure 5.6C. Imaging near the outlet showed that only blood cells passed through the SR to the end of the microchannel. When the DEP force was removed, CTCs then traveled to the outlet. This indicated a high separation yield of the CTCs from blood cells.

Figure 5.9 indicates the frequencies which yielded over 90% separation efficiencies for each concentration of CTCs in blood. Over 90% separation was achieved for all mixtures over the range of 300 kHz-700 kHz although the absolute efficiency for each CTC

concentration varies over the frequency range. Differences in their trajectories under the same electric field conditions can be analyzed as a function of variations in their morphologies (cell size).

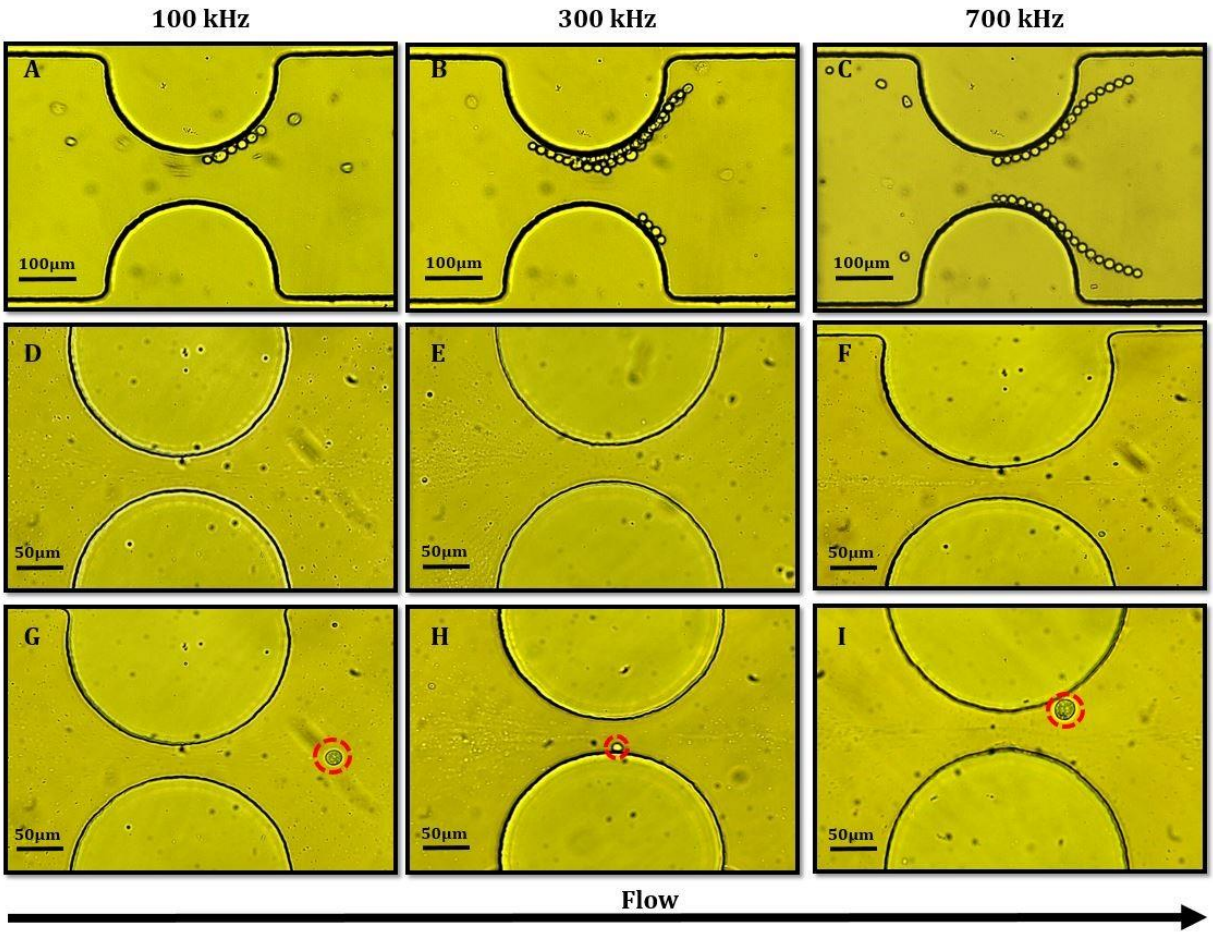


**Figure 5.7:** Representative images of different solutions on similar DEP conditions. (A-C) are MDA-MB-231 cells, (D-F) are whole blood cells diluted in DEP buffer (1:10), and (G-I) are mixtures of MDA-MB-231 cells and diluted whole blood (CTCs). The applied electric field for all trials was 80 Vpp, while the frequency was modulated as indicated by the labels.

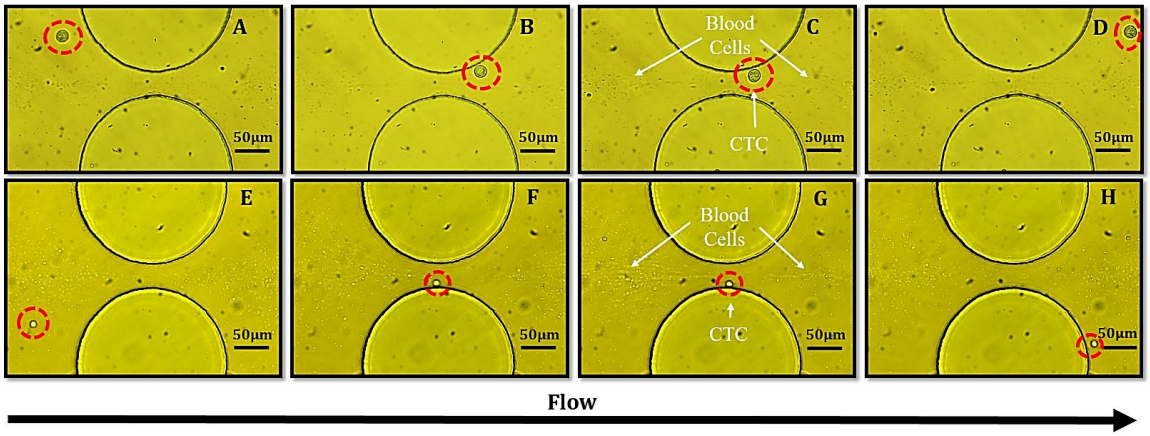


**Figure 5.8:** CTC separation from whole blood. (A)-(C) and (E)-(G) are during DEP excitation at 300kHz, 80Vpp and 700kHz, 80Vpp respectively, while (D) and (H) when the DEP excitation is removed which was used to release CTC.

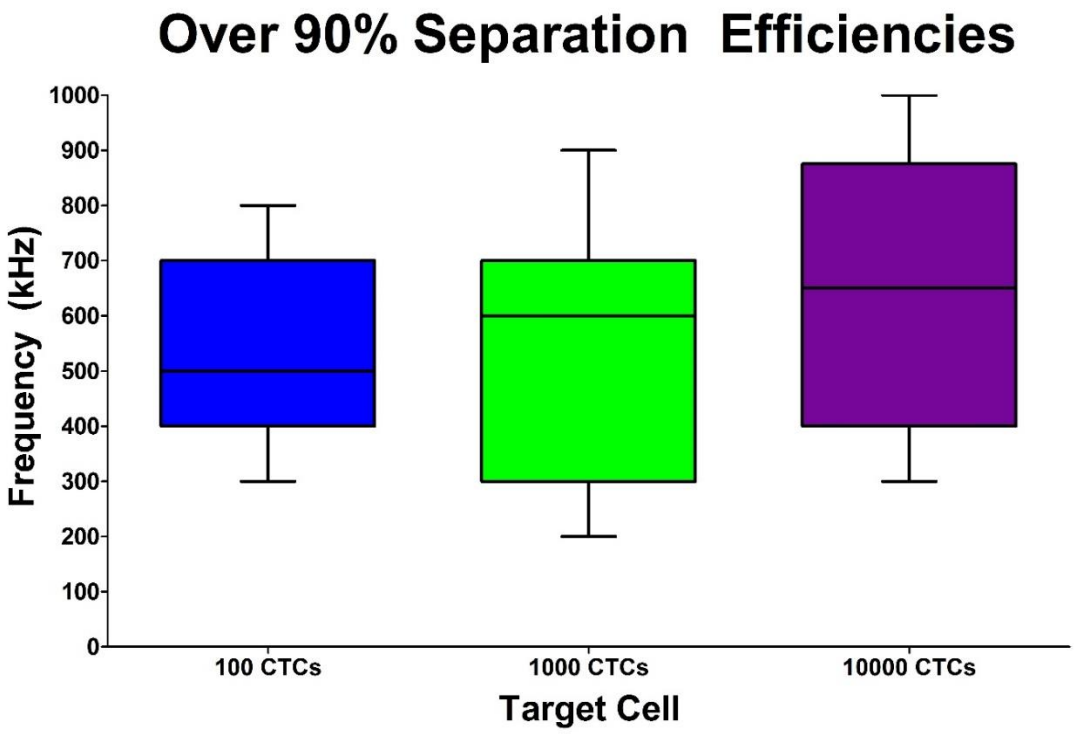


**Figure 5.9:** Frequencies which yielded in over 90% separation efficiencies for 100, 1000, and 10000 CTCs in 1 mL of blood.

### 5.3.3 Neuron and Satellite Glial Cells Separation

To further demonstrate the separation capabilities of the device, heterogeneous mixtures of neuron cells and SGCs were also analyzed. Electric field parameters were optimized through a magnitude and frequency sweep over the range of 50-100 Vpp and 1 kHz-1 MHz. The clearest separation occurred at 300kHz and 80 Vpp. As shown in Figure 5.10, when an electric field with these parameters was applied, the sensory neurons were attracted to the corners of the semi-circle as a result of pDEP. Although some neuron cells collected around the semi-circles, the majority flowed to the top and bottom corners. Figure 5.6 displays the electric field gradient maxima. In contrast, the SGCs were pushed away from the electric field maxima by nDEP forces. As indicated by Figure 5.10C, the SGCs began to pearl chain due to their dipole-dipole interactions and aligned themselves in similar geometries to the electric field lines (seen in Figure 5.6C). Although the SGCs were observed to have some effect caused by the nDEP forces, the flow rate was sufficiently large to ensure they passed through the SR to the outlet. It is important to note that the neuron cells were trapped in the SR even with the large range in size. This further indicates that the selection process in this device is not size exclusive and the electrical properties of the objects have a role too.

Additional experiments at increased flow rates were conducted to further analyze the separation capabilities of the device. As demonstrated by Figure 5.11, when the flow rate was increased, the trajectories of the neurons and SGCs were modulated. Figure 5.12 indicates the frequencies which yielded over 90% separation of the target neurons from the SGCs. As the flow rate increased, the frequency ranges with high separation efficiencies decreased suggesting that the flow has a great influence over the particle trajectories. At 100 μL/hr, no separation efficiencies over 90% were observed. As shown in Figure 5.11,

following electric field excitation, some neuron cells again were pushed toward the corners of the semi-circles. However, the majority of neuron cells began to pearl-chain and flow through the middle of the SR. The SGCs once again flowed through the SR and were pushed away from the electric field gradient maxima although there was less evidence of the SGCs aligning themselves with the electric field lines. Similar phenomena were seen for all cases; separation of the neuron cells and SGCs were observed at other frequencies beyond the ranges shown in Figure 5.12, but at lower efficiencies.

When the velocities of the particles were analyzed, it was found that the two cell populations had differential velocities. The SGCs flowed at higher velocities than the neuron cells. It is theorized that the pDEP attraction slowed down the neuron cells, while the SGCs were unaffected by pDEP affects.

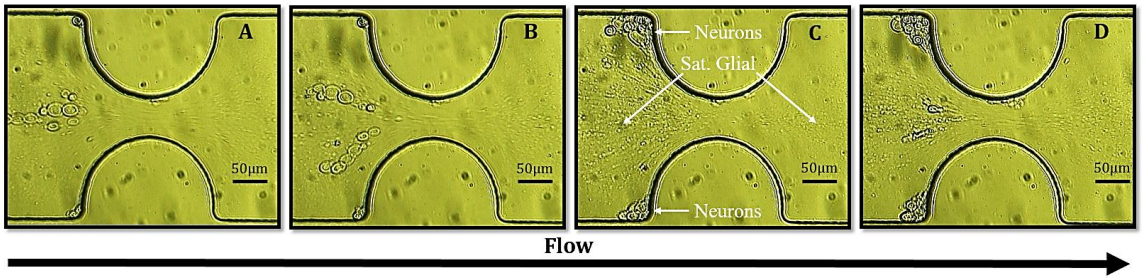


**Figure 5.10:**Neuron cell separation from satellite glial cells at 300 kHz and 80 Vpp.

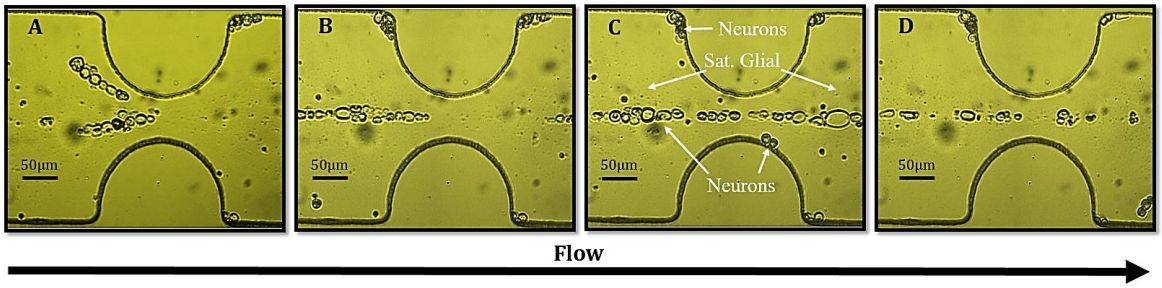


**Figure 5.11: :** Application of 300 kHz and 80 Vpp on neuron and SGC mixtures with a flow rate of 100 µL/hr.

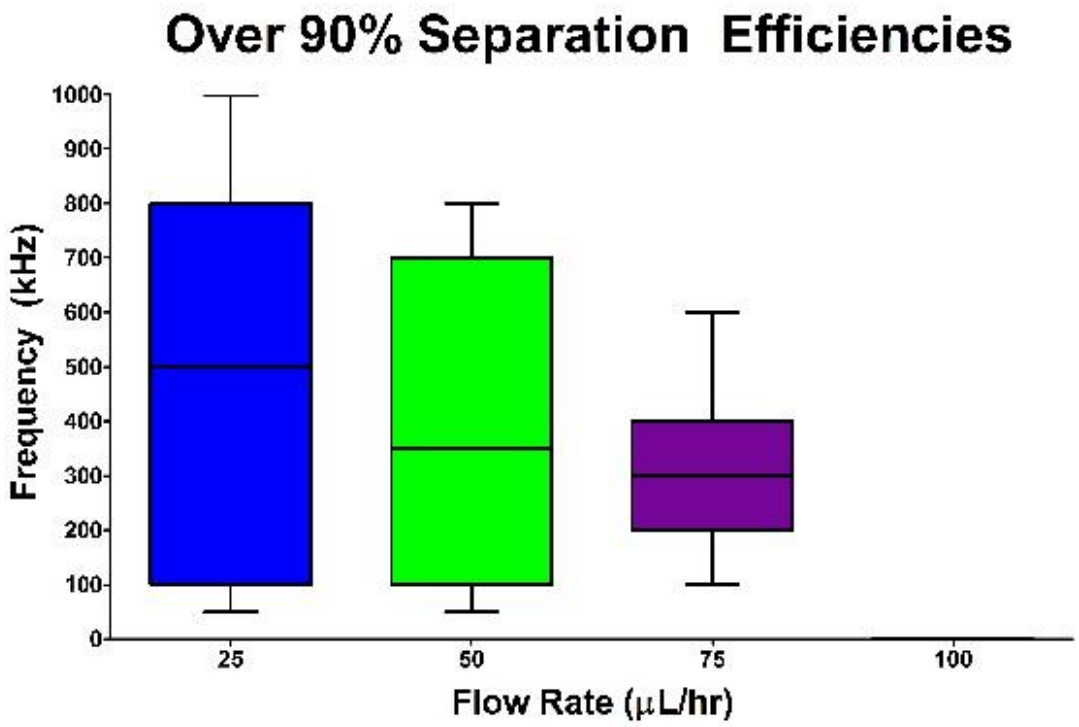


**Figure 5.12:** Frequencies which yielded in over 90% separation efficiencies for 25, 50, 75, and 100 μL/hr.

### 5.3.4 Comparison

Although the use of DEP forces to separate heterogeneous mixtures have been reported by numerous groups, the majority have focused on particles with very distinctive particles sizes or have reported separation efficiencies lower than 90%. Chen et al., recently reported a two stage separation device which combined electro-osmotic and DEP force with efficiencies that exceeded 96% [28]. Similarly, Shafiee et al. reported that prototypes of the cDEP platform achieved 95% or greater removal efficiencies between live and dead cells [29]. Zhang et al. also demonstrated the high separation efficiency of 13 μm and 5 μm with nearly 100% separation [30]. However, all these devices only reported investigations with particles of vastly different sizes/CM factors [1, 10, 28, 30]. In contrast, our results indicate that the πDEP architecture can be incorporated in

innovative microfluidic constructs and high electric field gradients can be locally generated without any contact between electrodes and the fluidic sample. This will allow us to design wide channels for high throughout or long channels to improve separation efficiency or use both attributes in a single platform. The unique design of the SR enabled the formation of local electric fields at each sidewall pair of semi-circles. This allowed for the separation of particles without saturation around the non-uniform structures. This, in turn, suppresses the alteration of the electric field due to dipole-dipole interactions and pearl-chain formation of cells and maintains high separation and trapping efficiency even for highly concentrated samples.

## 5.4 Conclusion

The fabricated microfluidic device has shown great promise for the separation of micro- and nano-scaled particles. The use of DEP forces has allowed for the selective separation of similarly-sized polystyrene beads for initial characterization of the device, highly aggressive breast cancer cells from blood, and neuron cells from satellite glial cells. Furthermore, the flexibility of the device fabrication allows for tunable features which can be customized for various applications. This indicates that the device can be used to separate mixtures on the micron/submicron scale and characterize them, as both heterogeneous and homogenous solutions for a variety of applications.

## 5.5 References

[1] Li, M., Li, W. H., Zhang, J., Alici, G., Wen, W., *Journal of Physics D: Applied Physics* 2014, *47*, 063001.

[2] Sajeesh, P., Sen, A. K., *Microfluidics and Nanofluidics* 2014, *17*, 1-52.

[3] Dittrich, P. S., Manz, A., *Nat Rev Drug Discov* 2006, *5*, 210-218.

[4] Tomlinson, M. J., Tomlinson, S., Yang, X. B., Kirkham, J., *Journal of Tissue Engineering* 2013, *4*, 2041731412472690.

[5] Lopez-Barbosa, N., Campaña, A. L., Noguera, M. J., Florez, S. L., Aroca, M. A., Cruz, J. C., Osma, J. F., *Biosensing Technologies for the Detection of Pathogens-A Prospective Way for Rapid Analysis*, InTech 2018.

[6] Shake, T., Zellner, P., Sahari, A., Breazeal, M. V. R., Behkam, B., Pruden, A., Agah, M., *Analytical and Bioanalytical Chemistry* 2013, *405*, 9825-9833.

[7] Foudeh, A. M., Didar, T. F., Veres, T., Tabrizian, M., *Lab on a Chip* 2012, *12*, 3249-3266.

[8] Lazcka, O., Del Campo, F. J., Munoz, F. X., *Biosensors and bioelectronics* 2007, *22*, 1205-1217.

[9] Pethig, R., *Biomicrofluidics* 2010, *4*, 022811.

[10] Lee, D., Nam, S. M., Kim, J.-a., Di Carlo, D., Lee, W., *Analytical chemistry* 2018, *90*, 2902-2911.

[11] Haddadi, H., Di Carlo, D., *Bulletin of the American Physical Society* 2018.

[12] Tome-Garcia, J., Doetsch, F., Tsankova, N. M., *Bio-protocol* 2017, *7*.

[13] Romany, L., Egea, R. R., Meseguer, M., Aparicio-Ruiz, B., Remohi, J., Garrido, N., *Fertility and Sterility* 2017, *108*, e128-e129.

[14] Pethig, R. R., *Dielectrophoresis: Theory, Methodology and Biological Applications*, John Wiley & Sons 2017.

[15] Nakidde, D., Zellner, P., Alemi, M. M., Shake, T., Hosseini, Y., Riquelme, M. V., Pruden, A., Agah, M., *Biomicrofluidics* 2015, *9*, 014125.

[16] Gascoyne, P. R., Shim, S., *Cancers (Basel)* 2014, *6*, 545-579.

[17] Gascoyne, P. R., Vykoukal, J., *Electrophoresis* 2002, *23*, 1973.

[18] Pohl, H. A., Crane, J. S., *Biophysical journal* 1971, *11*, 711-727.

[19] Gascoyne, P. R. C., Shim, S., Noshari, J., Becker, F. F., Stemke-Hale, K., *ELECTROPHORESIS* 2013, *34*, 1042-1050.

[20] Soltanian-Zadeh, S., Kikkeri, K., Shajahan-Haq, A. N., Strobl, J., Clarke, R., Agah, M., *ELECTROPHORESIS* 2017, *38*, 1988-1995.

[21] Zellner, P., Shake, T., Sahari, A., Behkam, B., Agah, M., *Anal Bioanal Chem* 2013, *405*, 6657-6666.

[22] Plaks, V., Koopman, C. D., Werb, Z., *Science* 2013, *341*, 1186-1188.

[23] Williams, S. C., *Proceedings of the National Academy of Sciences* 2013, *110*, 4861-4861.

[24] Sollier, E., Go, D. E., Che, J., Gossett, D. R., O'Byrne, S., Weaver, W. M., Kummer, N., Rettig, M., Goldman, J., Nickols, N., *Lab on a Chip* 2014, *14*, 63-77.

[25] Sghirlanzoni, A., Pareyson, D., Lauria, G., *The Lancet Neurology* 2005, *4*, 349-361.

[26] Hanani, M., Spray, D. C., in: Parpura, V., Verkhratsky, A. (Eds.), *Pathological Potential of Neuroglia: Possible New Targets for Medical Intervention*, Springer New York, New York, NY 2014, pp. 473-492.

[27] Zellner, P., Shake, T., Hosseini, Y., Nakidde, D., Riquelme, M. V., Sahari, A., Pruden, A., Behkam, B., Agah, M., *ELECTROPHORESIS* 2015, *36*, 277-283.

[28] Chen, X., Ren, Y., Liu, W., Feng, X., Jia, Y., Tao, Y., Jiang, H., *Analytical Chemistry* 2017, *89*, 9583-9592.

[29] Shafiee, H., Sano, M. B., Henslee, E. A., Caldwell, J. L., Davalos, R. V., *Lab on a Chip* 2010, *10*, 438-445.

[30] Zhang, J., Yuan, D., Zhao, Q., Yan, S., Tang, S.-Y., Tan, S. H., Guo, J., Xia, H., Nguyen, N.-T., Li, W., *Sensors and Actuators B: Chemical* 2018, *267*, 14-25.

# 6 Future Outlooks

## 6.1 DEP Chromatography

Separation and identification of particles in environmental, chemical, and biological samples is imperative for a wide range of applications With the growing need for targeted therapies for cancer patients, tools to sort cell for the analysis of disease progression, drug sensitivity, and metastatic level are urgently needed [1-3]. Other research areas such as pathogen detection in drinking water, isolation of immune cells from peripheral blood, neural separations and various other biological samples also can benefit from effective cell separation and identification methods. This section reports a novel isolation technique which integrates two unique separation methods: chromatography and DEP. The combination of preconcentrating and separation regions governed by DEP forces and an impedance detection region, can enable the characterization and separation of micron and submicron particles as shown in Figure 6.1.

Operation of the device occurs by injecting an analyte sample into the chip. The sample is then enrichened or preconcentrated to ensure programmable injection times for resolution enhancement and saturation prevention in the separation area. The innovative geometry of the SR, enabled by the design in Chapter 5, allows for both localized electric fields and a highly flexible designs to separate particles over the length of the SR. Bands of cell populations can then be electrically detected at the end of the microfluidic channel through impedance measurements similar to Chapter 4.

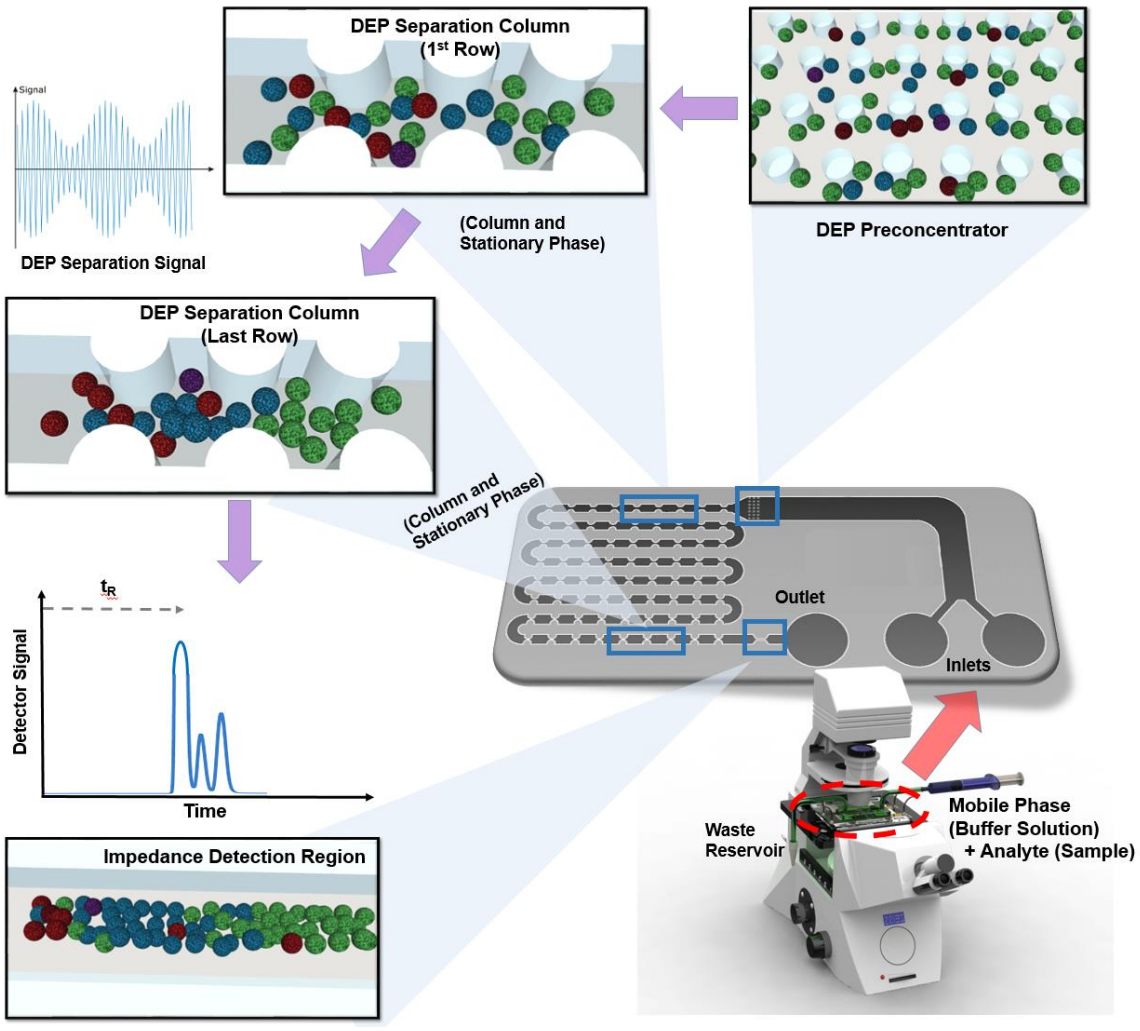


**Figure 6.1: :** Conceptual image of a DEP chromatography platform for particle separation, where spheres in each region represent a particle in a sample. Each color denotes a unique particle type.

Furthermore, the device incorporates features comparable to chromatography, where the DEP force acts as the stationary phase and a suspending medium is the mobile phase. Initial characterization of 2 µm and 500 nm polystyrene beads mixtures indicated high separation yields when operated at 10 kHz and 80 Vpp. When the magnitude and frequency of the electric field, and electrode geometries were varied, distinct bands were observed as shown in Figure 6.2.

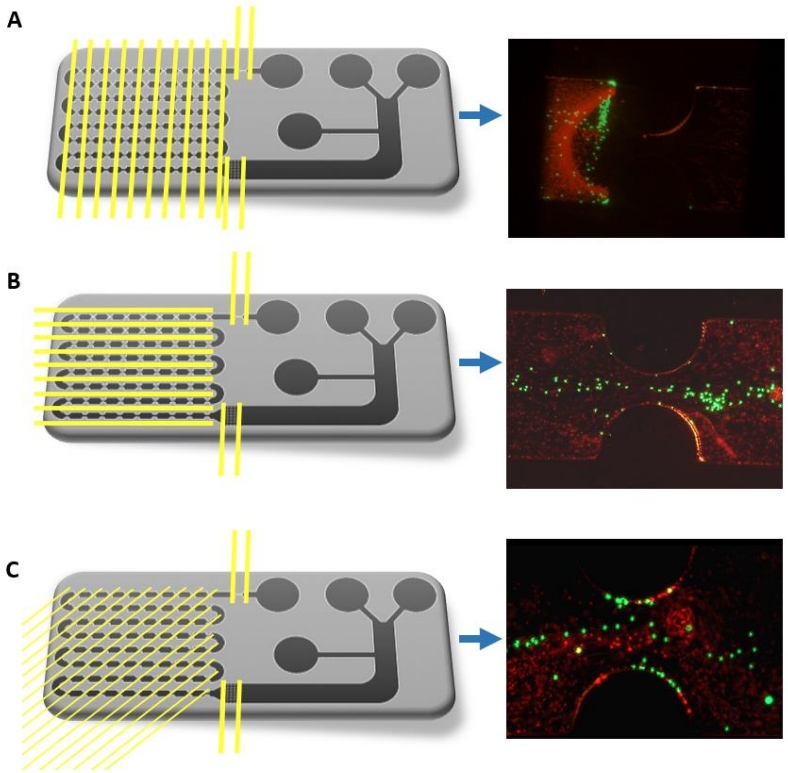


**Figure 6.2:** Different electrode orientations.

As the DEP chromatography device is a proof-of-concept chip, further experiments will be required to optimize the novel separation technique. Standard chromatography parameters, such as retention time, plug width, plate number and Height Equivalent to a Theoretical Plate (HETP) will be identified based on the impedance measurements. Additionally, the flexibility of the πDEP fabrication process will be utilized to create additional unique geometries for the SR. These geometries will be optimized to achieve the highest resolution for the separation of particles. However, the current design is still highly promising due to the high level of separation based on preliminary samples. From this, we conclude that the concept of DEP chromatography has the potential to be used for the separation of a variety of particles.

## 6.2 DEP Fiber

The primary mode of DEP investigations for this thesis has been driven by MEMS-based microfabrication techniques and devices. Although they have shown great versatility in their applications and flexibility in their designs, alternative methods can also provide significant benefits over traditional MEMS devices. This section presents a novel method of microfluidic particle manipulation through the use of thermally drawn fibers. Fibers have a variety of applications, and naturally incorporate 3D structure which are more difficult to fabricate with cleanroom based methods. Fabrication of a fiber with a circular cross section (Figure 6.3A) is done by initially forming a rod structure. With a Teflon rod as the base material, a layer of Polycarbonate(PC) film was rolled onto the rod. It was then consolidated in a vacuum oven. Following consolidation, two slots were machined into the rod, such that they were one the same horizontal plane as seen in Figure 6.3A. Another layer of PC film was added to the machine rod until the overall size reached a desired diameter. This structure was then consolidated to enable fiber stability during the drawing process. After the second consolidation, the Teflon rod was removed from the pre-form and one single copper wire (125μm diameter) were inserted into each of the two machined slots. The fiber was then thermally drawn using a drawing furnace. The final structure had a hollow channel surrounded by PC and two copper wires.

For initial characterization and DEP experimentation, the copper wires were stripped and connected to a function generator and amplifier. 2 μm and 500 nm polystyrene beads were characterized individually to demonstrate the presence of DEP forces. Figures 6.3B (2 μm) and 6.3D (500 nm) show the lateral cross section of the fiber when the bead samples were pushed through the microchannel. Figures 6.3C (2 μm) and 6.3E (500 nm) display the movement of the particles following the DEP excitation at 80 Vpp and 100 kHz. The 2

μm beads traveled the sidewalls of the fiber, while the 500 nm beads seemed to form a cylinder in the center of the channel. This suggests that the fibers may be used for DEP experimentation.

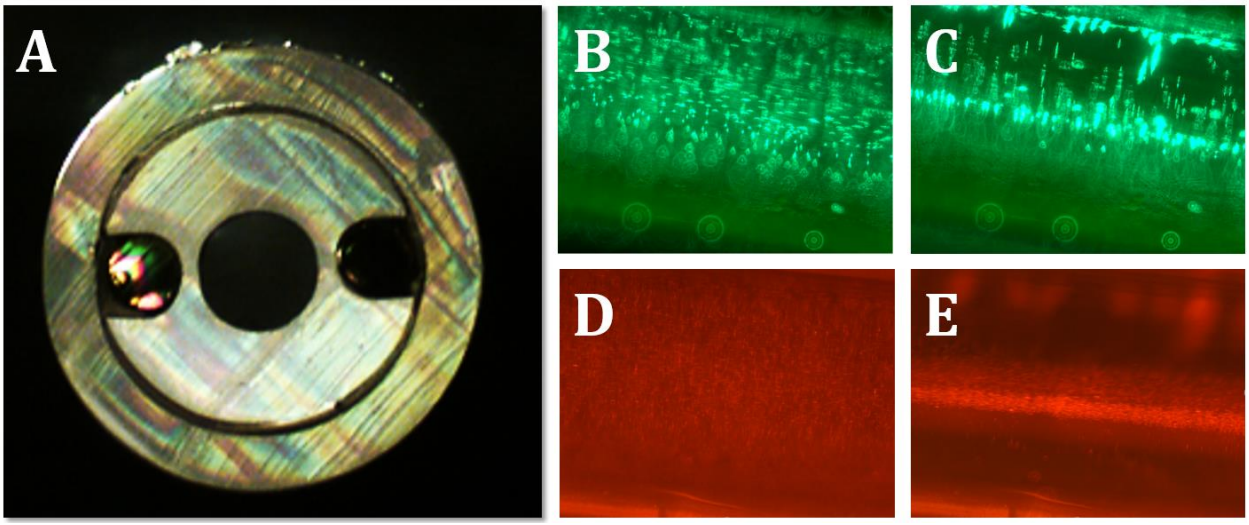


**Figure 6.3:** DEP Fiber with DEP excitation for (C) and (E). Copper electrodes shown in (A) are 125 μm.

## 6.3 References

[1] Li, M., Li, W. H., Zhang, J., Alici, G., Wen, W., *Journal of Physics D: Applied Physics* 2014, *47*, 063001.

[2] Sajeesh, P., Sen, A. K., *Microfluidics and Nanofluidics* 2014, *17*, 1-52.

[3] Dittrich, P. S., Manz, A., *Nat Rev Drug Discov* 2006, *5*, 210-218.

# 7 Conclusion

Throughout this thesis a microfluidic-based DEP devices were presented for the use in a variety of unique biomedical applications. Chapters 2 and 3 focused on the drug response of cancer cells with different sensitivities. DEP profile were assessed over a range of different chemical stimuli, dosages, and exposure lengths. Results demonstrated that each cell had distinctive shifts to their DEP profiles when exposed to each chemical stimulus. This suggested that DEP phenomena could be used to analyze the drug response of cells. Further investigations with cell proliferation assays, cell morphology imaging, and gene expression analysis provided additional information regarding the cell physiology which was correlated to DEP profile shifts. In chapter 4, DEP forces were employed to selectively enrich pathogens. Following specific enrichment periods, the pathogens were selectively released to allow for downstream impedance detection. Enrichment and electrical sensing of live/dead bacteria samples showed that the πDEP platform could be utilized for rapid pathogen detection. The development of a high throughput design was also reported. Chapter 5 presented a low cost microfluidic chip for the separation of heterogeneous biological mixtures. DEP forces were induced in a SR to allows for isolation of different cell populations. Initial testing of the device displayed high separation yields of micron and submicron, CTC and whole blood, and sensory neuron and SGC mixtures.

In order to attain these results, I had to develop a wide variety of skills. Some of these skills include device design, cleanroom-based microfabrication, soft lithography, cell culturing, fluorescence staining and microscopy, drug treatment techniques, DEP experimentation, and impedance spectroscopy. Beyond laboratory techniques, I also

developed several skills in technical communication through an oral presentation at a conference, drafting and revising numerous journal papers, and aiding in the writing of grant proposals.